Experiments on the Interaction of a Coflowing Light Gas Jet with a Weak Oblique Shock Wave

Thesis by
Kevin C. Moore

In Partial Fulfillment of the Requirements
for the Degree of
Doctor of Philosophy

California Institute of Technology
Pasadena, California

1996

(Defended May 29, 1996)

Acknowledgements

I wish first to express my gratitude to Professor Zukoski for the valuable guidance and support he has provided during my years at Caltech. I would also like to thank Professors Kubota and Marble for their valuable advice; they contributed a great deal to my understanding of the project. I am grateful to Professor Shepherd for advice he provided concerning the viewing and interpretation of the experimental data.

Thanks go to Doctor Larry Hill for his many contributions during the initial defining stages of the project; Doctor Donald Kendrick for his assistance in the manufacture of the temperature probes and measurement of their time constants; Doctor Khalid Juhany for conversations concerning the analysis of the temperature data; Doctor John Budzinski for his advice on the care and operation of the dye laser; everybody in the GALCIT Aeronautics shop for their expertise and helpfulness in the construction of the experimental apparatus; and Pavel Svitek of the GALCIT Hydrodynamics lab for his expert help with various parts of the experiments.

I am grateful for the help and friendship that the staff and my fellow students of the Aeronautics and JPC departments have given me. They have made my experience here at Caltech an enjoyable one.

I also wish to express my gratitude and love to my wife Angelyn, whose patience and support through this process has gone above and beyond the call of duty. I would also like to express special thanks to my parents for all of the support and encouragement they have given me over the years.

Sponsorship of this work was provided in part by the URI AFOSR-90-0188 and Dr. Julian Tishkoff. Other sources of support included a National Science Foundation Fellowship, a Daniel and Florence Guggenheim Fellowship, and Graduate Research and Teaching Assistantships from the California Institute of Technology.

Experiments on the Interaction of a Coflowing Light Gas Jet with a Weak Oblique Shock Wave

by

Kevin C. Moore

In Partial Fulfillment of the
Requirements for the Degree of
Doctor of Philosophy

Abstract

Results of experiments performed in the GALCIT Supersonic Wind Tunnel involving a coflowing helium jet in a Mach 2.4 air freestream are presented. Measurements of the undisturbed jet are compared with those made after the jet interacts with different weak oblique shock waves. Data collected using stagnation temperature and pitot pressure probes is used to form time averaged cross sectional views of the flow for different downstream stations. These views show that the baroclinic vorticity generated when the jet passes through the shock wave causes the jet to develop into a pair of counter-rotating vortices whose axes are aligned with the flow. Previously proposed models for the circulation deposited on the jet-freestream interface and characteristic time of an analogous unsteady two-dimensional flow are adapted to this flow. Comparison of the jet cross sections for corresponding characteristic times shows agreement with experiments and analysis previously performed on the unsteady two-dimensional analogy. Shear between the jet and the freestream is not seen to materially affect the development of the flow, but the development of the jet is seen to strongly depend on the strength of the oblique shock. Scattering of a laser light sheet off of ice crystals present in the air but absent from the helium provides time-resolved flow visualization pictures which show large departures from the mean as the flow moves downstream. This demonstrates the need to consider turbulence effects which were not considered in previous two-dimensional studies.

They also show that the presence of the shock wave increases the apparent randomness of the flow as well as the spreading rate of the jet, likely increasing mixing. A jet cross section extracted from the average of several Rayleigh scattered images agrees well with the general size and shape of the jet cross section taken from the corresponding time averaged temperature data. The design and construction of the active feedback control loop in a gas blending system used to independently control the mass flowrate and temperature of the jet is described.

Contents

List of Figures

List of Tables

List of Symbols

Symbol	: **Description and page when applicable**
$()_0$	: pertaining to the initial conditions
$()_1$	: pertaining to conditions just prior to the shock interaction
$()_2$	: pertaining to conditions just after the shock interaction
$()_{cm}$	: pertaining to the center of mass
$()_h$	: pertaining to conditions of the heavy gas
$()_l$	: pertaining to conditions of the light gas
$\widehat{()}$	: pertaining to a characteristic distance
$\overline{()}$	: the mean of a value
$()_{air}$	: pertaining to pure air
$()_{He}$	: pertaining to pure He
a	: speed of sound
$At = \frac{\rho_h - \rho_l}{\rho_h + \rho_l}$	: Atwood number
C_d	: drag coefficient
d	: exit diameter of the jet
δ	: flow deflection angle caused by shock
Γ	: circulation
h	: convective heat transfer coefficient
k	: thermal conductivity
Kn	: Knudsen number
M	: Mach number, mass

μ : viscosity

r : radius of gyration

R : the gas constant for a particular species

r : radius of the jet

Re : the Reynolds Number based on the jet exit diameter

ρ : density

t : time

τ : characteristic time

θ : angle of oblique shock wave with respect to upstream flow

u : velocity

x : streamwise distance from the injector exit

y : vertical distance from tunnel centerline

z : horizontal distance from tunnel centerline

Chapter 1

Introduction

The mixing of two fluids under compressible conditions is a subject of current interest to the aeronautics community. The complexity of this class of problems makes it difficult to study analytically or computationally; thus, experimental investigations are important in advancing the understanding of these flows. Herein are presented the results of experiments on the interaction of a weak oblique shock wave with a coflowing light gas jet and its effect on the mixing of the light gas jet with a denser freestream.

1.1 Motivation

The original motivation for studying this flow comes from the field of high speed aircraft propulsion. Air breathing engines with subsonic combustion cycles are limited to maximum vehicle speeds for which the Mach number is about 6. This is due to the static temperature increase and the stagnation pressure losses associated with decelerating the freestream to subsonic conditions.

For speeds above Mach 6 a supersonic combusting ramjet, or scramjet, engine is generally considered the best choice ([11], page 11). Keeping the flow in the combustion chamber supersonic reduces the temperature increase and stagnation pressure losses. However, the high speed of the flow in the combustion chamber results in a low residence time for the fuel and air in any reasonably sized engine. Typical residence times are in the range of 1 to 2 milliseconds for a Mach 15 vehicle [3]. This

results in a requirement that the fuel mix and burn as quickly as possible. Hydrogen is the fuel of choice for such an engine due to its high reaction rate and its suitability as a regenerative coolant. The problem in this case is then one of mixing the less dense hydrogen fuel with the more dense air quickly enough to achieve complete combustion before the reactants leave the combustion chamber.

The applicability of this study is not strictly limited to scramjet engine research. For example, the operation of high power chemical lasers also depends on the rapid mixing and reaction of two supersonic streams (typically hydrogen or deuterium mixing with fluorine or a fluorine donor) [10].

1.2 Background

Marble, et al. [18] originally proposed the use of a weak oblique shock wave to enhance the mixing between the fuel and air in a scramjet combustor. The technique relies upon the Richtmeyer-Meshkov (or shock induced Rayleigh-Taylor) instability. A shock wave passing across the interface between two gases of different densities distorts the interface due to the vorticity generated on the contact surface at points where the density gradient across the surface is not aligned with the pressure gradient across the shock wave [2].

By processing a hydrogen jet through a weak oblique shock wave, baroclinically generated vorticity on the hydrogen-air interface causes the jet to develop into a pair of counter-rotating longitudinal vortices as it moves downstream in a steady three-dimensional flow. Figure 1.1 shows a side view such a flow. The unshaded region is the denser air freestream, the lightly shaded region is the less dense hydrogen jet, and the darker shaded region is the wall of the combustor. Flow is from left to right, and the turn in the wall generates the shock wave represented by the dashed line.

1.2.1 The Analogous Two-Dimensional Flow

A diagram of a two-dimensional unsteady analogy to the three-dimensional steady flow of Figure 1.1 is shown in Figure 1.2. The lightly shaded region represents the

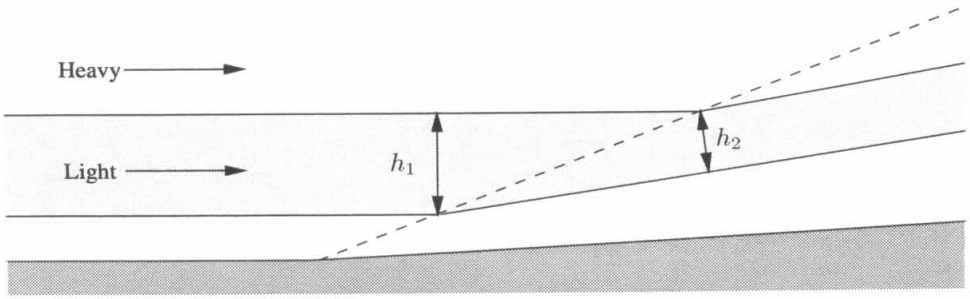

Figure 1.1 Side view of light-gas jet going through weak oblique shock wave

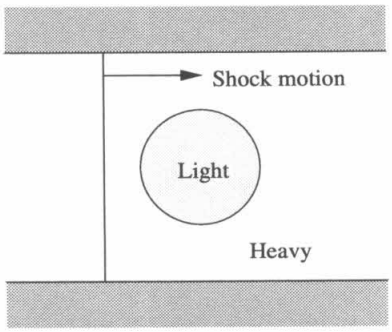

Figure 1.2 View along the axis of cylindrical inhomogeneity in two-dimensional analogy

cross section of a cylinder of light gas, while the unshaded section represents the air in a shock tube. The darker shaded regions represent the shock tube walls, and the shock wave is traveling from left to right in this picture. As the shock moves over the interface between the denser and the lighter gas a series of refractions and reflections take place, and vorticity is deposited on the interface. The portion of the inviscid vorticity equation which describes this is

$$\rho \frac{D}{Dt}\left(\frac{\underline{\omega}}{\rho}\right) = \frac{1}{\rho^2}(\underline{\nabla}\rho \times \underline{\nabla}p) \tag{1.1}$$

Figure 1.3 (from [32], page 121) shows how the gas cylinder evolves over time into a

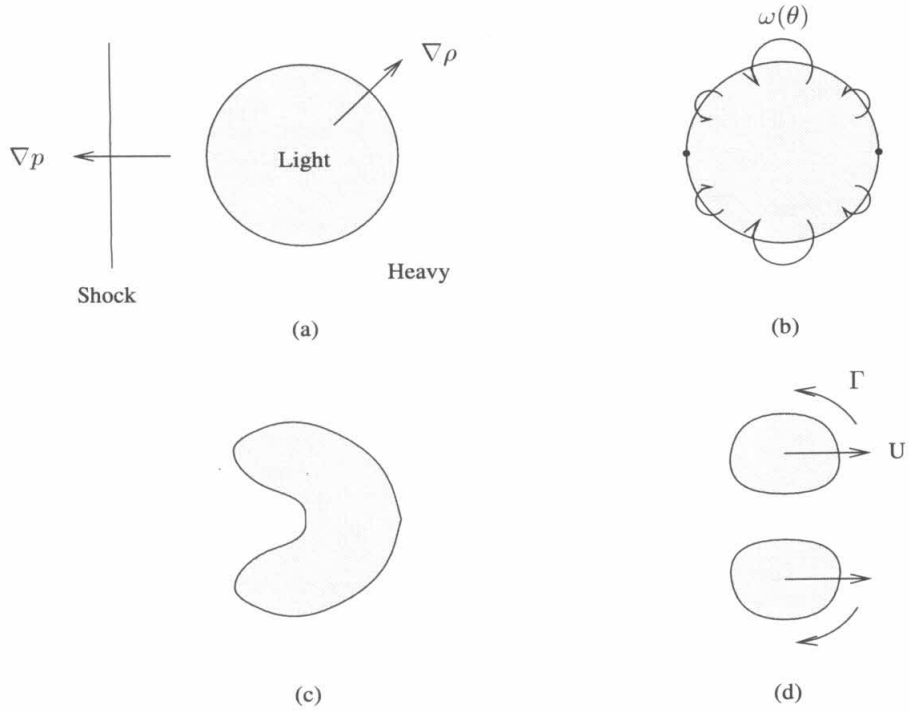

Figure 1.3 Development of flow in two-dimensional analogy

pair of counter-rotating vortices due to the vorticity deposited as the shock passes. Figure 1.3(a) shows the cylinder just before the shock arrives, Figure 1.3(b) shows the distribution of vorticity around the interface just after the shock passes, Figure 1.3(c) shows the initial deformation of the interface, and Figure 1.3(d) shows the pair of counter-rotating vortices after they have fully developed. Figures 1.3(a) through 1.3(d) can also be viewed as cross sections of the flow shown in Figure 1.1. Figures 1.3(a) and 1.3(b) represent cross sections of the light gas jet just upstream and just downstream of the shock, respectively, and Figures 1.3(c) and 1.3(d) represent cross sections taken successively further downstream after the shock interaction.

In the two-dimensional studies the geometry is such that the pressure gradient across the shock is perpendicular to the axis of the jet. The pressure gradient across the oblique shock in the three-dimensional geometry is not perpendicular to the axis

of the jet; it has a component parallel to the jet's axis. This means that the vorticity generated by the shock-jet interaction has a component which is locally tangent to the interface between the jet and the freestream. This locally tangent vorticity component can be equivalently viewed as being due to the different decelerations of the jet and the freestream in the streamwise direction. Thus, the velocity difference between the jet and the freestream has to change across the oblique shock wave in the three-dimensional problem. Shear between the jet and the freestream is not modeled at all in the two-dimensional problem.

Rudinger and Somers [23] performed early experiments on the effect of acceleration on small bubbles of gas whose densities were different than that of the surrounding freestream. They were primarily motivated by a wish to understand the motion of gaseous tracers used in experiments. The experimental configuration was analogous to that shown in Figure 1.2. Their gas bubbles were created by either a spark gap or injection of a gas through a needle tube. Results consisted of measurements of the bubble velocity relative to the surrounding gas, and these were compared to the predictions of a simple model. The scale of the experiments was too small to resolve the details of the development of the flow into a pair of vortices.

Haas [8] and Haas and Sturtevant [9] were interested in the initial development of the flow after passage of the shock and how it related to the general case of turbulence generation and subsequent intensification of mixing by finite amplitude waves in random media. Their experiments were on a larger scale than those of Rudinger and Somers and used microfilm membranes to contain cylinders of gas prior to the shock's arrival. Picone and Boris [22] and Marble, et al. [18] both performed computations modelling these experiments.

Jacobs [13], Budzinski [3], and Yang ([32], [34], and [33]) have studied the two-dimensional problem specifically with an eye toward its applicability to the scramjet fuel mixing problem. Jacobs performed experiments using a biacetyl tracer in the light gas to allow flow visualization using planar laser induced fluorescence. Budzinski's investigations focussed on quantitatively measuring the amount of mixing as well as measuring the circulation deposited on the interface. He utilized the different

Rayleigh scattering cross sections of helium and nitrogen to make direct measurements of the mass fraction of helium. Yang performed extensive computations on a number of variations on the basic problem. He looked at configurations including multiple shocks, arrays of jets, different jet shapes, and variations of the interface thickness.

1.2.2 Other Related Studies

Waitz performed both numerical and experimental investigations using a contoured wall injector ([30] and [31]). The injector consisted of a rearward facing ramp with slot injectors spaced evenly across its width. The expansion at the top of the ramp was followed by a compression at the base. Each slot injector's exit coincided with the origin of the compression, so the jets exiting from the injectors were immediately processed through the shock. In addition to other measurement techniques, he obtained composition measurements of the flow using a gas analyzer specifically constructed for the task, but they were not temporally resolved. Direct comparison with Waitz's results is difficult because his experimental configuration was much more complicated than that used in this study.

The same steady three-dimensional flow geometry as was investigated by this author was studied computationally by Drummond [6]. Drummond used a coflowing hydrogen jet and included chemical reaction and heat release, and looked at conditions similar to those expected in a scramjet combustor. He concluded, "Marble's injector scheme appears to be an excellent candidate for use in actual combustor configurations."

1.2.3 Time Scaling

Yang [32] proposed a time scale for finite strength shocks of $\tau = HW/\Gamma$, where H is a characteristic height of the jet, W a characteristic width, and Γ is the circulation deposited on each half of the interface by the shock interaction. This characteristic time is based upon the amount of time it takes for the jet to be split due to the motion induced by the vorticity on the interface. The characteristic velocity is represented

by Γ/W, and the distance the dividing stream must travel is represented by H.

Due to the finite strength of the shock the values of H and W are not equal after the shock interaction. The circular nature of the jet shown in Figure 1.3(b) is true only for a weak wave; in the case of a stronger shock the interface will be compressed in the horizontal direction and exhibit a more elliptical shape. Yang accounted for this compression by scaling the distance the dividing jet must travel by the density ratio across the shock wave. Using the initial jet radius as the basis for his length scale resulted in a time scale of

$$\tau = \frac{\rho_1}{\rho_2}\frac{r_0^2}{\Gamma} \tag{1.2}$$

For the steady three-dimensional configuration shown in Figure 1.1 a different scaling must be used to account for the compression caused by the finite shock strength. In the two-dimensional case the density ratio across the shock is inversely related to the geometrical compression across the shock; lines parallel to the shock remain the same length after its passage while those perpendicular to it shrink by a factor equal to the inverse of the density increase across the shock. This ignores the complications caused by the shock's passage through the inhomogeneity. Three-dimensional effects complicate the problem for the oblique shock wave in Figure 1.1, and the actual geometrical measurements must be used instead of the density ratio across the shock. This gives a version of Yang's time scale modified for the three-dimensional case:

$$\tau = \frac{h_2}{h_1}\frac{d_1^2}{4\Gamma} \tag{1.3}$$

Neglecting the difference between the angles that the jet and the air turn through as they go through the oblique shock results in

$$\tau = \frac{\sin(\theta - \delta)}{\sin\theta}\frac{d_1^2}{4\Gamma} \tag{1.4}$$

Budzinski's thesis [3] gives an overview of the various analytical approaches taken

to the problem of modelling how the amount of circulation deposited on each half of the jet scales with the Atwood number and the shock strength. Budzinski found that his experiments agreed most closely with the model of Yang [32], and that model is the one which this author used, in a slightly modified form, to compare his results with those of Budzinski and Yang.

Yang proposed the following estimate of the initial circulation deposited on each half of the interface:

$$\Gamma = \frac{2d}{V_s}\frac{\Delta p}{\rho_2}\left(\frac{\Delta\rho}{\rho_l + \rho_h}\right) \tag{1.5}$$

The shock velocity, V_s, and the pressure jump across the shock, Δp, were re-interpreted for the three-dimensional case. The shock velocity was replaced by a velocity based upon the diameter of the jet just upstream of the shock and the time it took for the shock to move across the jet ($u_{air,1}\tan\theta$).

The pressure jump across the shock was replaced by the component of the shock pressure increase perpendicular to the flow upstream of the shock ($\Delta p\cos\theta$). This ensured that only the streamwise component of the vorticity generated by the oblique shock entered the calculation. The result of these modifications is

$$\Gamma = \frac{2d_1}{u_{air,1}\tan\theta}\frac{\Delta p\cos\theta}{\rho_2}At \tag{1.6}$$

The components of vorticity locally tangent to the interface between the jet and the freestream are non-zero in the three-dimensional case, but do not contribute to the development of the jet into a pair of vortices. Thus, they were left out of the calculations of the circulation and characteristic time.

Substitution of equation 1.6 into equation 1.4 gives the formula used to calculate the time scale for each experimental case

$$\tau = \frac{d_1\rho_2\, u_{air,1}}{8\,\Delta p\, At}\frac{sin(\theta-\delta)}{cos^2\theta} \tag{1.7}$$

1.3 Present Experiments

The interaction of a weak oblique shock wave with a coflowing light gas jet contains shear and turbulence effects not present in the two-dimensional investigations which have been done in the past. The goal of this study was to determine if the presence of shear and turbulence, along with other three-dimensional effects, would cause a significant deviation from the predictions of the unsteady two-dimensional experiments. The present investigation can be viewed as a link between the two-dimensional work of Budzinski and Yang and the study of injector models done by Waitz.

Figure 1.1 depicts the configuration used in these experiments. The jet was injected parallel to the freestream with a controlled mass flowrate and temperature. This fixed the velocity and density ratios between the jet and the freestream. All of the jets used in these experiments consisted of pure helium. Helium was chosen for its low density and benign chemical nature.

A variety of experimental techniques were used to collect information on the jet both up- and downstream of the oblique shock wave. Pitot and temperature probes were used to survey the flow field. They provided time averaged information on the jet cross sections at various downstream locations. The information from these measurements was used to deduce the average motion and deformation of the jet as it moved downstream.

Time resolved information was provided by schlieren photography and a planar Rayleigh scattering technique. The schlieren photos were taken from the side and were thus limited to providing data on the height of the jet and its vertical position in the tunnel. The planar Rayleigh scattering technique provided time resolved flow visualization of the jet cross sections by utilizing the scattering off of ice crystals present in the air but not in the helium. Non-uniform distribution of ice crystals in the test section prevented the Rayleigh scattering technique from being used to obtain direct information on the composition of the flow.

Chapter 2

Experimental Apparatus and Techniques

2.1 GALCIT Supersonic Wind Tunnel

The second leg of the GALCIT supersonic wind tunnel was used to perform all of the experiments in this study. It was operated in an open loop mode with ambient air from the laboratory being drawn into the test section through a filter and a two-dimensional Foelsch nozzle. Modifications to the tunnel in support of these experiments included redesign and replacement of much of the test section, installation of a helium injector and the supporting hardware, construction of a plenum with a high efficiency particulate air filter at the inlet, installation of a schlieren system, and installation of hardware to allow Rayleigh scattered light images to be obtained.

A side view of the test section is depicted in Figure 2.1. Flow is shown going

Figure 2.1 Side view of wind tunnel test section

from left to right. The ramps in the test section were changed to vary the strength of the weak oblique shock wave or eliminate it entirely. The injector was a cylindrical

tube with an outside diameter of 6.35 mm. It was positioned down the center of the nozzle, which had a throat height of 17.97 mm, an exit height of 50.8 mm, and a width of 63.5 mm. The injector tubing occupied 2.7% of the throat area. No correction was made to the nozzle contour to account for the presence of the small three-dimensional injector, although a simple correction to the contour was made assuming linear growth of the boundary layer downstream of the throat [5].

The top and bottom walls of the test section were not kept parallel; instead, they opened up at a small angle (one degree). This was done in an attempt to counteract the effects of the growth of the boundary layer and keep the static pressure constant along the length of the test section.

The top of the tunnel had a number of machine screws going through the outer frame to hold the ramps in place. Holes were drilled in the ramps so that a hollow machine screw could be installed and a tube inserted into the test section. This allowed the test section to be vertically traversed at every point where a support screw existed. These screws were place approximately 16.5 jet exit diameters apart. O-rings between the hollow screw and the tunnel, and between the hollow screw and the probe tube provided a seal between the test section and the lab.

A mount for the probe tube was constructed so that it could be slid along the length of the test section until it was aligned with the desired support screw location. Four set screws were then used to secure the mount in place. The tube support used a linear positioner driven by a micrometer to move the probe up and down inside the tunnel.

Figure 2.2 is a photo showing a side view of the tunnel test section. The black 7° ramp can be seen running along the bottom. Test section components were black anodized to minimize their reflectiveness. The micrometer driving the probe traverse can been seen at the top of the photo, and the pitot pressure probe for the 7° ramp can be seen in the test section. The top of the test section is shown ending before it actually does. There is a small lip to support the o-ring running horizontally along the top of the test section, but the space behind the o-ring has been hollowed out.

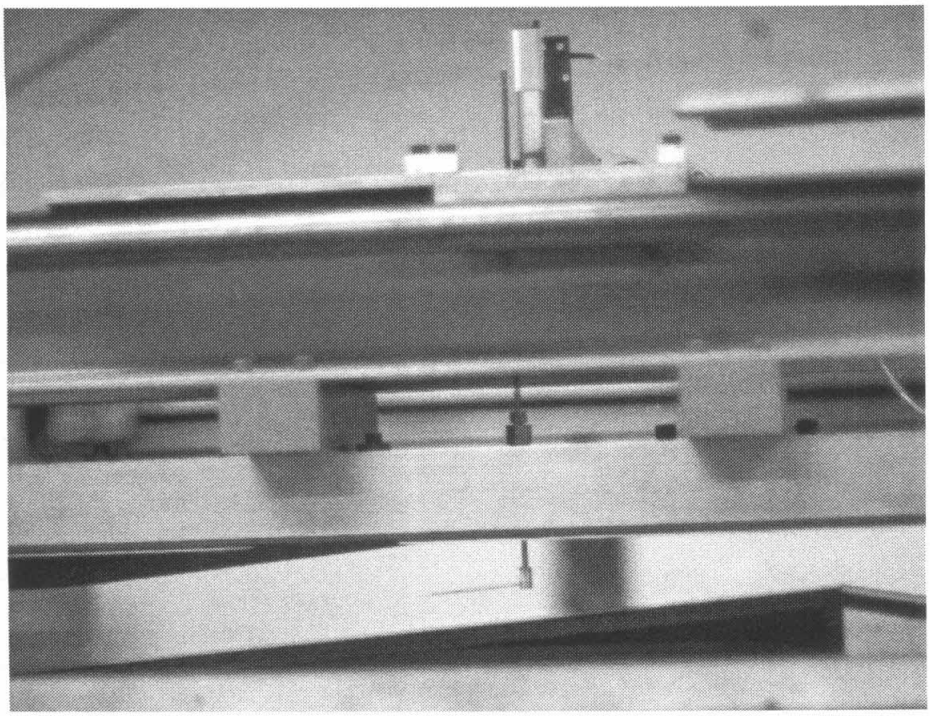

Figure 2.2 Photographic side view of tunnel test section

Figure 2.3 is a photo of the traverse mechanism. An arm attached to the probe tube (running diagonally from the center to the bottom right of the photo) was used to rotate the probe inside the tunnel. This allowed data to be collected off of the tunnel centerline. Calibrated marks on the plate below the arm allowed for accurate determination of the angle of the probe off of the tunnel centerline. The linear positioning transducer used to measure the probe position in the tunnel can also be seen toward the left side of the photo.

Optical access to the test section was provided by windows which ran along its length on both sides. A metal plate was manufactured which could replace either of the windows. Small tap holes (made by a number 78 drill) at regular intervals in the metal plate gave measurements of the static pressure at different downstream locations in the test section.

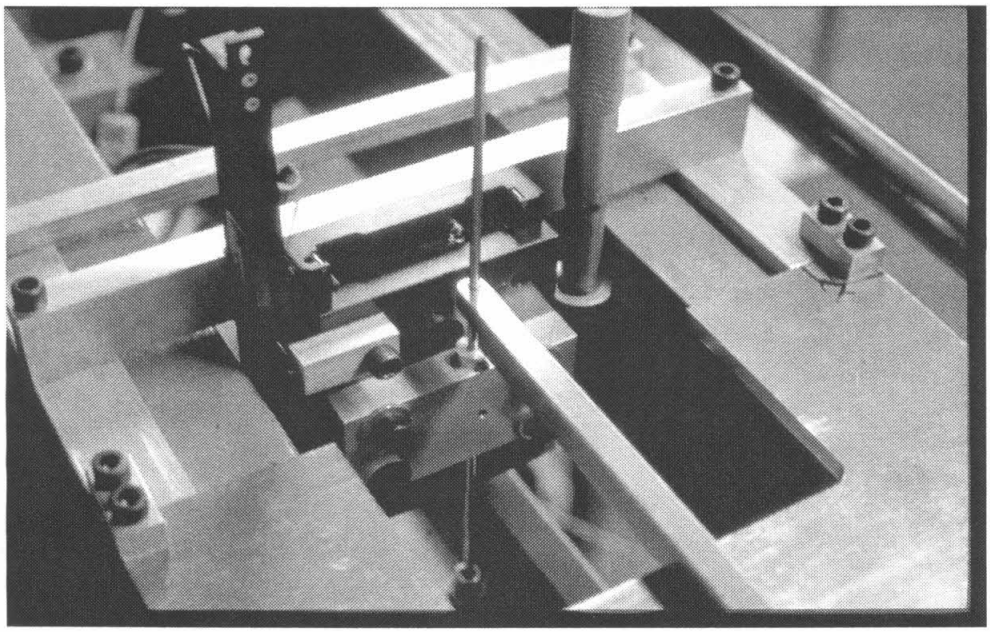

Figure 2.3 Photograph of probe traverse mechanism

2.2 He Injection System

The helium flowed through a long straight tube and into the test section of the wind tunnel. The tube was held firmly in the center of the two-dimensional nozzle through the use of six set-screws. Two tools designed for the purpose were used to ensure that the injector tube was centered in the nozzle.

The temperature and mass flowrate of the helium jet could be independently controlled through the use of a gas blending system. Two mass flow controllers were utilized. One provided room temperature helium to the injector, while the helium from the other passed through a liquid nitrogen bath on its way to the injector. Assuming that the static pressure of the helium at the jet exit was matched with that of the air freestream, the static density of the helium could be controlled only by changes to the static temperature of the helium. This follows directly from the ideal gas law.

Control of the jet's exit velocity was provided by changes in the helium mass flowrate. Changing the mass flowrate also changed the exit Mach number of the jet. Thus, the static temperature as well as the velocity was coupled to the mass flowrate. An additional complication was the significant heat transfer between the injector tubing and the helium. The heat transfer acted in a way which tended to prevent the helium velocity from dropping as the mass flowrate was reduced. As the mass flowrate through the injector was decreased, the lowest helium temperature achievable increased. The rate of increase in the minimum temperature was faster than the rate of decrease of the exit Mach number. This made it difficult to achieve lower helium velocities, since the temperature limit put a lower limit on the speed of sound in the helium, which in turn put a lower limit on the helium velocity for a given Mach number. See Appendix A for a more complete description of the helium injection system.

2.3 Flow Visualization Methods

There were two methods of flow visualization used in these experiments: the schlieren method and Rayleigh scattering of a laser light sheet off of ice crystals present in the flow. Both provided time resolved information on the flow in the tunnel.

2.3.1 Schlieren Flow Visualization

The source side of the schlieren system consisted of a Nanolamp spark source collimated through a series of achromatic lenses and a 20 cm diameter parabolic mirror. Two mirrors were used to position the collimated beam in the wind tunnel test section and send it to the collection optics. The collection optics used a 30.5 cm diameter spherical mirror and two camera lenses (100 mm and 50 mm focal lengths) to constrict the source beam onto the knife edge and focus the test section onto the film plane of a 35 mm camera.

The signal from the schlieren system was very weak due to the small size of the helium jet (exit diameter 4.65 mm) and the low density of the air and helium in

the test section (typically 0.11 of atmospheric for the wind tunnel air). This made it necessary to cut off most of the illumination from the spark source in order to visualize the jet. The film used for data collection was TMAX 400, and it was push processed to EI 1600 to compensate for the low light levels. Once the schlieren images were all obtained the negatives were scanned onto a Photo CD; this allowed direct manipulation of the images on a CD-ROM equipped personal computer.

2.3.2 Planar Rayleigh Scattering

The Rayleigh scattering technique used in these experiments relied upon the humidity present in the laboratory atmosphere. The water vapor present in the air drawn into the wind tunnel condensed as the flow accelerated through the nozzle and the static temperature dropped. The helium used was dry, so the jet fluid contained no ice crystals. The scattered signal from a light sheet cutting across the test section had contributions from scattering off of the helium atoms, the various air molecules, and the ice crystals. The air filter at the tunnel inlet stopped particles 0.2 μm or larger in size, which eliminated practically all dust from the freestream air; images from the ccd camera would occasionally show a bright spot from a dust particle, but almost all were dust free. The calculations of scattered intensity contained in Section B.1 show that the contributions from atomic and molecular scattering were negligible. Thus, as long as the ice crystals tracked the air flow reasonably well the scattered light images would be brighter in regions of higher air concentration and lower in regions of higher jet fluid concentration.

Considering the ideal case of a small spherical particle moving relative to a quiescent fluid, Melling [20] showed that if the drag on the particle was Stokesian the time evolution of its velocity could be described by the differential equation

$$\frac{du_p}{dt} = \frac{C}{24} Re_p C_d (u_f - u_p) \tag{2.1}$$

where

$$C = \frac{18\mu_f}{\rho_p d_p^2} \tag{2.2}$$

The subscript p denotes variables describing the condition of the particle, while the subscript f denotes properties of the surrounding fluid. Using the same drag law as Melling,

$$C_d = \frac{24}{Re_p(1 + 2.7\,Kn)} \tag{2.3}$$

equation 2.1 can be arranged to give

$$\frac{\rho_p d_p^2(1 + 2.7\,Kn)}{18\mu_f}\frac{du_p}{dt} + u_p = u_f \tag{2.4}$$

This is an inhomogeneous first-order equation with characteristic time

$$\tau_p = \frac{\rho_p d_p^2}{18\mu_f}(1 + 2.7\,Kn) \tag{2.5}$$

Using the larger of the ice crystal size results from Section B.2, along with suitable values for the properties of the surrounding fluid in the test section, resulted in a time constant of 0.50 μs in air and of 0.78 μs in the helium jet. These time constants indicate that the ice crystals in the test section accurately tracked the flow.

The collection side of the planar Rayleigh scattering system is shown in Figure 2.4. The same Candela SLL-1050M flashlamp pumped dye laser as was used by Budzinski [3] provided a laser pulse with an energy of 2–3 Joules and a width of 700 nanoseconds. The energy output of the laser was measured before each run using a Scientech volume absorbing disc calorimeter (model 38-0101). The dye used was Coumarin 480 (giving a peak output at a wavelength of 480 nm), and a prism tuner was present in the lasing cavity to narrow the bandwidth of the beam and vertically polarize it. The polarization of the incoming light is an important factor in calculating the scattering efficiency of particles ([28], also see Section B.1), and

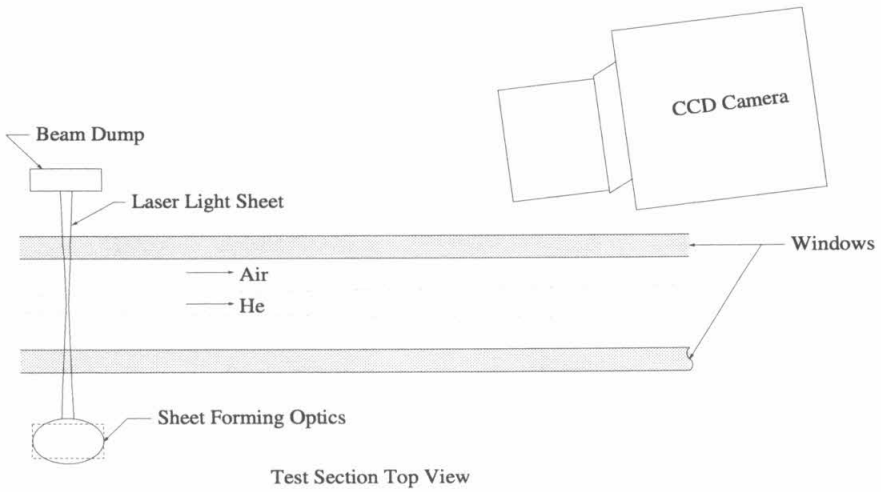

Figure 2.4 Rayleigh scattering collection optics

the configuration of the mirrors directing the beam into the test section necessitated the use of a half-wave plate to rotate the polarization of the beam. This beam was formed into a light sheet using a cylindrical lens, and that sheet was directed across the flow in the wind tunnel.

The scattered light was collected by a Photometrics Star I ccd camera aimed through a window on the side of the wind tunnel. The ccd array in the camera was cooled to -45 °C in order to minimize thermal noise. The camera used a 60 mm Nikon lens set to f/8. The high f-number was needed to get an adequate depth of field; the viewing angle of the camera caused one side of the image to be closer to the camera than the other. The lens was mounted to the camera using an off axis extension. This served the dual purpose of setting the desired magnification and attenuating the aberration caused by the off-axis viewing angle. The ccd array was 576 pixels wide and 384 pixels high, and each pixel was 20 μm on a side. The magnification of the collection optics was such that the area imaged by each pixel was 77 μm on a side. The camera's analog to digital converter had a 12 bit resolution.

An IBM compatible personal computer running the Linux operating system was used to control the ccd camera and the dye laser. A computer program was written

by the author to send commands over an IEEE-488 bus to the ccd camera and a Stanford Research Systems DG535 digital delay/pulse generator. Data collection began by setting the camera for a 0.1 second exposure time (the shortest possible for the shutter). The digital delay/pulse generator was set to send two triggers when a signal was received from the controlling computer. The first triggered the camera shutter to open; the second one, spaced 0.05 seconds later, triggered the firing of the flashlamp pumped dye laser. The camera's interface computer could hold only one frame at a time, so after each picture was taken a command was issued to the camera's computer to send the image over the IEEE-488 bus to the controlling Linux computer.

Scattering off of the window surfaces was a significant source of unwanted light when taking Rayleigh scattered images, and efforts were made to minimize it. Since it was unsafe to directly observe the beam from the dye laser, an argon-ion laser was used to align the optics before each run. A mirror was placed inside the cavity of the dye laser, and the argon laser aimed into it in such a way that the beam from the argon laser followed the same path as the beam from the dye laser.

2.4 Total Temperature Measurements

Fine wire thermocouple probes were used to make measurements of the temperature field in the test section. The design of the probes was based on those used by Juhany [14]. His design was modified by increasing the distance between the supports for the thermocouple wire. A different probe was made for each ramp set; this was done because the angle between the flow and the axis of the probe traverse changed with the ramp angle. For the maximum angle the streamwise position of the probe varied by no more than ± 0.13 exit diameters.

Figure 2.5 is a schlieren picture showing the flow over the probe for one of the cases studied. If the picture is rotated clockwise 90° the view is the same as that in Figures 2.1 and 2.2. The probe was moved from the top to the bottom to collect temperature information along a vertical line in the test section. The probe was

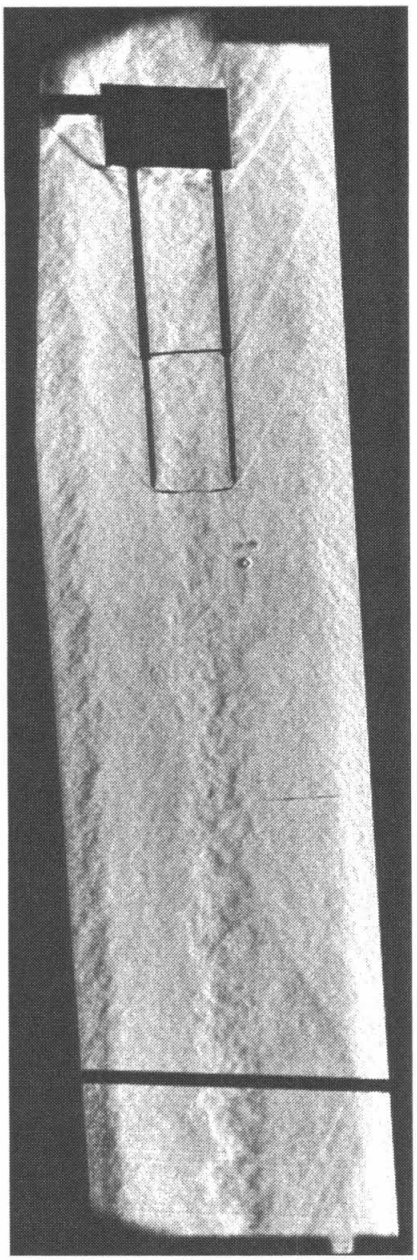

Figure 2.5 Schlieren for $u_{He}/u_{air} = 1.7$ case with 4.5° ramp showing temperature probe. Station number 3

then rotated (in 1 to 2 degree increments, depending on the resolution needed) and another traverse made. Measurements of the jet were made within 10.5° of the tunnel centerline. This resulted in a maximum positional error of (-0,+0.22) exit diameters in the streamwise direction.

The probes consisted of a support body holding two small tubes which extended forward in the streamwise direction. Thermocouple wires were run through the tubes to the front of the probe. The insulation was stripped off of the ends of the thermocouple wires and they were bent toward each other and glued in place. These then acted as the supports for the 0.05 mm diameter thermocouple wire which was welded to them. The thermocouple junction itself was positioned at the mid point between the supports. The length of the probe from its rotation axis to the thermocouple junction was 60.3 mm, the spacing between tubes was 12.7 mm, and the gap spanned by the fine thermocouple wire was approximately 6 mm. Type K thermocouple wire was used for all temperature measurements in the test section.

The wires from the temperature probe were fed through the tube holding the probe and out of the test section. A small amount of glyptol sealant was used on the threading of the probe and the feed-through tube to help hold them together. An ice bath held a reference junction, and the signal went to an Omega Omni Amp III signal amplifier before being sent to the data acquisition system.

Before each probe was used for the first time its response was checked using an ice bath and a boiling water bath. This check also verified the calibration of the amplifier and digital to analog converter electronics.

2.5 Pressure Measurements

The locations of the static pressure taps are represented by the small '+' marks in Figure 2.6. The tap positions were chosen to allow measurements to be made for all of the test section ramp configurations. Tygon tubing connected the outer side of each tap to a Statham model PA208TC-5-350 piezo-resistive pressure transducer. The transducer was powered using the supply circuit of an Omni Amp III; its signal

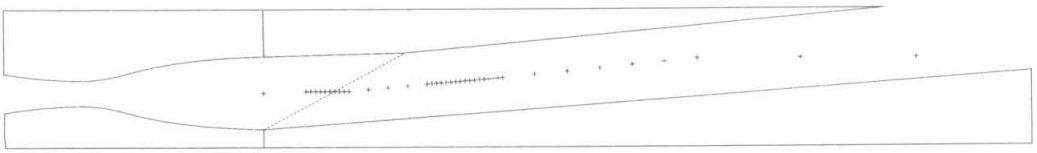

Figure 2.6 Position of static taps in the tunnel

was then amplified by a factor of 100 and fed to the input of the data acquisition system.

The pitot pressure measurements were made using a probe which resembled the temperature probe except with only one hollow tube extending forward from the body. A pitot probe can be seen installed in the test section in Figure 2.2. It was threaded and screwed onto the tube holding it. A small amount of glyptol placed on the threads before tightening ensured that there was no leak at that junction.

The length of the probe from the rotation axis of the supporting tube to the tip was the same as for a temperature probe, 60.3 mm. The outer diameter of the tubing at the probe tip was 0.508 mm, and its inner diameter at that point was 0.254 mm. The other end of the probe was connected to a Statham model PA208TC-15-350 piezo-resistive pressure transducer.

The only difference between the pitot pressure transducer and the one used for static pressure measurements was the effective range (0-15 psi and 0-5 psi absolute, respectively). Their connecter interfaces were identical, and, since they were never in use at the same time, the same electronics were used to run both. The pressure transducers were calibrated using a vacuum pump and a vernier equipped mercury manometer. Their response was measured to be linear within 0.3% at the worst, and a straight line fit to the calibration data was used to convert all experimental data to pressures.

2.6 Data Acquisition System

The acquisition of the Rayleigh scattered images has been described in the Section 2.3.2. Temperature and pressure data was collected using a Metrabyte DAS 20 analog to digital and digital to analog converter board mounted in an IBM compatible personal computer. The temperature and mass flow control system for the helium injector also used a DAS 20 mounted in a PC.

The output of the signal amplifier connected to the temperature transducer was connected to one input channel of the DAS 20. The pressure transducer required two channels of input. One was the voltage to the transducer's bridge circuit, and the other was the output from that circuit.

The linear position transducer used to measure probe positions within the test section was based upon a slide potentiometer. The power to the potentiometer was provided by one of the Omni Amp III's, and that voltage was fed to a DAS 20 input channel. The output from the transducer was fed to another channel, and the ratio was used to determine the probe position. This transducer was calibrated using the micrometer on the probe traverse, and its response was found to be linear within 0.5%.

Various computer programs resident on the PC's controlled the DAS 20's in the collection of data. The program used to run the mass flow controllers is described in Section A.2 and listed in Section A.3. The programs to collect temperature and pressure data were much simpler.

For the case of temperature data collection, the computer program continuously displayed the current temperature reading. Once a key was struck, it would collect voltage data for the position transducer and set up the DAS 20 to collect thermocouple voltage readings as directed. The measurements were usually made at the rate of 4000 Hz for the duration of 1 second. Calculations and experiments on the frequency response of the thermocouple probe are described in Section 3.2. These readings were then converted to a temperature and then averaged. The voltages from the position transducer were converted to position data, and finally the position and temperature data was output to a file.

The operation of the program to collect pressure data was essentially identical to that for the temperature probe. A simple calculation of the time response of the pitot pressure probe gave a time constant of about 0.1 seconds. Pressure data usually consisted of an average of 400 readings taken over the period of one second.

2.7 Cases Studied

Two different jet conditions and three different ramp configurations were studied. Table 2.1 contains a summary of the different jet exit conditions used. Section A.1

u_{He}/u_{air}	Mach No.	u (m/s)	ρ (kg/m^3)	T (K)	T_0 (K)	$\dot{m}$ (slpm)	Re
1.32	1.13	778	0.020	139	198	50.0	5900
1.70	1.50	1000	0.022	125	219	92.7	9000

Table 2.1 He jet properties at injector exit

describes how these were obtained. The Reynolds number is based upon the exit diameter of the jet.

The velocity ratio 1.7 jet was studied with no ramp, a 4.5° ramp, and a 7.0° ramp, while the velocity ratio 1.3 jet was studied with the no ramp and 7.0° ramp configurations. The freestream conditions with no ramp, a 4.5° ramp, and a 7.0° ramp are summarized in Table 2.2. The convective Mach numbers for the two

	Mach No.	u (m/s)	ρ (kg/m^3)	T (K)	T_0 (K)	p (Pa)
no shock	2.39	588	0.133	151	323	5780
after 4.5° turn	2.22	568	0.161	163	323	7510
after 7.0° turn	2.12	555	0.178	170	323	8720

Table 2.2 Freestream properties for various tunnel configurations

jets were calculated using the formula $M_c = \frac{u_{He}-u_{air}}{a_{He}+a_{air}}$ with the appropriate jet and freestream properties, and they were found to be 0.2 for the 1.32 velocity ratio jet and 0.46 for the 1.7 velocity ratio jet.

An item of note in Table 2.2 is the higher than expected stagnation temperature. This was caused by the condensation of the water in the laboratory air as both were accelerated through the nozzle [26]. Although the humidity of the laboratory air was not explicitly controlled, the laboratory was located in the building's basement, which tended to keep the humidity relatively constant. It was measured during each experimental run using a psychrometer, and a value of 0.009–0.010 kg_{H_2O}/kg_{air} was typical.

The information contained in Tables 2.2 and 2.1 was combined with data on the jet at its intersection with the shock to get estimates for the circulation deposited on the interface and characteristic times for the different flows. Table 2.3 contains a summary of the results from these calculations. The term $\hat{x}$ is the distance (in

ramp angle	u_{He}/u_{air}	$M' \sin\theta$	ρ_l/ρ_h	$\Gamma(m/s)$	$\tau(\mu s)$	$\hat{x}$
4.5°	1.7	1.11	0.185	0.324	53.6	9.15
7.0°	1.32	1.17	0.188	0.426	25.9	3.81
7.0°	1.7	1.17	0.185	0.516	31.1	5.30

Table 2.3 Time constant calculations using Yang's model

jet exit diameters) that the flow must travel in the streamwise direction for it to develop 1 τ in time.

Table 2.4 is a matrix which represents where data were collected for each of the

		x/d					
ramp angle	u_{He}/u_{air}	16.4	32.8	49.2	66.4	83.6	99.9
0°	1.32	x	x	x	x	x	x
0°	1.70	x	x	x	x	x	x
4.5°	1.70	x	x	x	x	x	
7.0°	1.32	x	x	x	x		
7.0°	1.70	x	x	x	x		

Table 2.4 Data collection matrix

cases studied. Not every possible measurement was made at every place marked with

an 'x,' and some measurements were made more often, but the table gives a general outline of where data were taken. The decrease in the furthest distance downstream data were taken as the ramp angle was increased was due to the effective shortening of the test section by the steeper ramps.

Chapter 3

Pressure and Temperature Measurements

Both the temperature and pitot pressure surveys of the flow field provided time averaged information on the jet cross section at various downstream locations. In the case of no shock wave, these cross sections showed the growth of the jet as it moved downstream. In the cases with a shock wave they also showed the jet being split down the middle and forming into two vortices as it moved downstream. All cross sectional views are taken looking upstream with the jet coming out of the page toward the observer. The coordinate system for these pictures has the x-axis coming straight out of the page, the y-axis going toward the top of the page, and the z-axis going to the left of the page.

It is important to remember that in the cases with a shock wave the flow downstream of the shock has been compressed. Thus, any comparison of the size of the jet cross section downstream of a shock with the size of the jet cross section at the same station for the case without a shock must account for this compression. This is shown in Figure 1.1 and discussed in Section 1.2.3. The result is that in order to get the equivalent total area the cross sections for the cases with a shock wave must be stretched along the y-axis by the amount $\frac{\sin(\theta-\delta)}{\sin\theta}$. None of the plots in this section have had a scaling applied to them. To do so would distort the shape of the jet. The area correction was applied before generation of the area comparison plots in Figures 5.1 and 5.2.

3.1 Pressure Measurements

Chapter 2 describes the apparatus used to obtain static and pitot pressure measurements. The static pressure measurements were needed to verify the design of the tunnel. The cancellation of the oblique shock by the expansion on the top tunnel wall was very sensitive to the position of the corner on the top wall. The test section blocks were designed using the most conservative estimate for the location of the corner. The blocks were then installed and the tunnel run. Schlieren photos and static pressure data then provided the information needed to make a correction to the position of the corner.

Pitot pressure measurements of the flow field had the advantage that the probe was small and sturdy. The temperature probe was relatively large and caused the tunnel to unstart when it was placed at the locations furthest downstream. The pitot probe did not affect the flow in the tunnel nearly so much, and if the tunnel did unstart the probe was strong enough to withstand the resultant stresses on it.

3.1.1 Static Pressure Measurements

A plot of all static pressure measurements is in Figure 3.1. They form three groups, the lowest one being for the two cases with no ramp. The one in the middle is static data for the single case with a 4.5° ramp, and the top two are data sets that were taken with a 7.0° ramp in the test section.

Referring to Table 2.4, the static pressure values of Figure 3.1 can be compared with the downstream limit of where data was taken. For the cases with no ramp, data was taken all of the way to the x/d=100 downstream station. The experiments with the 4.5° ramp went to the x/d=83.6 station, and the experiments with the 7.0° ramp stopped at x/d=66.4. Thus, the sudden increase in static pressure seen in the data for the 7.0° ramp downstream of the x/d=66.4 station is not of importance. It is due to the deceleration of the flow after it passes the end of the ramp.

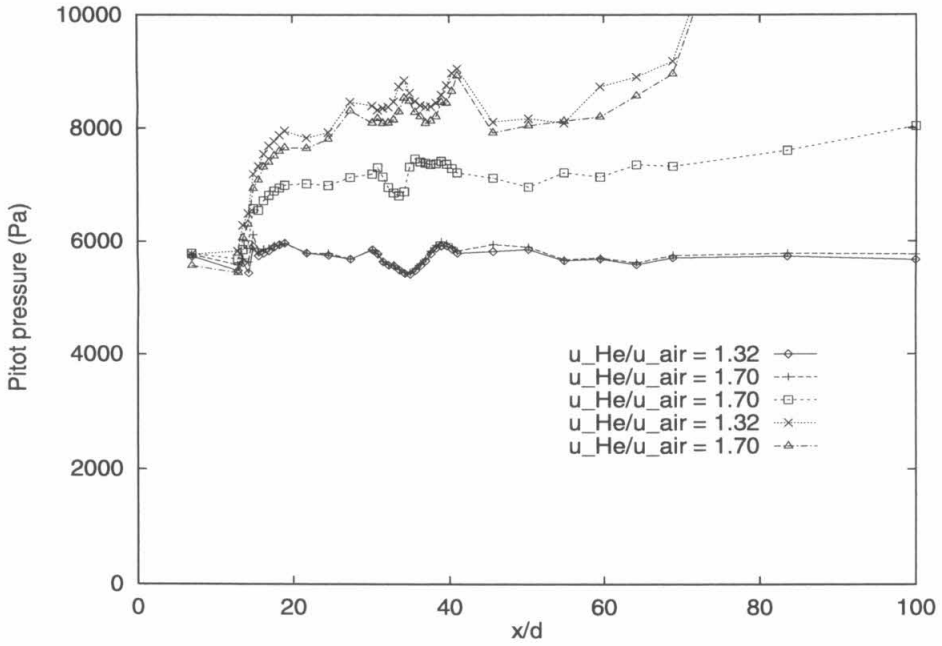

Figure 3.1 Plot of static pressure data

3.1.2 Pitot Pressure Measurements

The different ratios of specific heat for air and helium made it impossible to get quantitative information on the jet's composition using pitot probe data. The time constant of the pitot probe was lower for helium than it was for air (primarily due to the low atomic weight of helium). Assuming discrete blobs of relatively unmixed fluid moving past the probe tip, this meant that the average pitot pressure read by the transducer was skewed slightly in favor of the helium pressure. See Appendix C for a description of how the pressure data was reduced to give the jet cross sections described below. The percentage values listed on the contours are based upon the ratio $\frac{(p-p_{min})}{(p_{max}-p_{min})}$.

The Mach number of the helium at the jet exit was less than that of the air, but its static pressure was matched with that of the air. The Mach number of the helium was smaller than that of the air by a large enough margin that the stagnation

pressure in the helium jet was much smaller than that of the air. If the air and the helium had the same Mach number as well as static pressure then the helium's stagnation pressure would have been higher than that of the air due to the higher γ for helium. Pitot pressure profiles taken along the y-axis right at the injector exit are shown in Figure 3.2. The notches in the profiles to either side of the jet were

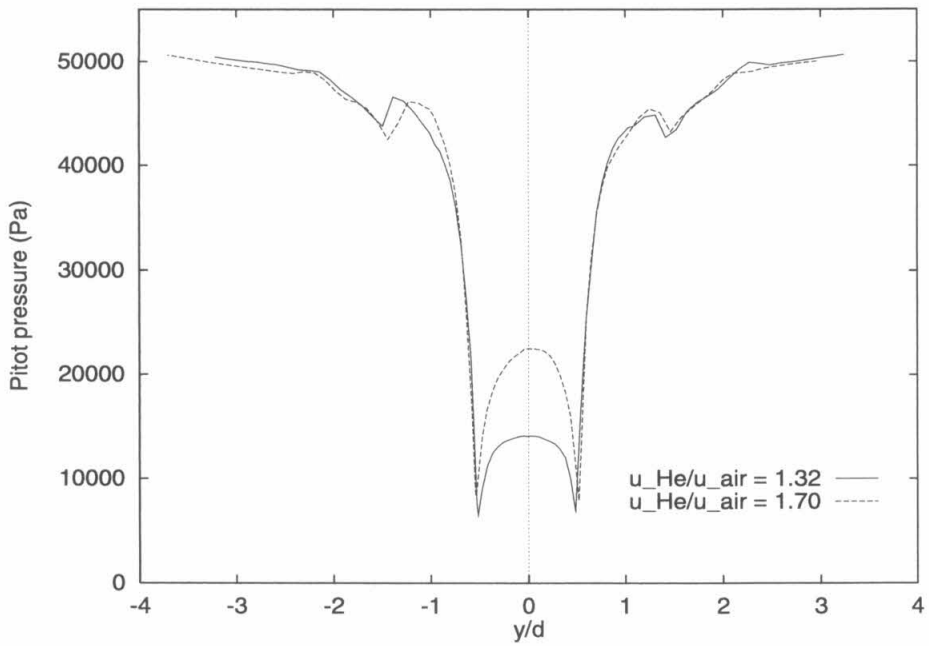

Figure 3.2 Pitot pressure at jet exit

caused by the waves coming off of the contraction on the outside of the injector 1.5 diameters upstream of its exit.

Figures 3.3 through 3.8 are a series which show cross sections of the jet for the case of no ramp and a velocity ratio of 1.3. They were taken approximately every 16.5 diameters in the streamwise direction. The jet is seen to slowly spread as it moves downstream. There is a slight flattening of the jet along the y-axis; it is suspected that this was due to the presence of the cylindrical injector tube in the two-dimensional nozzle.

The cross sections shown in Figures 3.9 through 3.14 are also for the tunnel

configuration with no ramp, but the helium/air velocity ratio for this case was 1.7. Comparison of Figures 3.3 and 3.9 shows that the jet profile was fuller for the higher velocity ratio. This trend continued, with the difference becoming quite noticeable by the x/d=49.2 downstream station. However, the higher Mach number for the velocity ratio 1.7 cases caused a higher stagnation pressure for the helium jet (see Figure 3.2). The minimum pitot pressure of the data shown in Figure 3.9 is 20000 Pa, while the minimum pressure for the data in Figure 3.3 is 17400 Pa. They have maximum pressures of 49700 Pa and 48800 Pa, respectively. By the time the jet reached 100 diameters downstream the lowest pitot pressure was 36900 Pa for the $u_{He}/u_{air} = 1.32$ case and 34500 Pa for the $u_{He}/u_{air} = 1.7$ case. The maximum pressures recorded at x/d=100 for those cases were 47800 Pa and 47900 Pa, respectively.

The passage of the flow through the shock changed the properties (*e.g.* velocity, pitot pressure, static temperature) of the jet and the freestream by different amounts. This prevented comparison of the actual pitot pressure values for the shock and no shock cases.

When a ramp was installed in the test section, the shock it generated intersected the jet approximately 17 diameters downstream of the injector exit. Figures 3.3 and 3.9 are of particular interest since they show what the helium jets looked like just before they interacted with the shocks. There is no trace in either picture of the injector tube wake seen at y/d=$\pm$0.5 in Figure 3.2.

Figures 3.15 through 3.19 show the jet contours for the case with a 4.5° ramp and a velocity ratio of 1.7. Figure 3.15 is a contour of the $u_{He}/u_{air} = 1.7$ jet taken at x/d=16.4 with the 4.5° ramp installed. The shock can be seen just starting to pass through bottom the jet at about 2.8 jet diameters from the bottom of the picture. Figures 3.16 through 3.19 show the jet splitting into two distinct halves and beginning its development into a pair of vortices as it moves downstream.

For the test section configuration with a 7.0° ramp Figures 3.20 through 3.22 show the jet cross sections for the 1.32 velocity ratio case, and Figures 3.23 through 3.25 show the same cross sections for the 1.7 velocity ratio case. These show the jet

splitting into two distinct regions much more quickly than it did after going through the shock generated by the 4.5° ramp, as predicted by the characteristic times in Table 2.3. For the 7.0° cases, cross sections at the same downstream station for both velocity ratios appear to have the same general shape, which indicates that shear does not, on average, appear to affect the development of the jet after the shock.

The agreement is perhaps slightly better than what would be expected from looking at the time constants and characteristic streamwise distances in Table 2.3. The calculations for $\hat{x}$ were based upon the average velocity between the jet and the freestream, which was higher for the 1.7 velocity ratio cases. Thus, the characteristic distance for those cases was longer, as the flow had to travel further downstream to achieve the same development in time as for the otherwise equivalent $u_{He}/u_{air} = 1.32$ flow. The 1.7 velocity ratio jet had a slightly different Atwood number and radius compared with the 1.32 velocity ratio jet at the point where it interacted with the shock, and both also contributed to its higher value for $\hat{x}$.

3.2 Temperature Measurements

The temperature probes measured the recovery temperature of the flow at a fine wire thermocouple junction. The junctions were spot welded by the author and inspected under a binocular microscope. They were not much larger than the surrounding thermocouple wire in size and close to the cylindrical shape of the fine wire they were made from.

Behrens [1] described the method used to obtain the recovery factor for a circular cylinder based upon the Mach number and stagnation Reynolds number of the flow over it. This recovery factor could then be applied to the temperature measured by the probe to get the stagnation temperature of the flow. The recovery factor for the probe was calculated to be 0.95 for the freestream, 0.97 for the exit conditions of the $u_{He}/u_{air} = 1.32$ jet, and 0.96 for the exit conditions for the $u_{He}/u_{air} = 1.7$ jet.

Condensation and subsequent evaporation of ice crystals caused problems with

getting quantitative data from the temperature measurements. The ice crystal size calculations in Section B.2 agree with those of Thoman [27], but there is disagreement with his prediction that the ice crystals would not evaporate in the flow around the fine wire thermocouple due to its small size. The amount of vaporization around the thermocouple was found to vary with downstream distance as well as with the humidity of the laboratory air. The heat of vaporization for the typical amount of the water in the lab air was sufficient to give temperature changes in the freestream of as much as 25 K, although generally they were in the range of 10 to 15 degrees. The variation within a cross section was much less, but the variation from cross section to cross section was too much to make calculation of the stagnation temperatures meaningful. The recovery factor correction was applied to all temperature measurements made at the jet exit since those measurements were used to obtain other jet properties, and the pure jet fluid at the jet exit had no ice in it.

Conduction along the thermocouple wire was a concern since the wire length was of the same order of magnitude as ten times the cold length of the probe [21]. See Appendix D for a discussion of this and calculation of the thermocouple time constant and its measurement using an electronic circuit. The time constant of the temperature probes was measured to be similar in air and helium, which meant that the average temperature measured was not skewed greatly toward that of one stream or the other.

The problem of conduction along the thermocouple wire was addressed by looking at an equation for steady state heat transfer along the wire

$$\frac{4h}{d}(T_g(y+y') - T(y,y')) + \frac{d}{dy'}\left(k(y')\frac{dT(y,y')}{dy'}\right) = 0 \tag{3.1}$$

In the above equation y′ is the position relative to the wire, y is the position relative to the tunnel, d is the wire diameter, h the convective heat transfer coefficient, and k the thermal conductivity of the wire. The temperature probe always measured the temperature at y′=0 and was moved along y. The thermal conductivity varied across the junction, so k was a function of y′.

The idea for the use of equation 3.1 was that knowing T(y,0) for many y (since the probe was moved up and down in the tunnel) would allow the reconstruction of $T_g(0+y)=T_g(y)$. Kubota [16] derived a method to correct the temperature measurements using this technique. It was selectively applied to the temperature data, and the correction found to not be appreciable except at the injector exit, where the gradients were the highest. Since only the centerline temperature value was used in calculating jet properties, no temperature correction was applied to any data.

Figures 3.26 through 3.31 show cross sections of the jet temperature for the case with no shock and a velocity ratio of 1.32 (the percentage values for all of the temperature contours are based upon the ratio $\frac{(T-T_{min})}{(T_{max}-T_{min})}$). The same no shock configuration with a jet velocity ratio of 1.7 is depicted in Figures 3.32 through 3.37. These figures show the same general properties as the pressure contours previously discussed. The maximum temperatures measured at x/d=16.4 were in the range of 296 K, and the minimum temperatures there were 213 K for the $u_{He}/u_{air} = 1.32$ jet and 236 K for the $u_{He}/u_{air} = 1.7$ jet. By the time the jets reached 100 diameters downstream the freestream recovery temperature was measured to be 290 K, and the minimum temperatures were found to be 270 K for the velocity ratio 1.32 jet and 267 K for the velocity ratio 1.7 jet. The decrease in freestream temperature from x/d=16.4 to x/d=100 was most likely due to the change in ice crystal size with downstream location.

Figures 3.38 to 3.42 are temperature contours from the 4.5° ramp, $u_{He}/u_{air} = 1.7$ case; Figures 3.43 and 3.44 are data from the 7.0° ramp, $u_{He}/u_{air} = 1.32$ runs; and Figures 3.45 and 3.46 are from the 7.0° ramp, $u_{He}/u_{air} = 1.7$ runs. Temperature data were not taken at the last downstream station (x/d=66.4) with the 7.0° ramp because the temperature probe was too large and unstarted the tunnel when pushed down into the freestream. The sizes and shapes of the contours from the 7.0° ramp runs agree well with their corresponding pitot pressure contours, but the contours from the last two stations (x/d=66.4 and x/d=83.6) for the 4.5° ramp case do not match well with the corresponding pressure data. This is believed to be due to noise in the temperature measurements caused by the low quality of the flow around the

probe at these downstream stations. The low flow quality in these cases was caused by the separation of the boundary layer, which was induced by the presence of the temperature probe. The temperature probe was much larger than the pitot probe, so it induced the boundary layer separation sooner than the pitot probe.

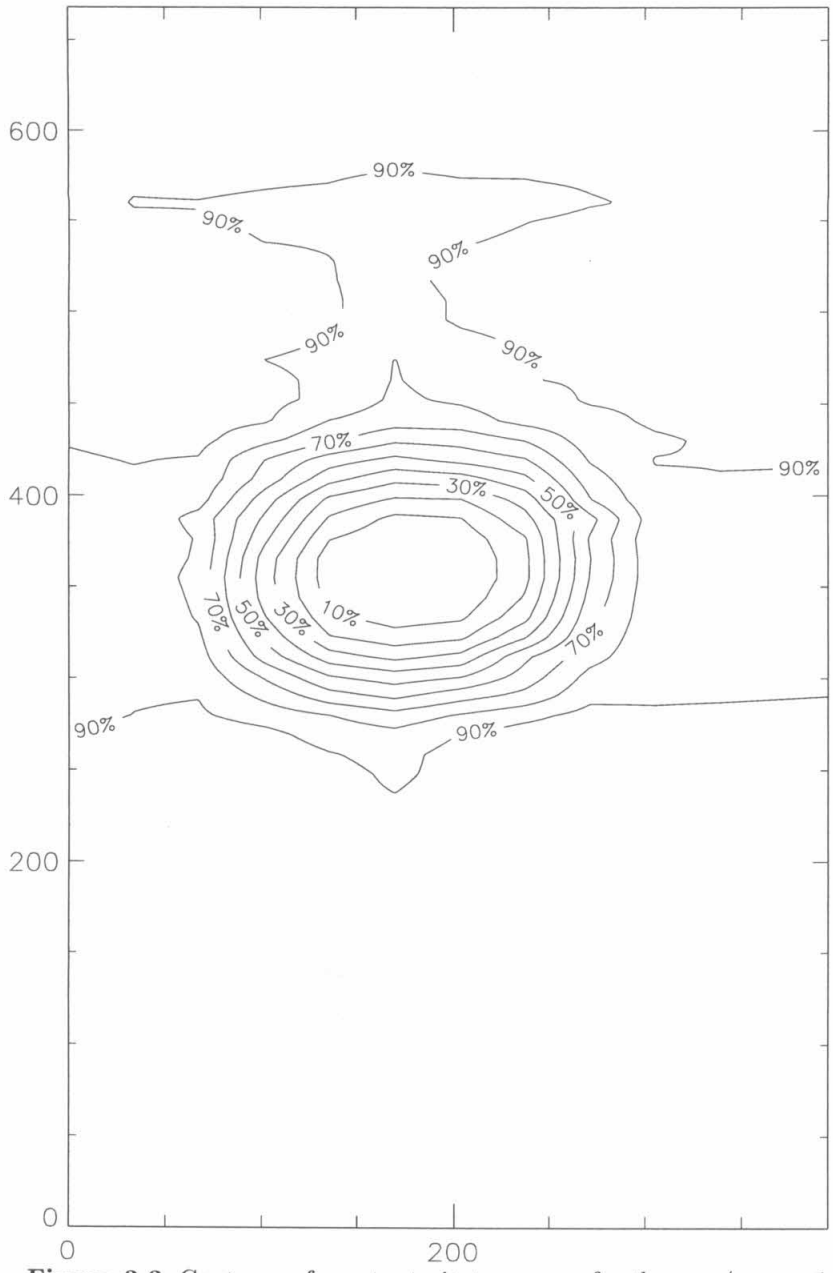

Figure 3.3 Contours of constant pitot pressure for the $u_{He}/u_{air} = 1.32$, no ramp case at $x/d = 16.4$. Axes are in hundredths of jet exit diameters. $p_{max} = 48800$ Pa, $p_{min} = 17400$ Pa

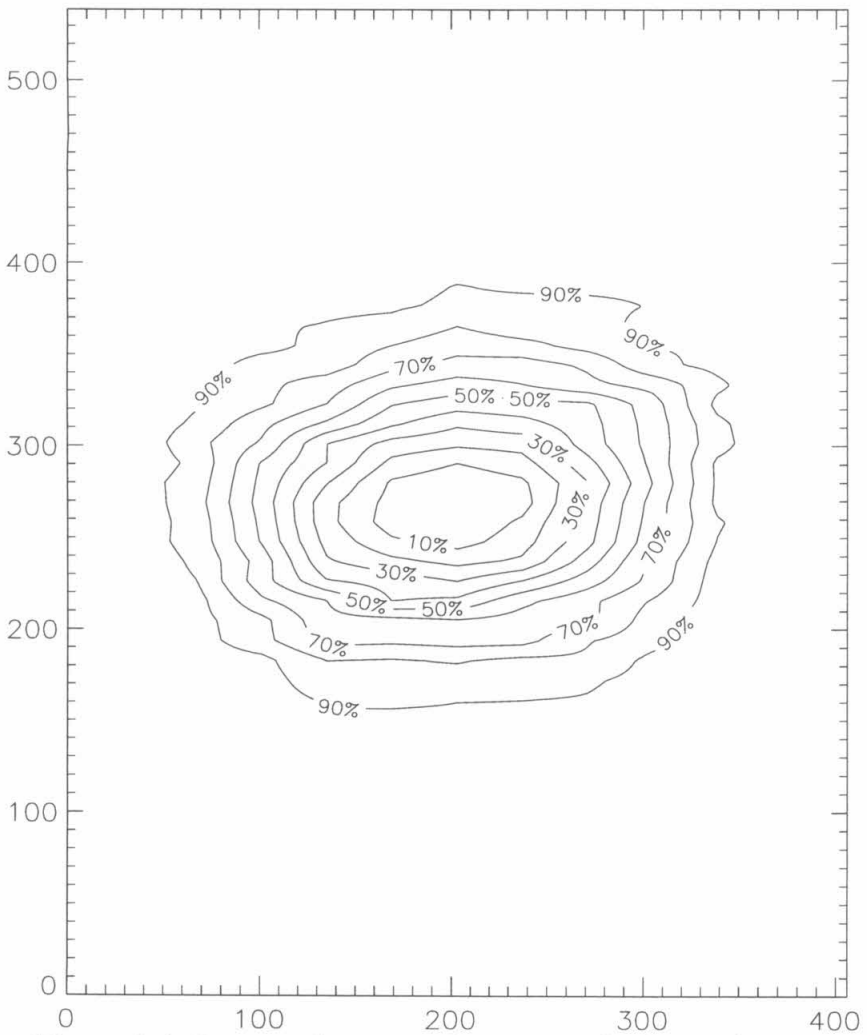

Figure 3.4 Contours of constant pitot pressure for the $u_{He}/u_{air} = 1.32$, no ramp case at $x/d = 32.8$. Axes are in hundredths of jet exit diameters. $p_{max} = 48600$ Pa, $p_{min} = 23000$ Pa

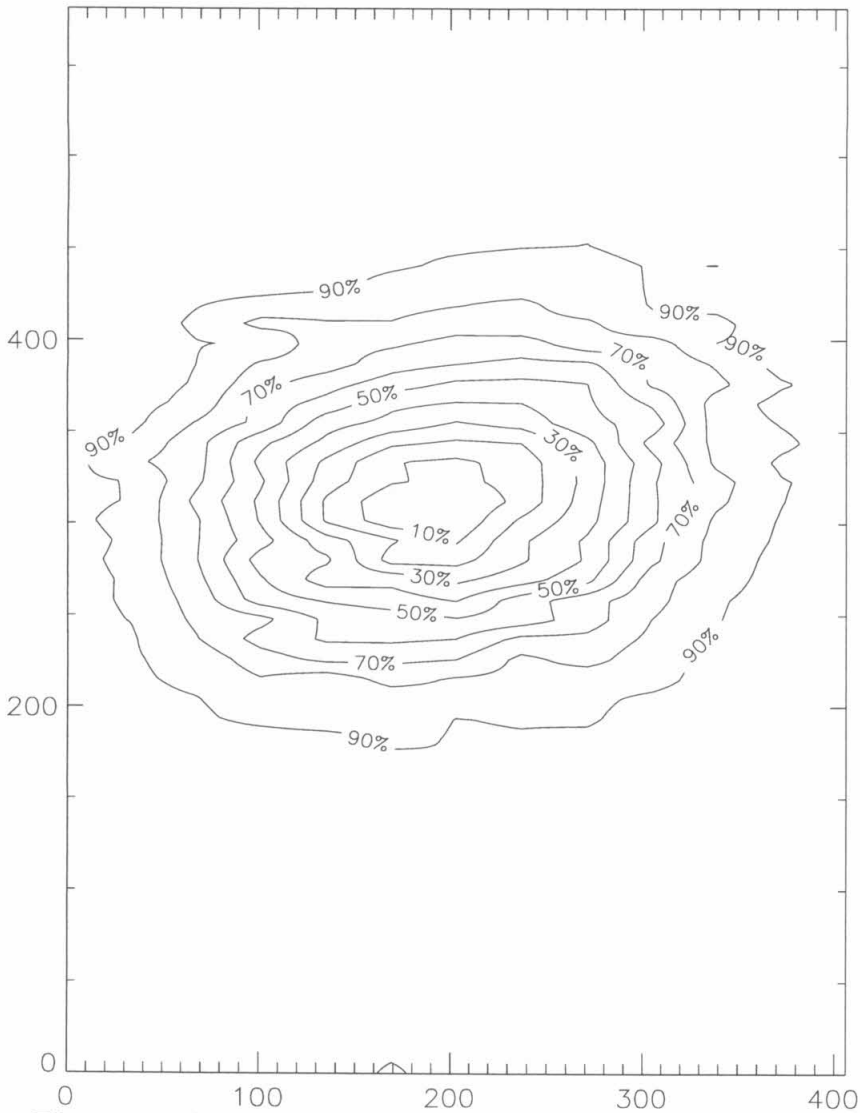

Figure 3.5 Contours of constant pitot pressure for the $u_{He}/u_{air} = 1.32$, no ramp case at $x/d = 49.2$. Axes are in hundredths of jet exit diameters. $p_{max} = 49000$ Pa, $p_{min} = 27300$ Pa

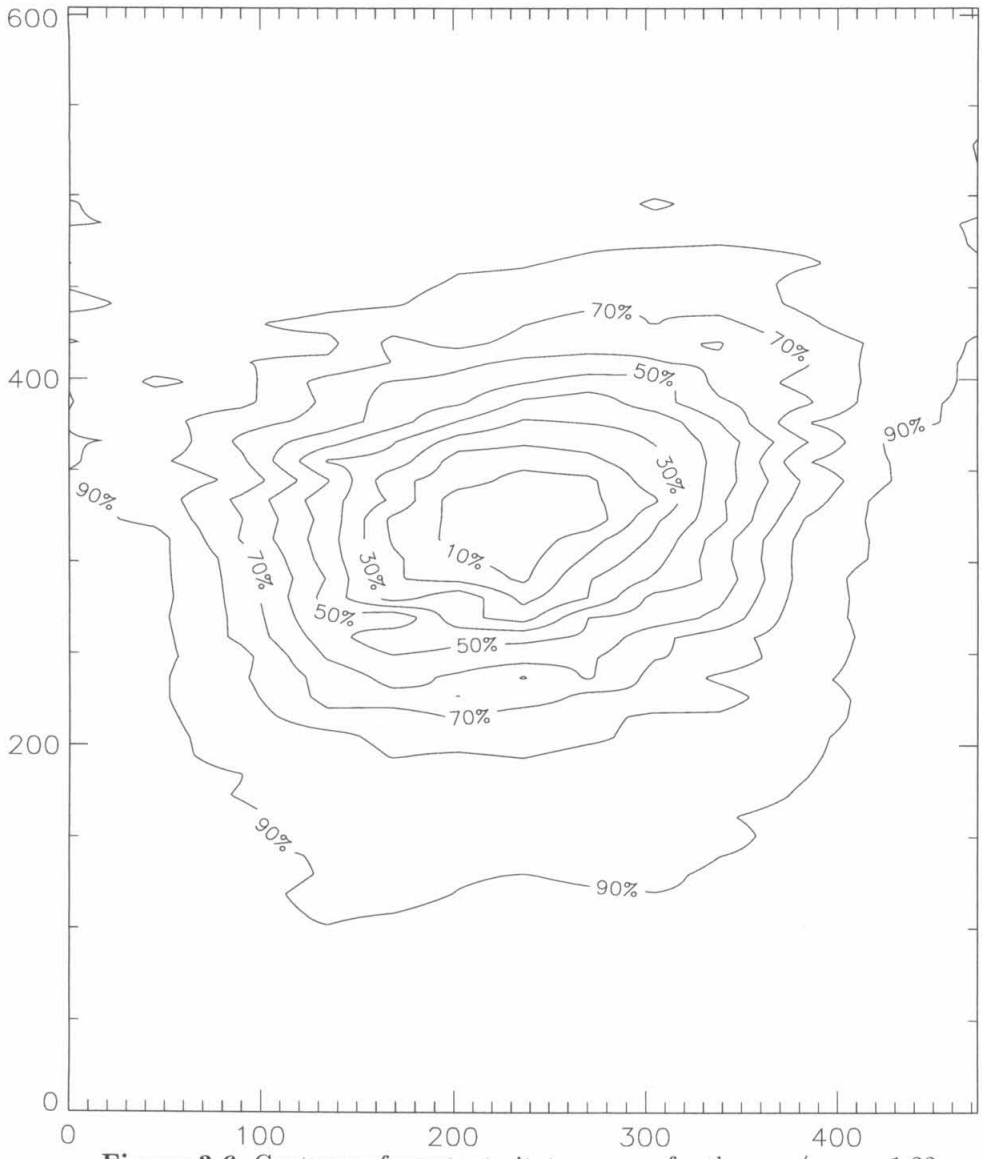

Figure 3.6 Contours of constant pitot pressure for the $u_{He}/u_{air} = 1.32$, no ramp case at $x/d = 66.4$. Axes are in hundredths of jet exit diameters. $p_{max} = 49000$ Pa, $p_{min} = 33000$ Pa

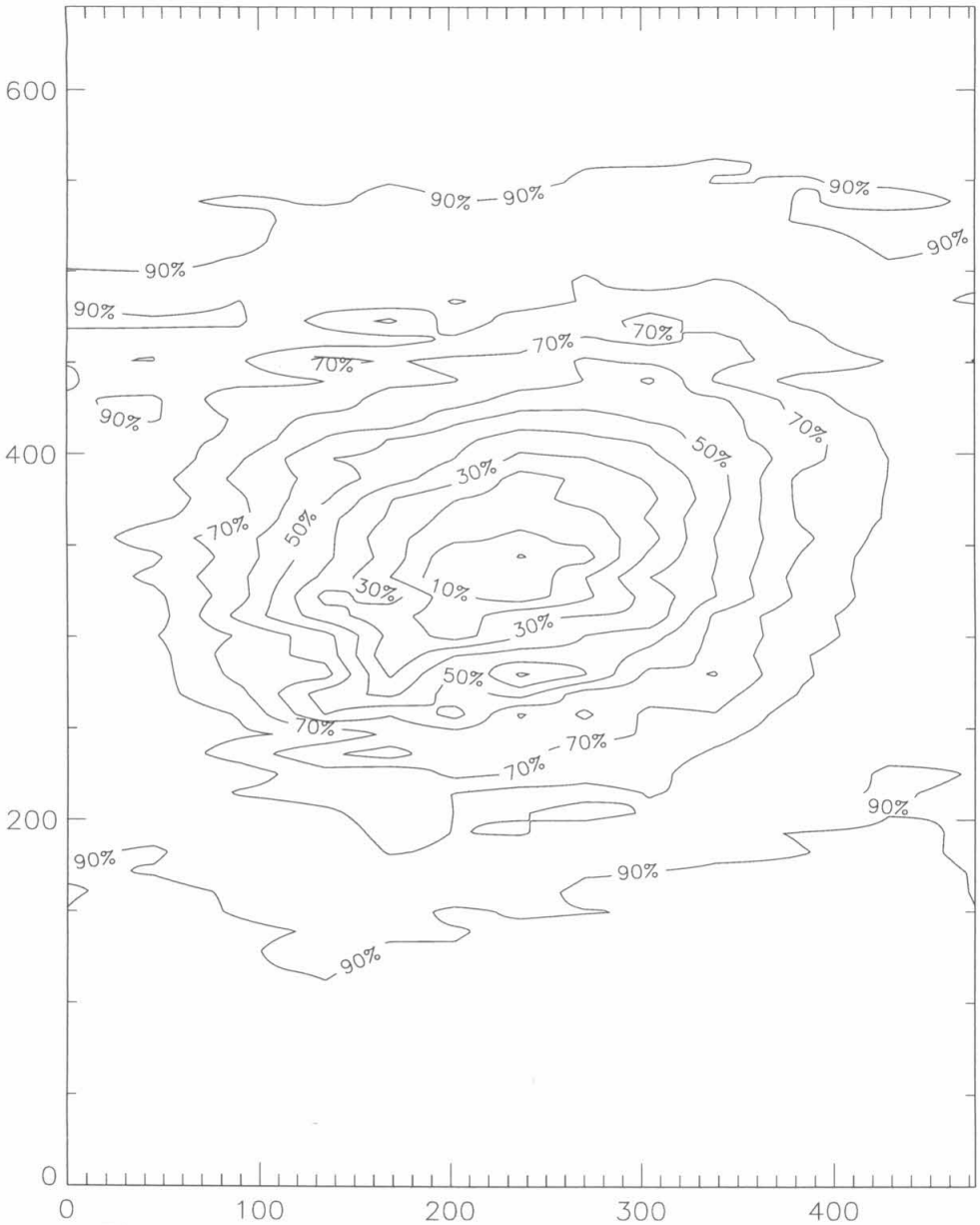

Figure 3.7 Contours of constant pitot pressure for the $u_{He}/u_{air} = 1.32$, no ramp case at $x/d = 83.6$. Axes are in hundredths of jet exit diameters. $p_{max} = 48400$ Pa, $p_{min} = 34800$ Pa

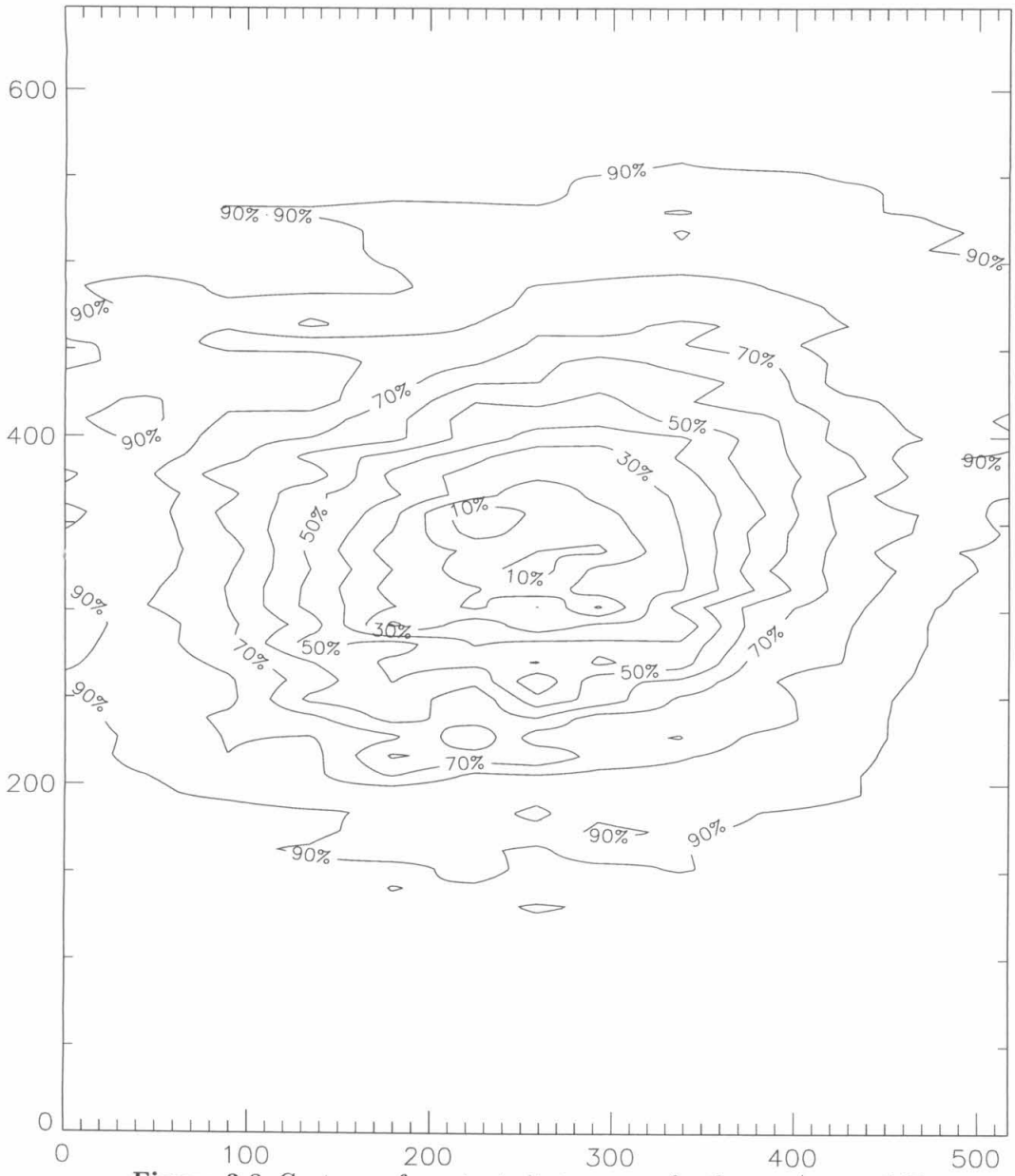

Figure 3.8 Contours of constant pitot pressure for the $u_{He}/u_{air} = 1.32$, no ramp case at $x/d = 99.9$. Axes are in hundredths of jet exit diameters. $p_{max} = 47800$ Pa, $p_{min} = 36900$ Pa

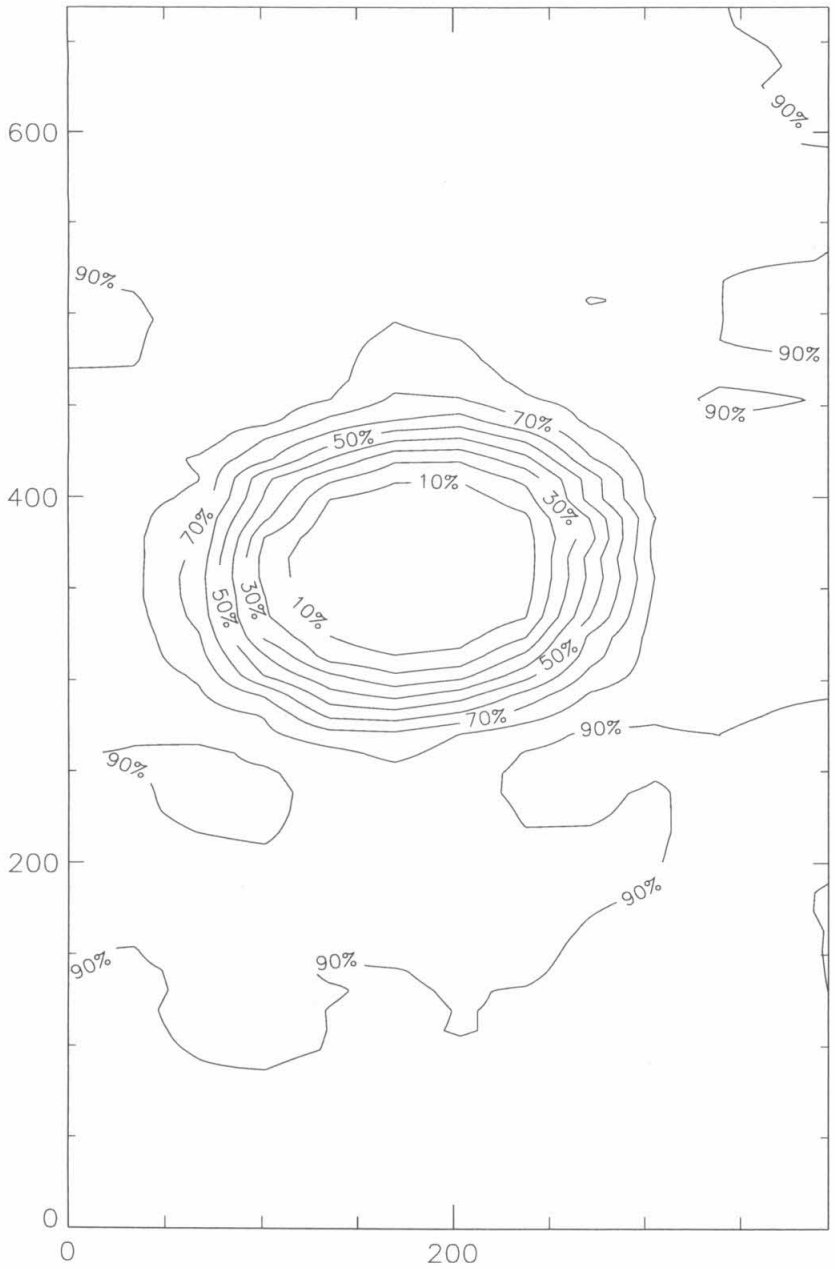

Figure 3.9 Contours of constant pitot pressure for the $u_{He}/u_{air} = 1.7$, no ramp case at $x/d = 16.4$. Axes are in hundredths of jet exit diameters. $p_{max} = 49700$ Pa, $p_{min} = 20000$ Pa

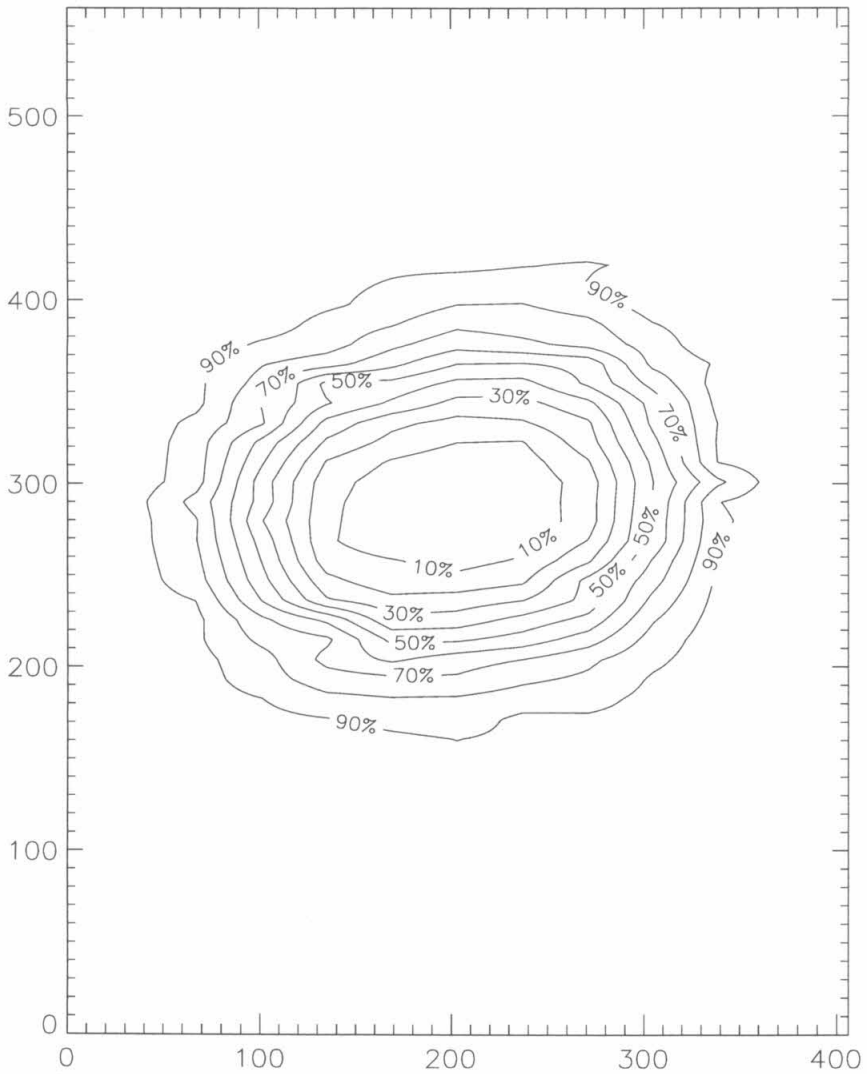

Figure 3.10 Contours of constant pitot pressure for the $u_{He}/u_{air} = 1.7$, no ramp case at $x/d = 32.8$. Axes are in hundredths of jet exit diameters. $p_{max} = 48900$ Pa, $p_{min} = 24600$ Pa

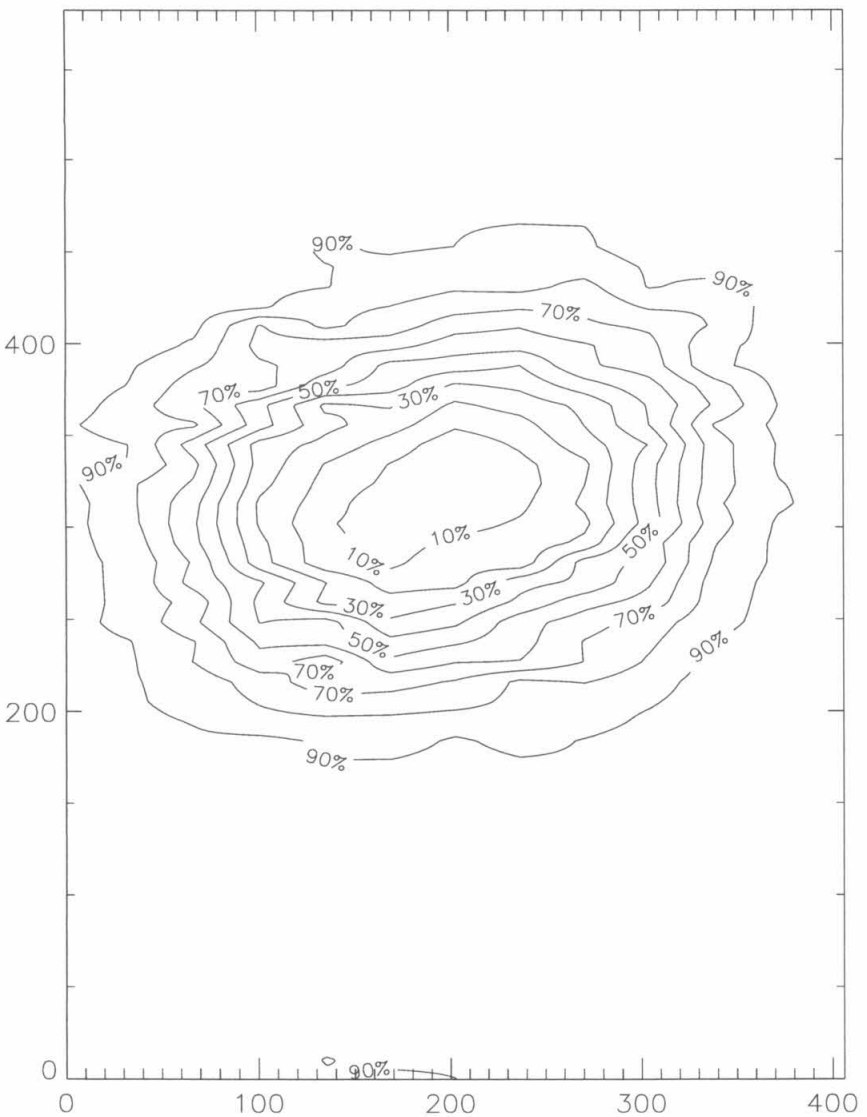

Figure 3.11 Contours of constant pitot pressure for the $u_{He}/u_{air} = 1.7$, no ramp case at $x/d = 49.2$. Axes are in hundredths of jet exit diameters. $p_{max} = 48900$ Pa, $p_{min} = 27800$ Pa

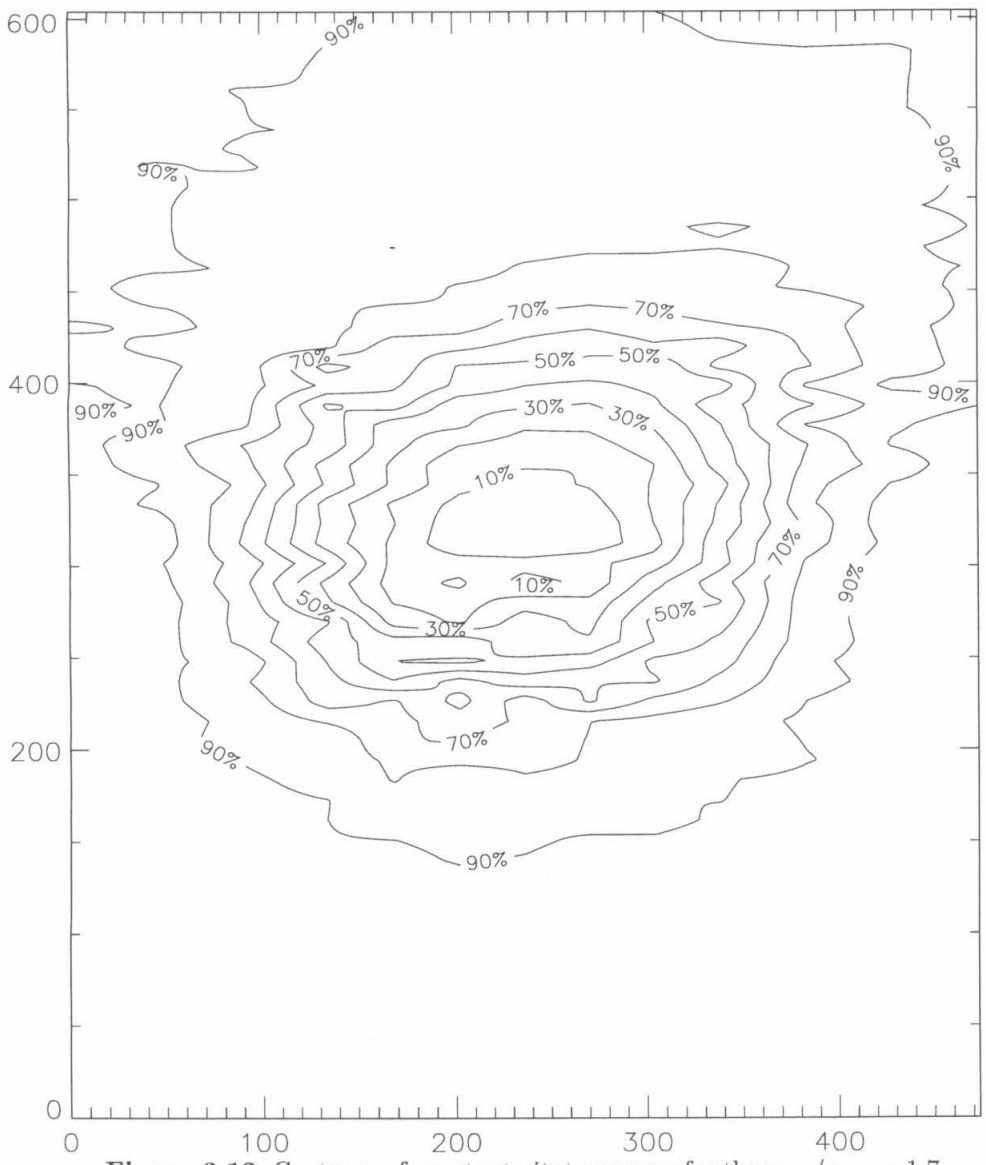

Figure 3.12 Contours of constant pitot pressure for the $u_{He}/u_{air} = 1.7$, no ramp case at $x/d = 66.4$. Axes are in hundredths of jet exit diameters. $p_{max} = 48900$ Pa, $p_{min} = 31400$ Pa

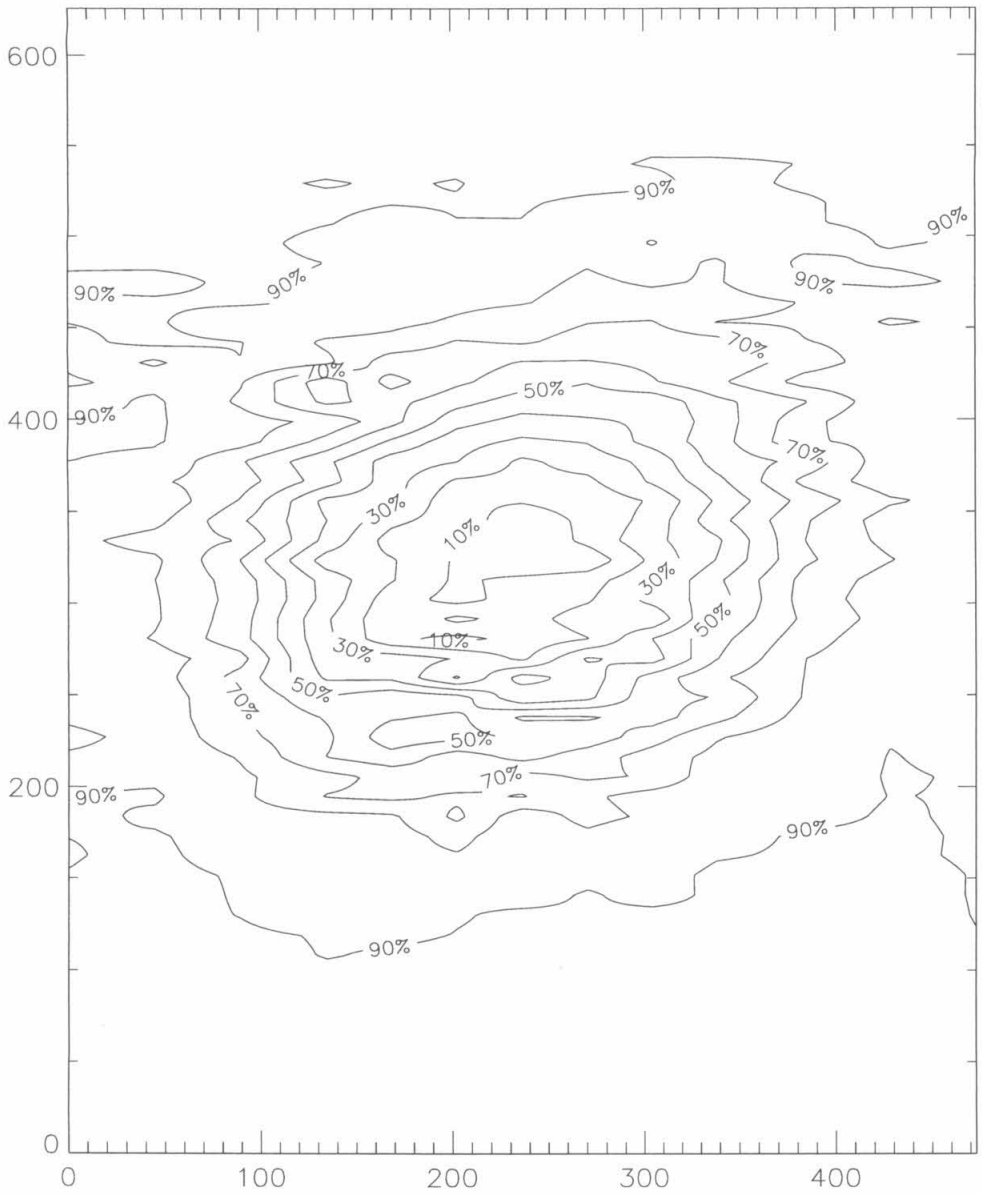

Figure 3.13 Contours of constant pitot pressure for the $u_{He}/u_{air} = 1.7$, no ramp case at $x/d = 83.6$. Axes are in hundredths of jet exit diameters. $p_{max} = 48700$ Pa, $p_{min} = 32900$ Pa

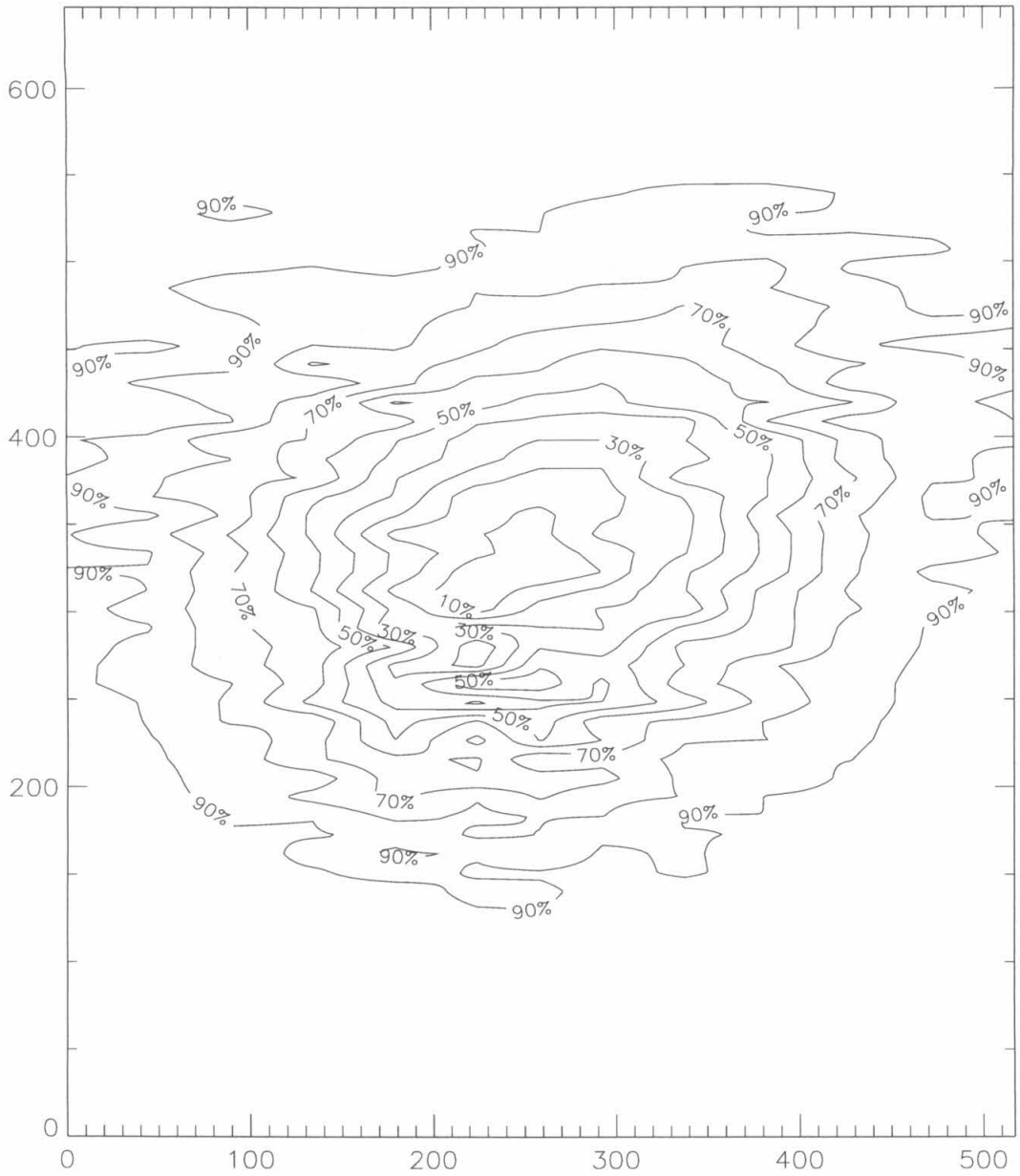

Figure 3.14 Contours of constant pitot pressure for the $u_{He}/u_{air} = 1.7$, no ramp case at $x/d = 99.9$. Axes are in hundredths of jet exit diameters. $p_{max} = 47900$ Pa, $p_{min} = 34600$ Pa

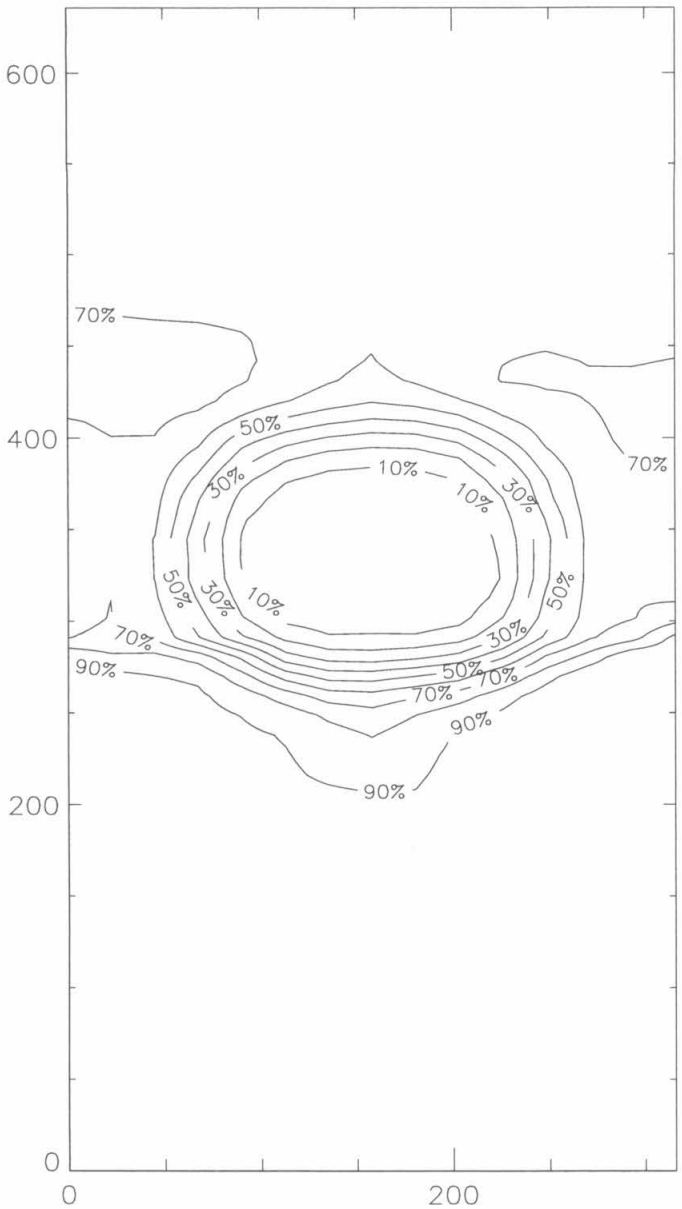

Figure 3.15 Contours of constant pitot pressure for the $u_{He}/u_{air} = 1.7$, 4.5° ramp case at $x/d = 16.4$. Axes are in hundredths of jet exit diameters. $p_{max} = 57000$ Pa, $p_{min} = 19700$ Pa

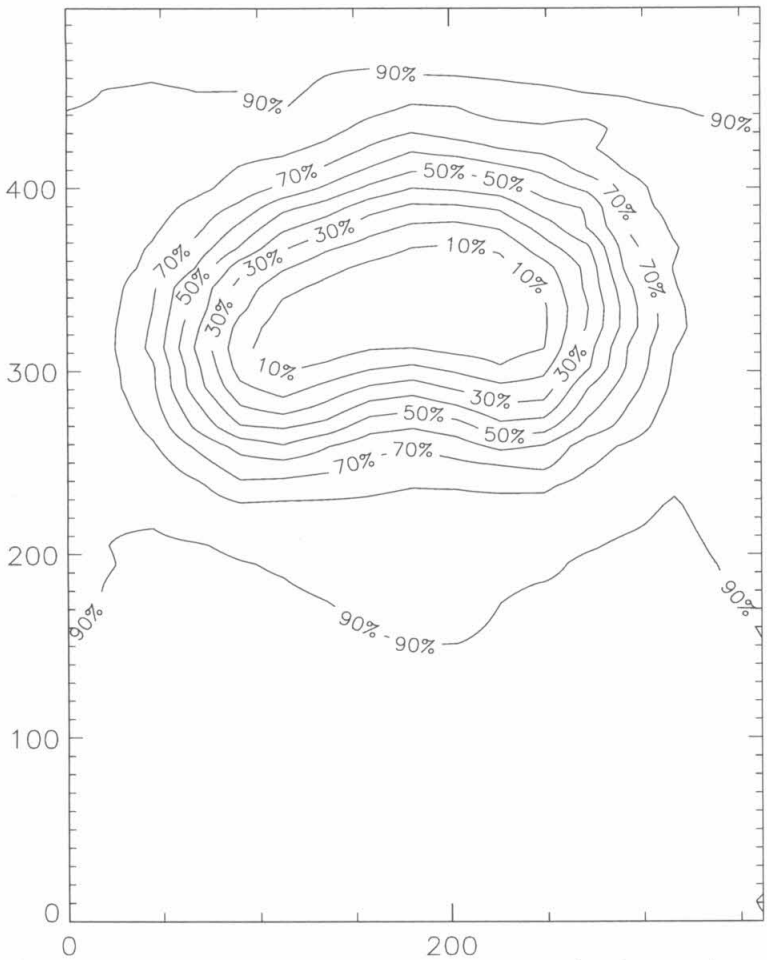

Figure 3.16 Contours of constant pitot pressure for the $u_{He}/u_{air} = 1.7$, 4.5° ramp case at $x/d = 32.8$. Axes are in hundredths of jet exit diameters. $p_{max} = 55900$ Pa, $p_{min} = 28200$ Pa

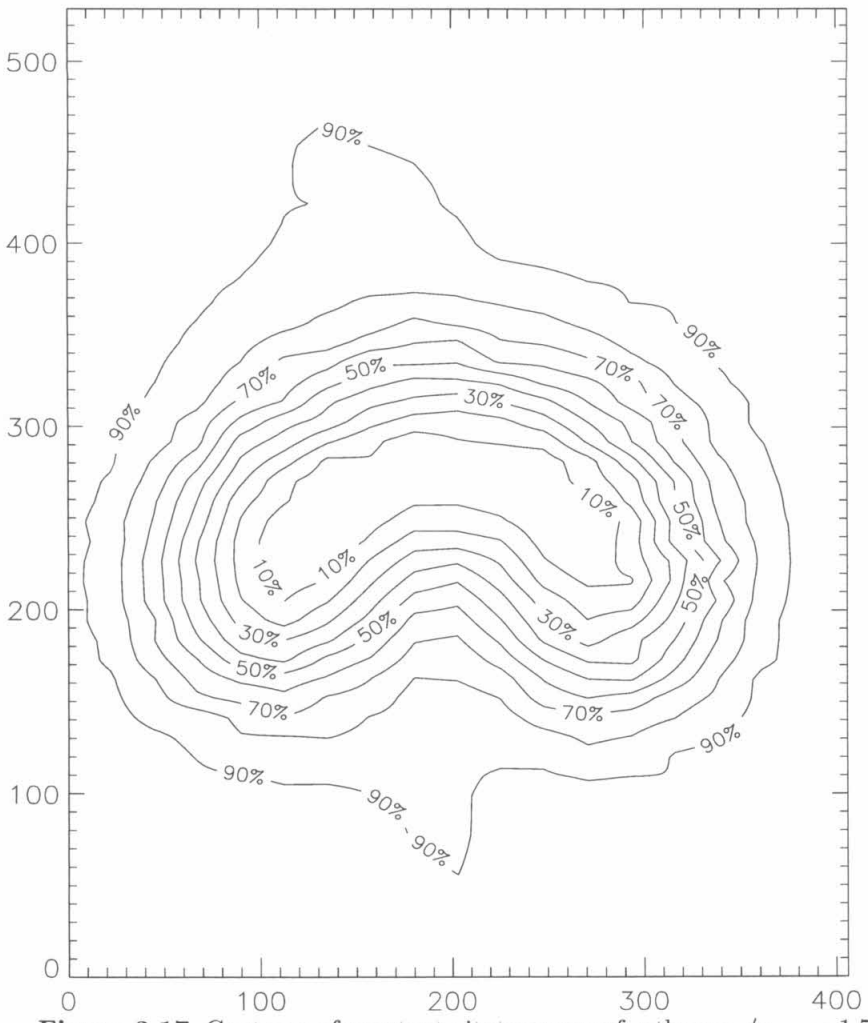

Figure 3.17 Contours of constant pitot pressure for the $u_{He}/u_{air} = 1.7$, 4.5° ramp case at $x/d = 49.2$. Axes are in hundredths of jet exit diameters. $p_{max} = 53500$ Pa, $p_{min} = 32900$ Pa

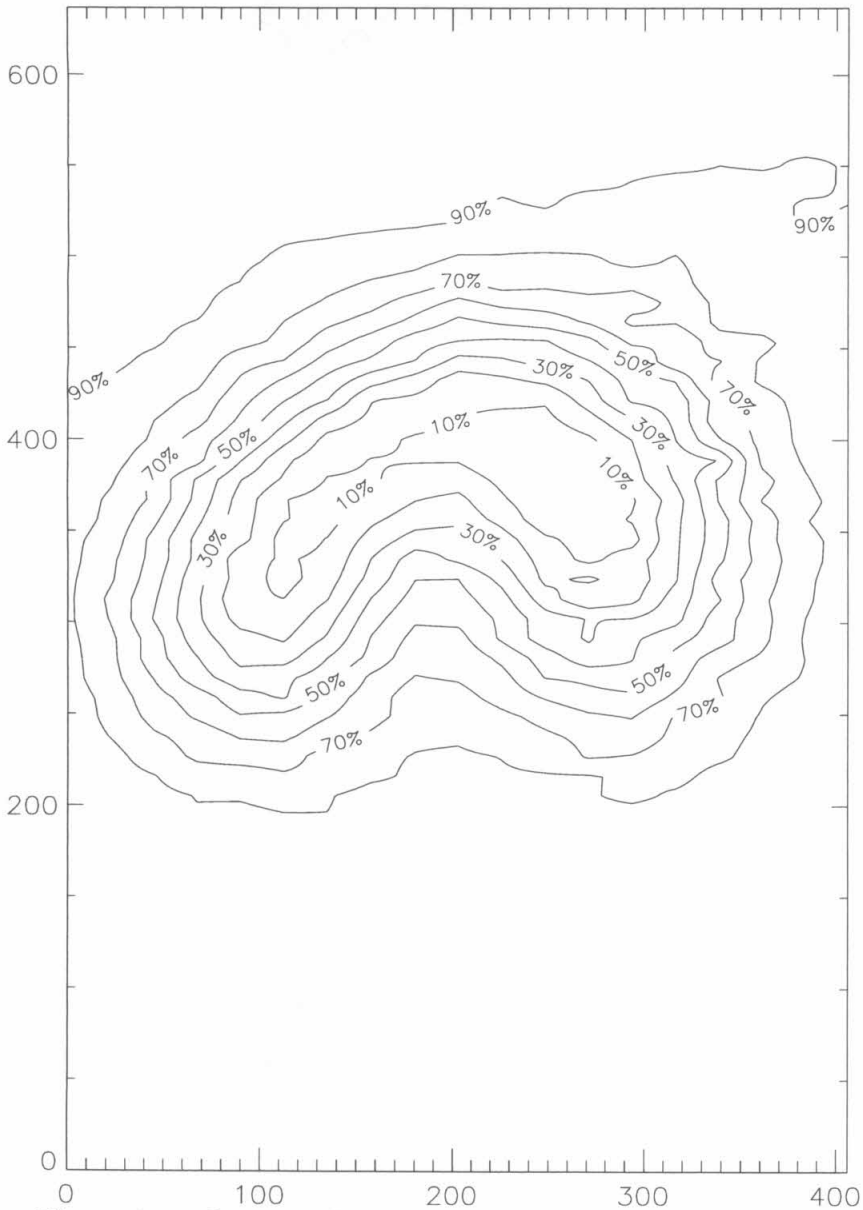

Figure 3.18 Contours of constant pitot pressure for the $u_{He}/u_{air} = 1.7$, 4.5° ramp case at $x/d = 66.4$. Axes are in hundredths of jet exit diameters. $p_{max} = 54600$ Pa, $p_{min} = 38400$ Pa

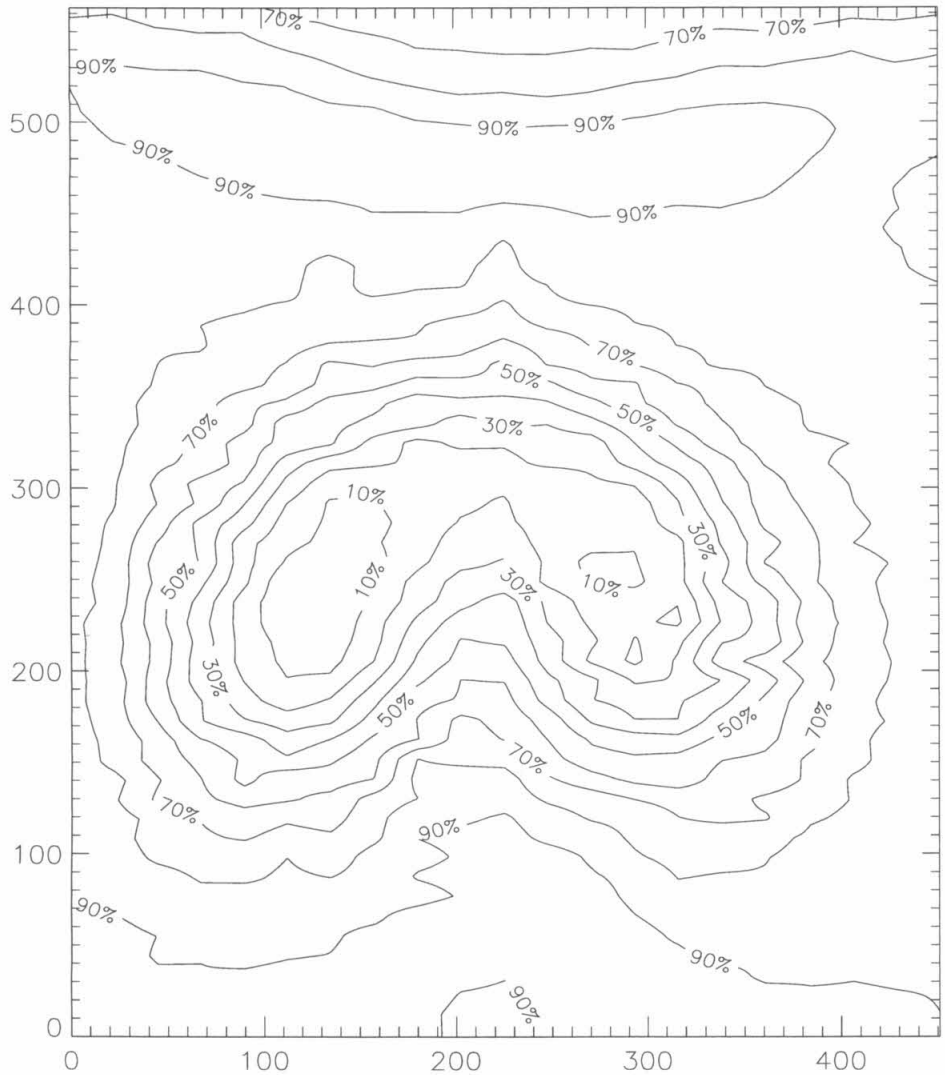

Figure 3.19 Contours of constant pitot pressure for the $u_{He}/u_{air} = 1.7$, 4.5° ramp case at $x/d = 83.6$. Axes are in hundredths of jet exit diameters. $p_{max} = 55800$ Pa, $p_{min} = 41600$ Pa

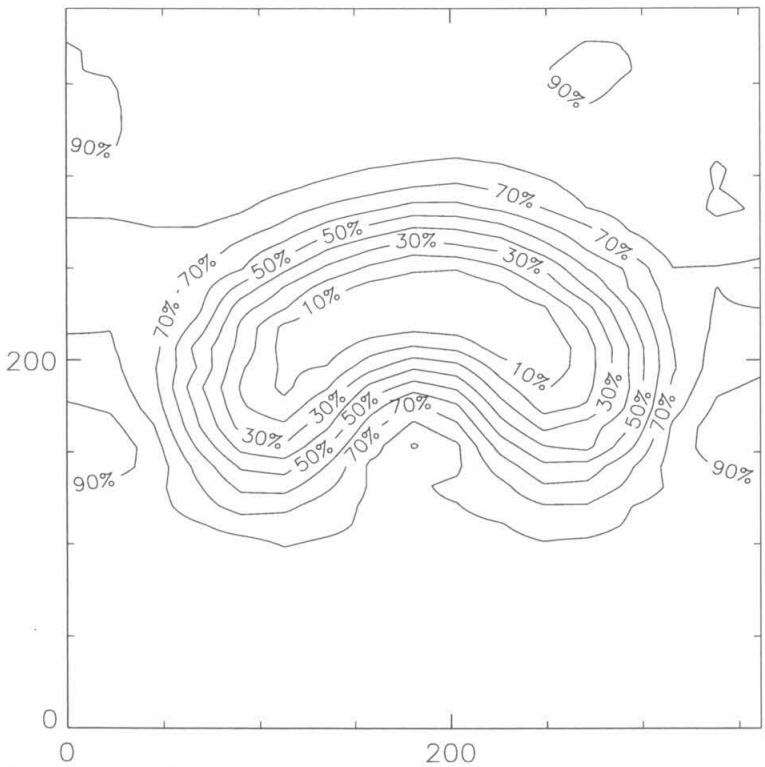

Figure 3.20 Contours of constant pitot pressure for the $u_{He}/u_{air} = 1.32$, 7.0° ramp case at $x/d = 32.8$. Axes are in hundredths of jet exit diameters. $p_{max} = 60300$ Pa, $p_{min} = 34700$ Pa

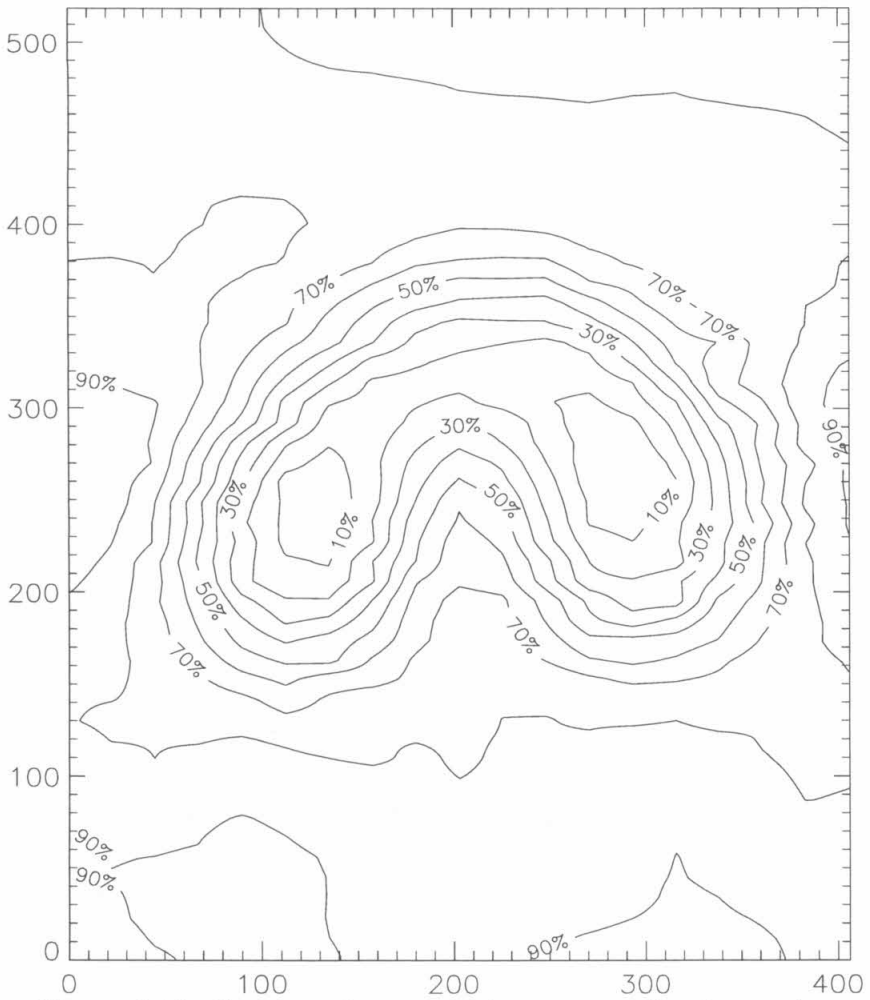

Figure 3.21 Contours of constant pitot pressure for the $u_{He}/u_{air} = 1.32$, 7.0° ramp case at $x/d = 49.2$. Axes are in hundredths of jet exit diameters. $p_{max} = 59100$ Pa, $p_{min} = 44300$ Pa

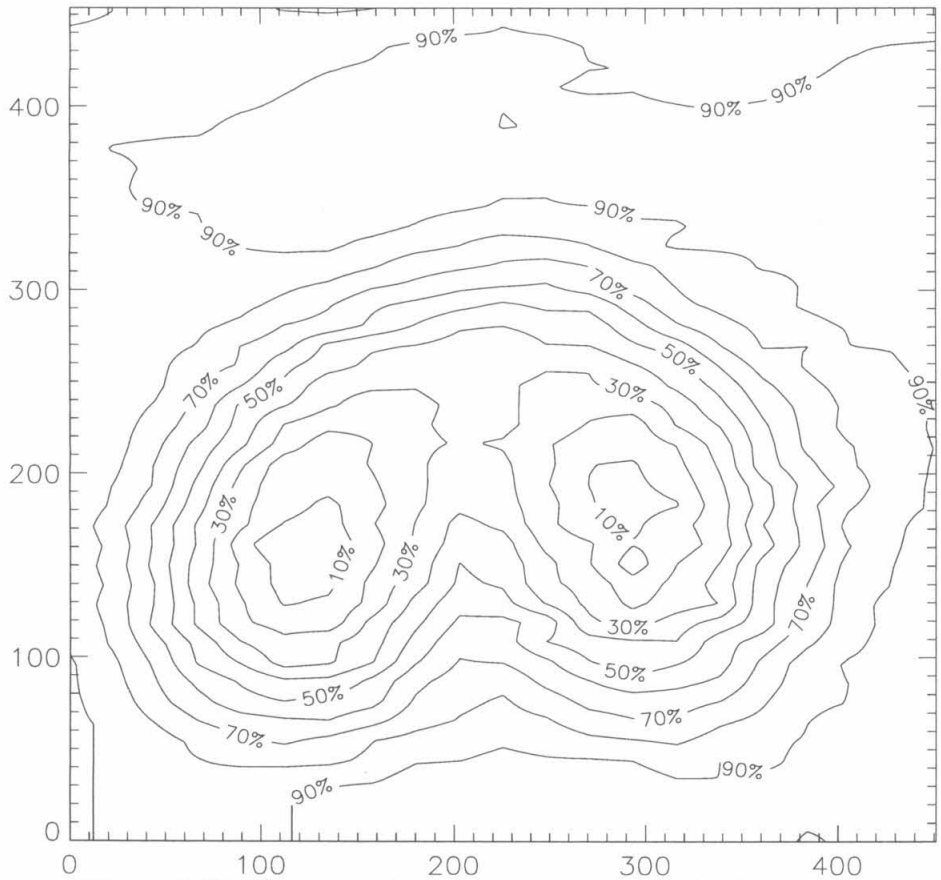

Figure 3.22 Contours of constant pitot pressure for the $u_{He}/u_{air} = 1.32$, 7.0° ramp case at $x/d = 66.4$. Axes are in hundredths of jet exit diameters. $p_{max} = 59700$ Pa, $p_{min} = 48400$ Pa

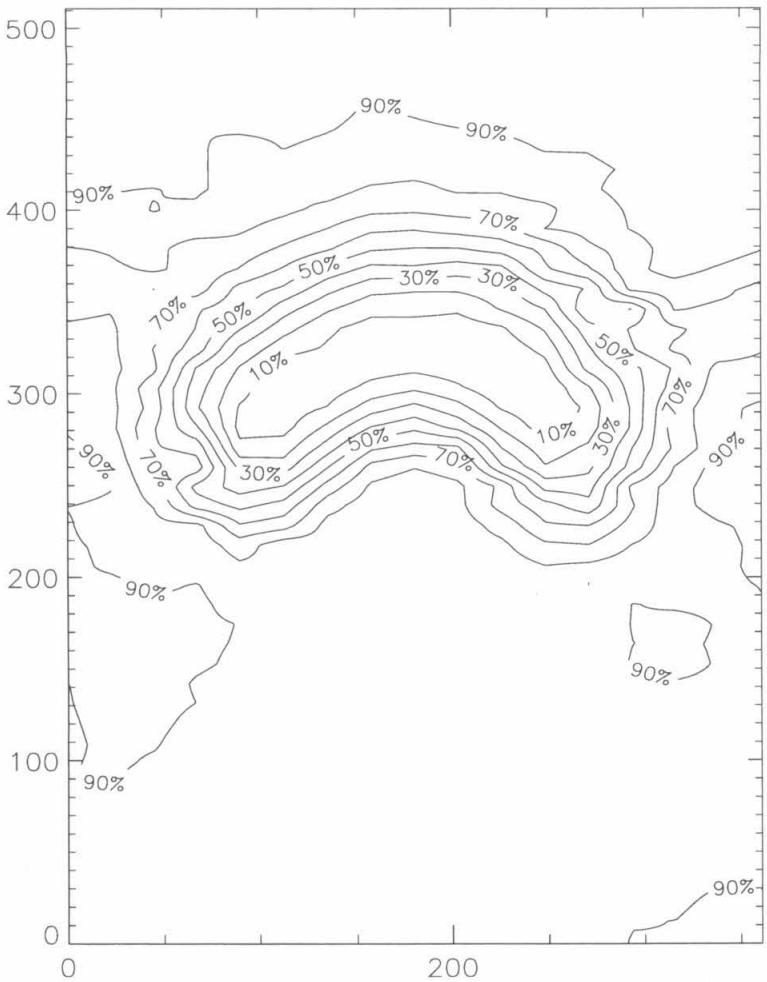

Figure 3.23 Contours of constant pitot pressure for the $u_{He}/u_{air} = 1.7$, 7.0° ramp case at $x/d = 32.8$. Axes are in hundredths of jet exit diameters. $p_{max} = 59900$ Pa, $p_{min} = 31400$ Pa

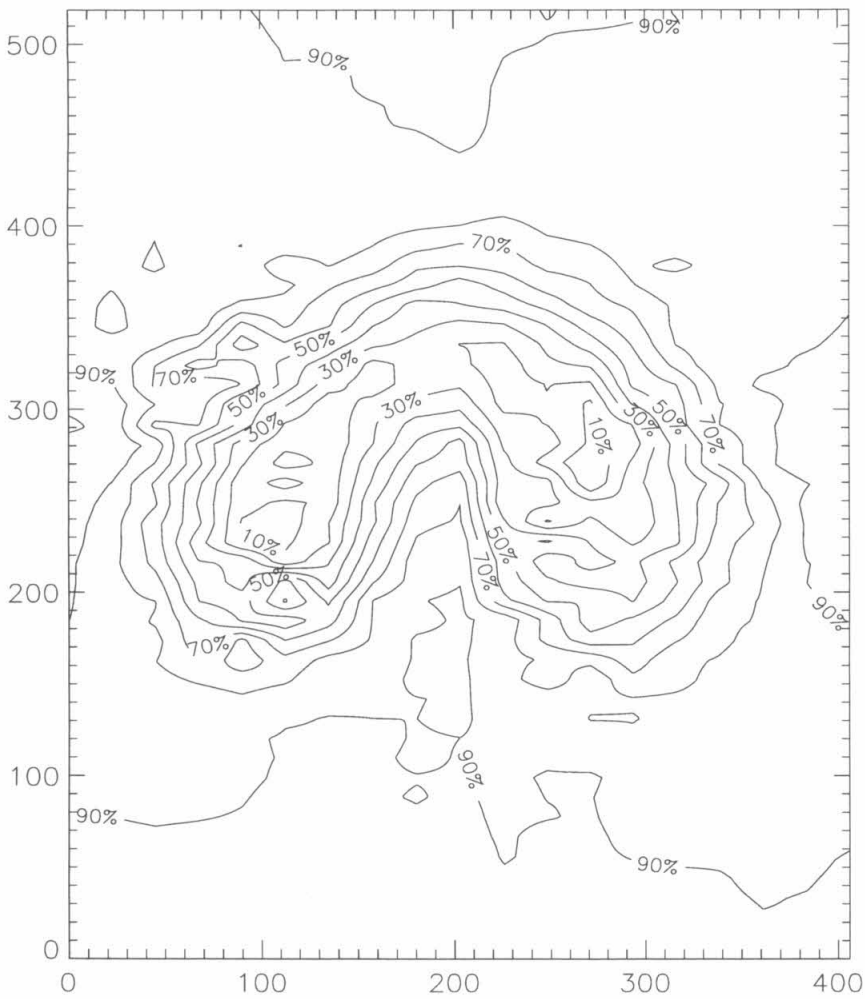

Figure 3.24 Contours of constant pitot pressure for the $u_{He}/u_{air} = 1.7$, 7.0° ramp case at $x/d = 49.2$. Axes are in hundredths of jet exit diameters. $p_{max} = 58300$ Pa, $p_{min} = 39600$ Pa

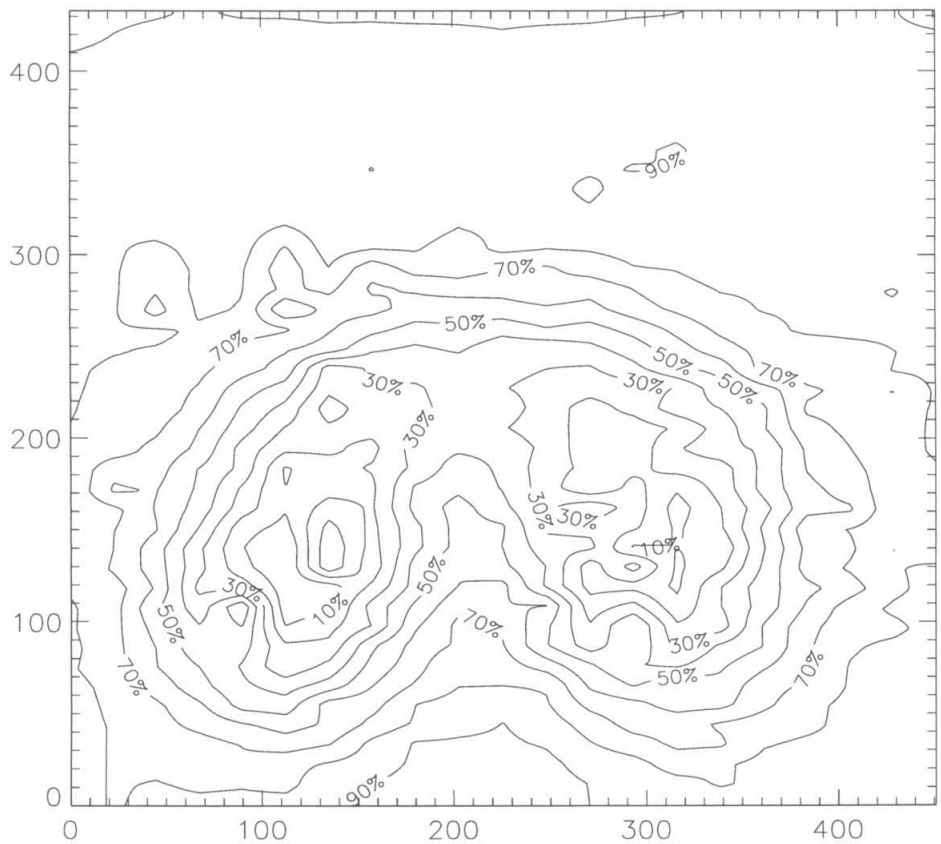

Figure 3.25 Contours of constant pitot pressure for the $u_{He}/u_{air} = 1.7$, 7.0° ramp case at $x/d = 66.4$. Axes are in hundredths of jet exit diameters. $p_{max} = 61300$ Pa, $p_{min} = 44600$ Pa

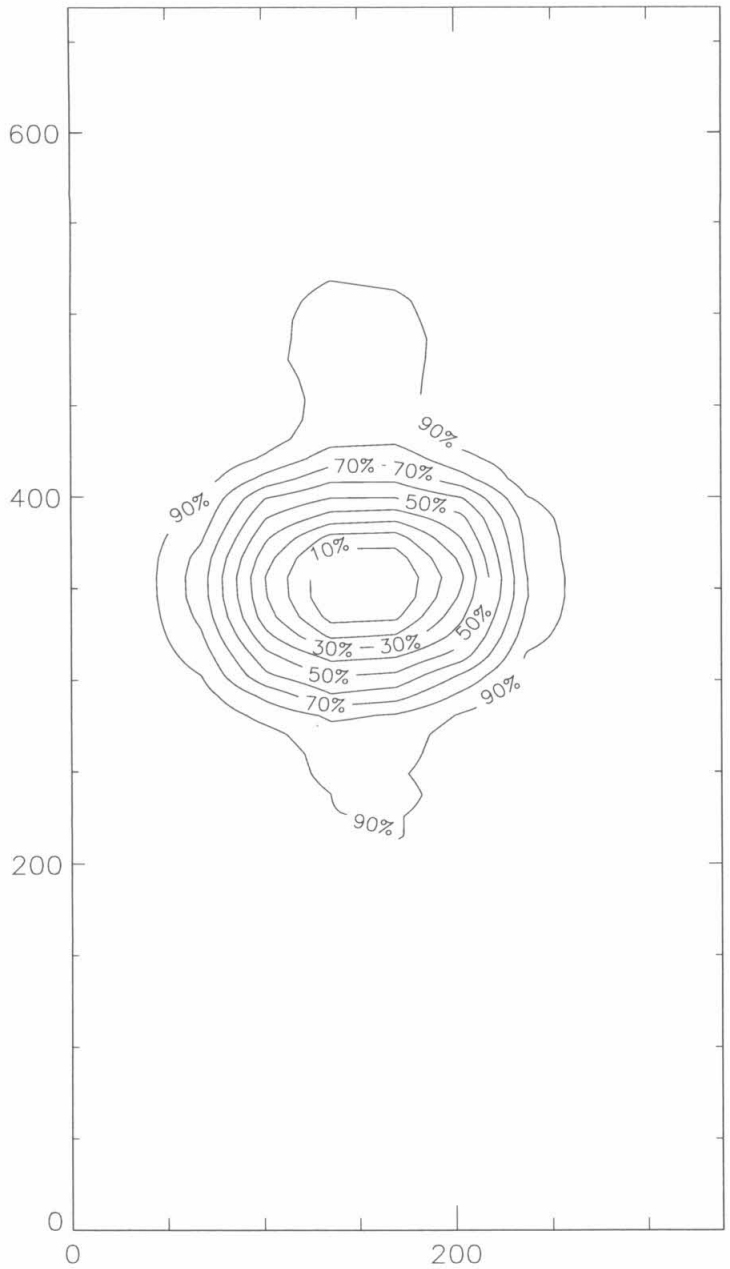

Figure 3.26 Contours of constant probe recovery temperature for the $u_{He}/u_{air} = 1.32$, no ramp case at $x/d = 16.4$. Axes are in hundredths of jet exit diameters. $T_{max} = 296$ K, $T_{min} = 213$ K

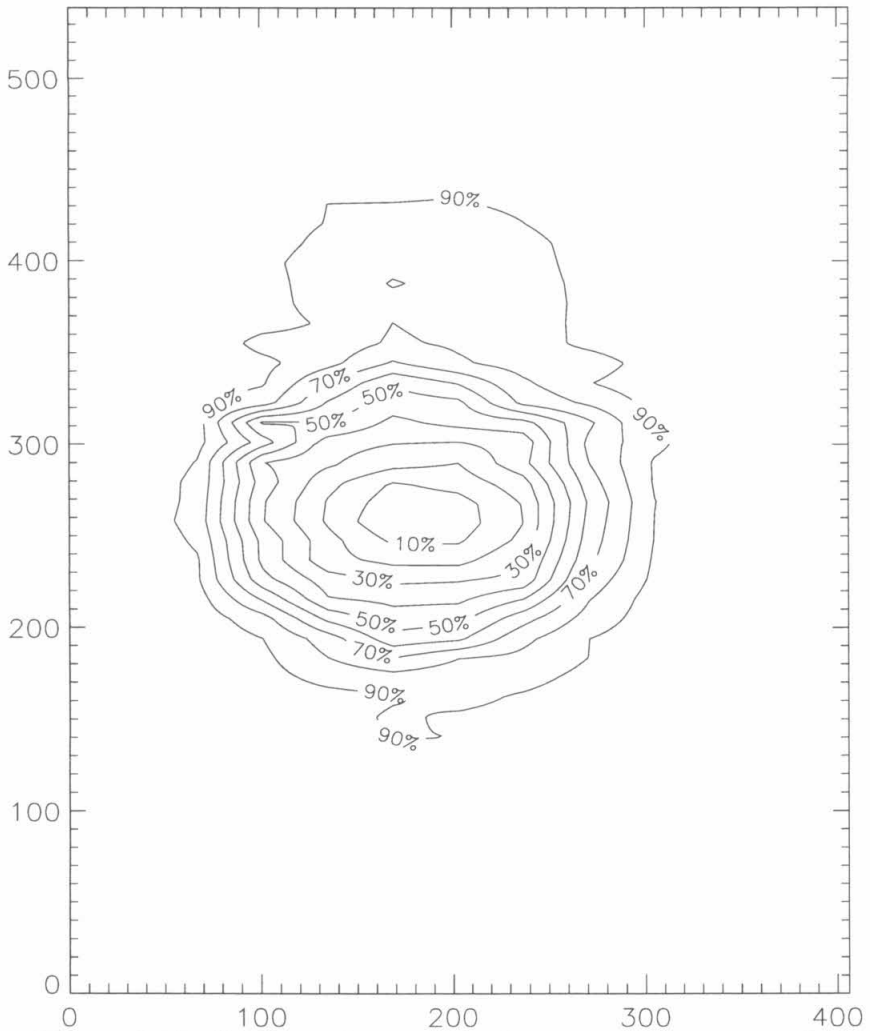

Figure 3.27 Contours of constant probe recovery temperature for the $u_{He}/u_{air} = 1.32$, no ramp case at $x/d = 32.8$. Axes are in hundredths of jet exit diameters. $T_{max} = 294$ K, $T_{min} = 242$ K

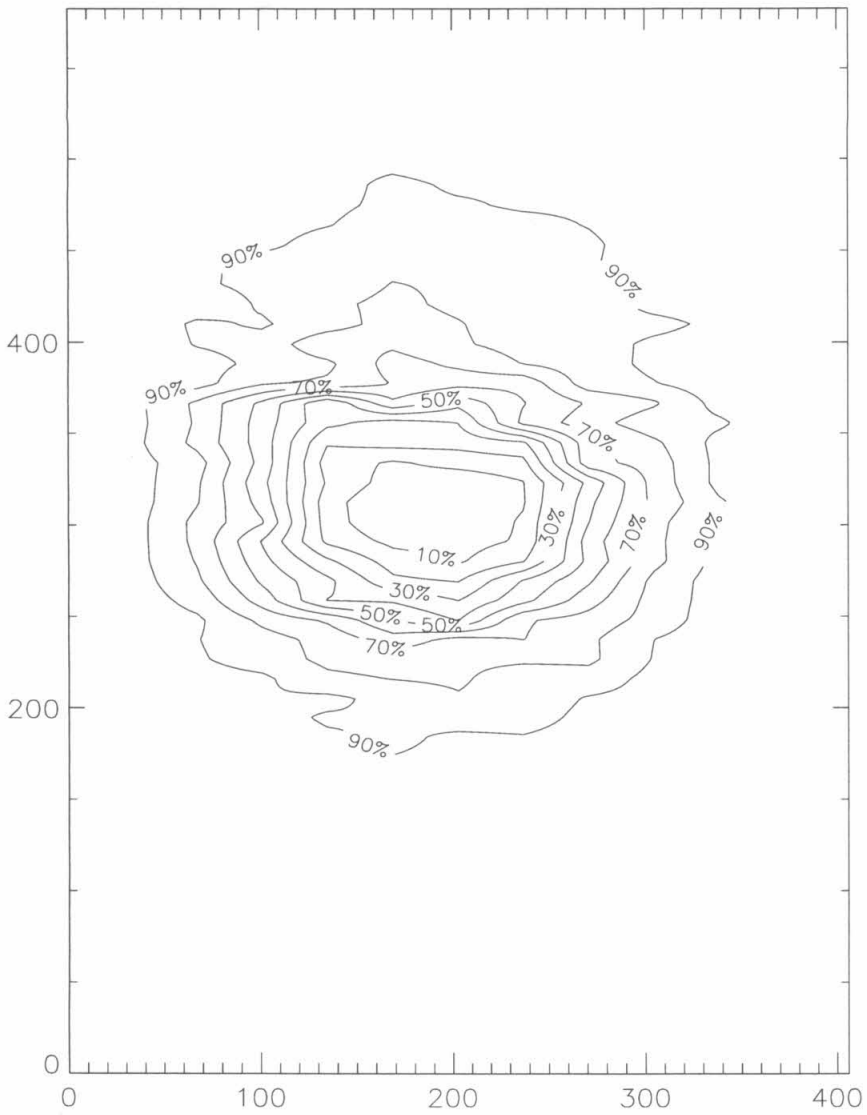

Figure 3.28 Contours of constant probe recovery temperature for the $u_{He}/u_{air} = 1.32$, no ramp case at $x/d = 49.2$. Axes are in hundredths of jet exit diameters. $T_{max} = 293$ K, $T_{min} = 251$ K

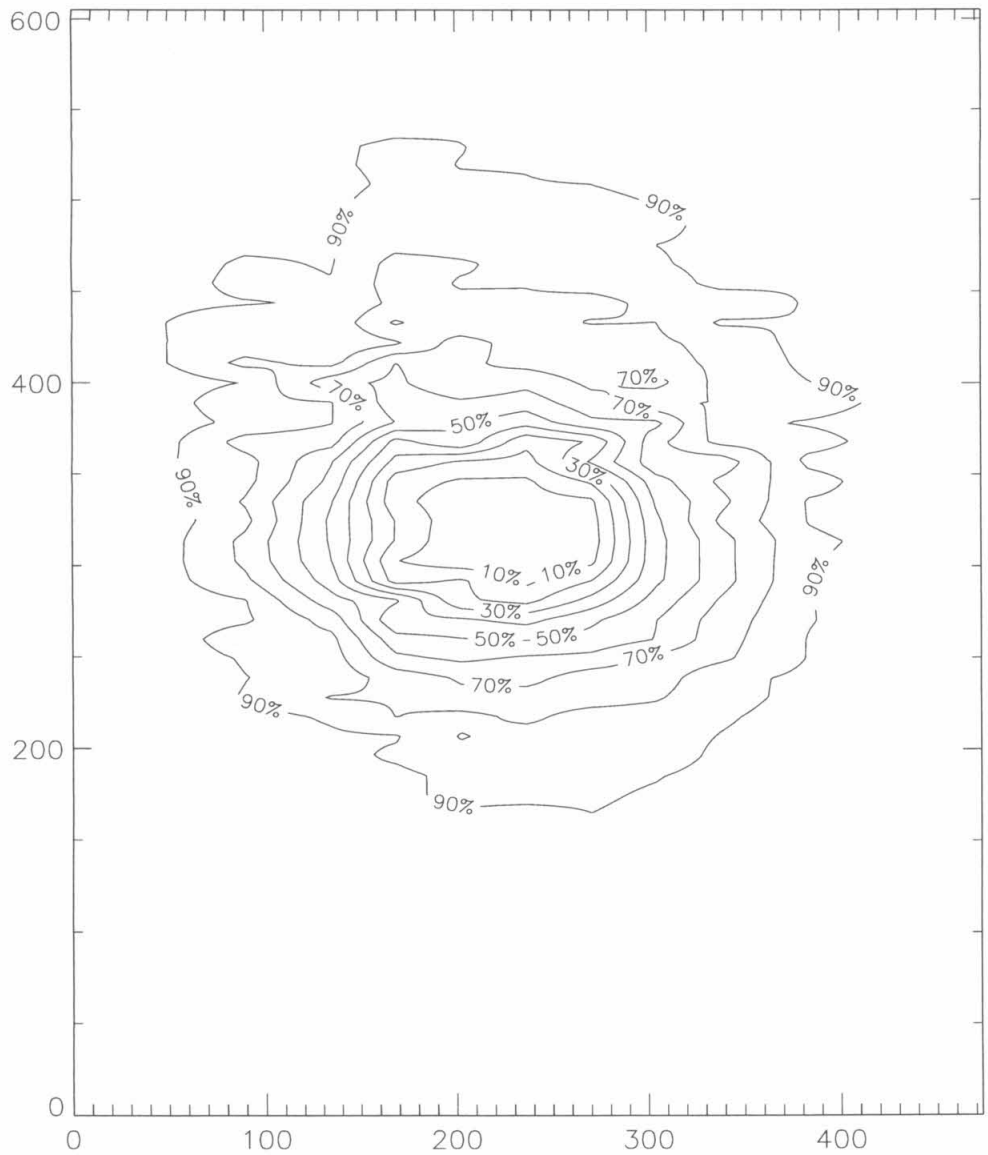

Figure 3.29 Contours of constant probe recovery temperature for the $u_{He}/u_{air} = 1.32$, no ramp case at $x/d = 66.4$. Axes are in hundredths of jet exit diameters. $T_{max} = 292$ K, $T_{min} = 257$ K

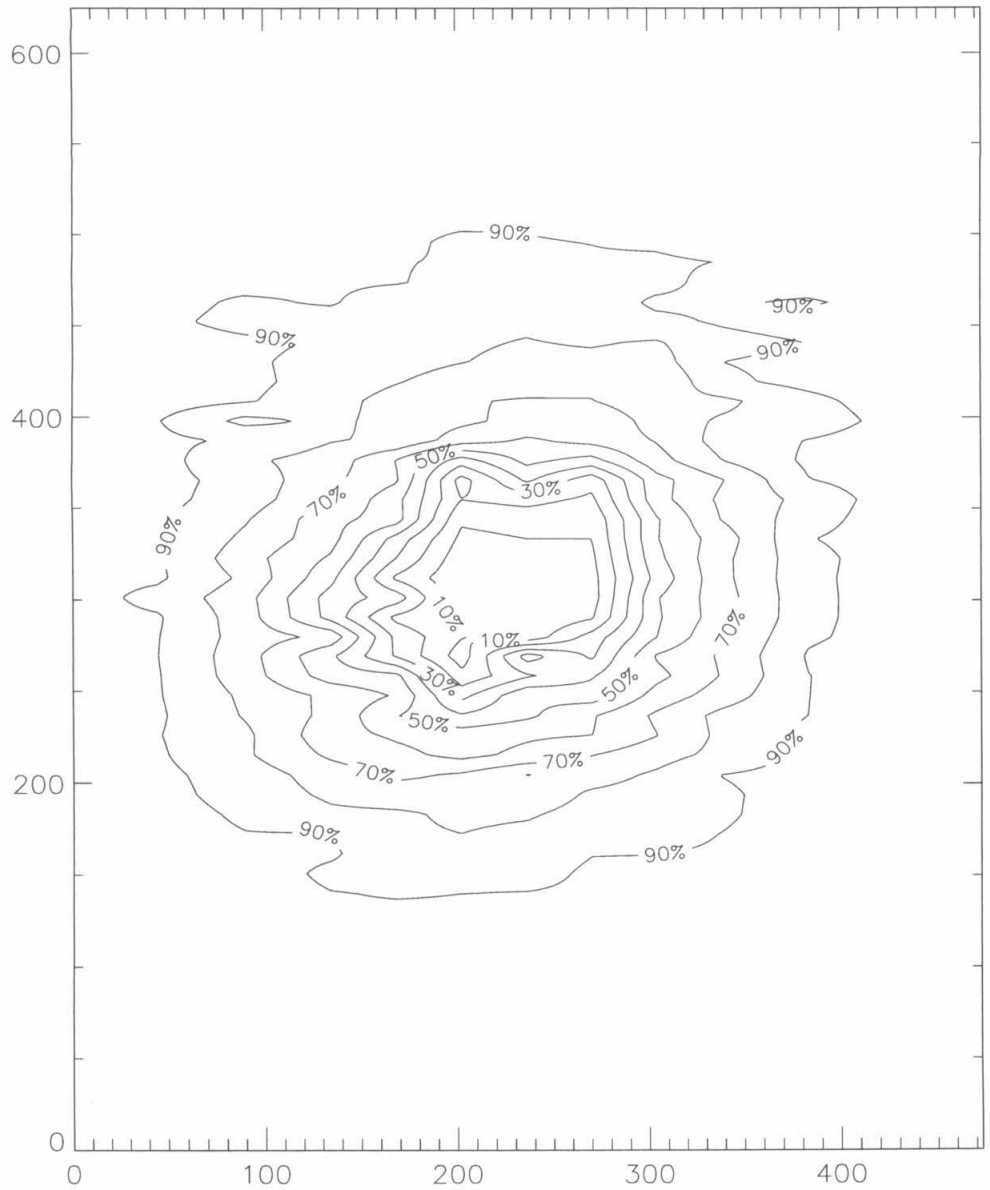

Figure 3.30 Contours of constant probe recovery temperature for the $u_{He}/u_{air} = 1.32$, no ramp case at $x/d = 83.6$. Axes are in hundredths of jet exit diameters. $T_{max} = 292$ K, $T_{min} = 261$ K

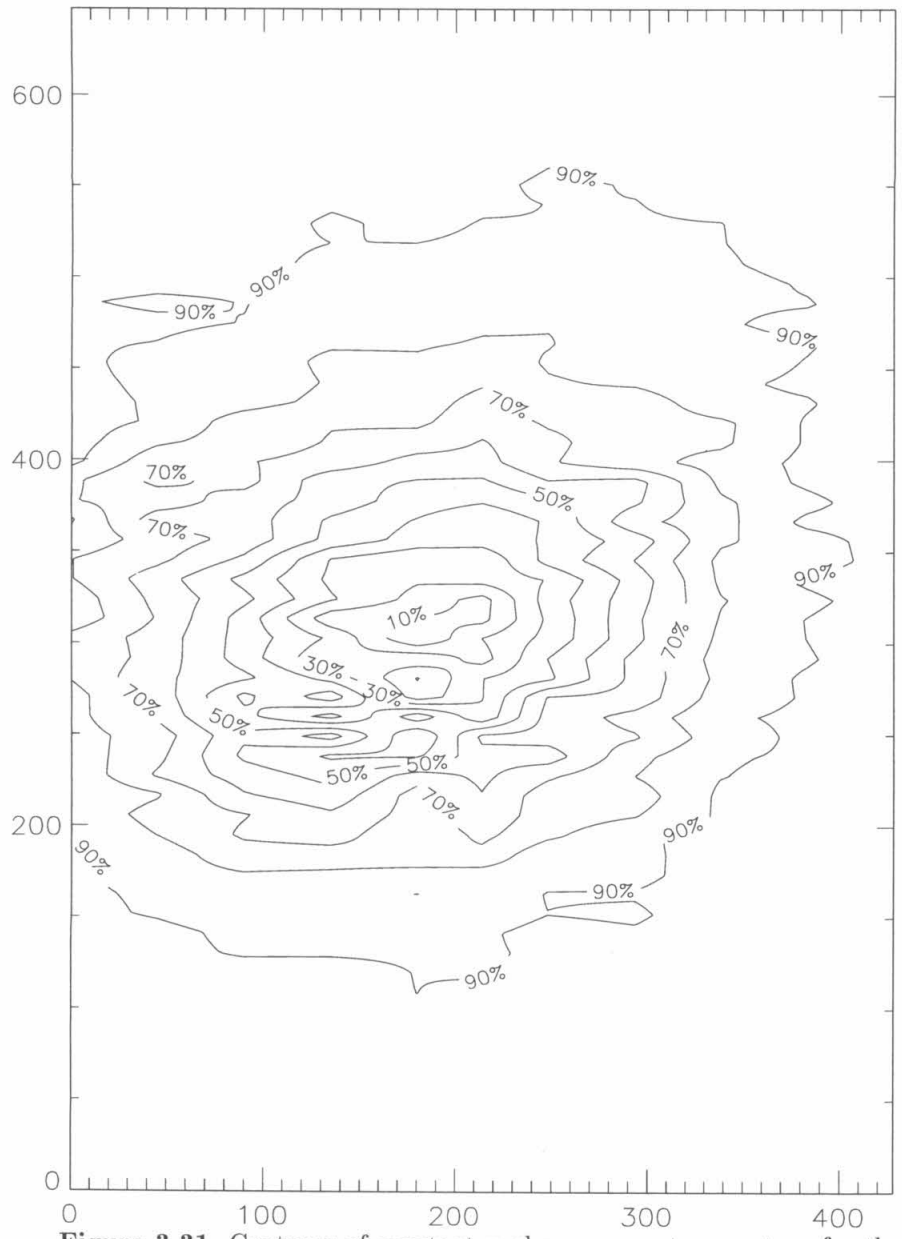

Figure 3.31 Contours of constant probe recovery temperature for the $u_{He}/u_{air} = 1.32$, no ramp case at $x/d = 99.9$. Axes are in hundredths of jet exit diameters. $T_{max} = 290$ K, $T_{min} = 269$ K

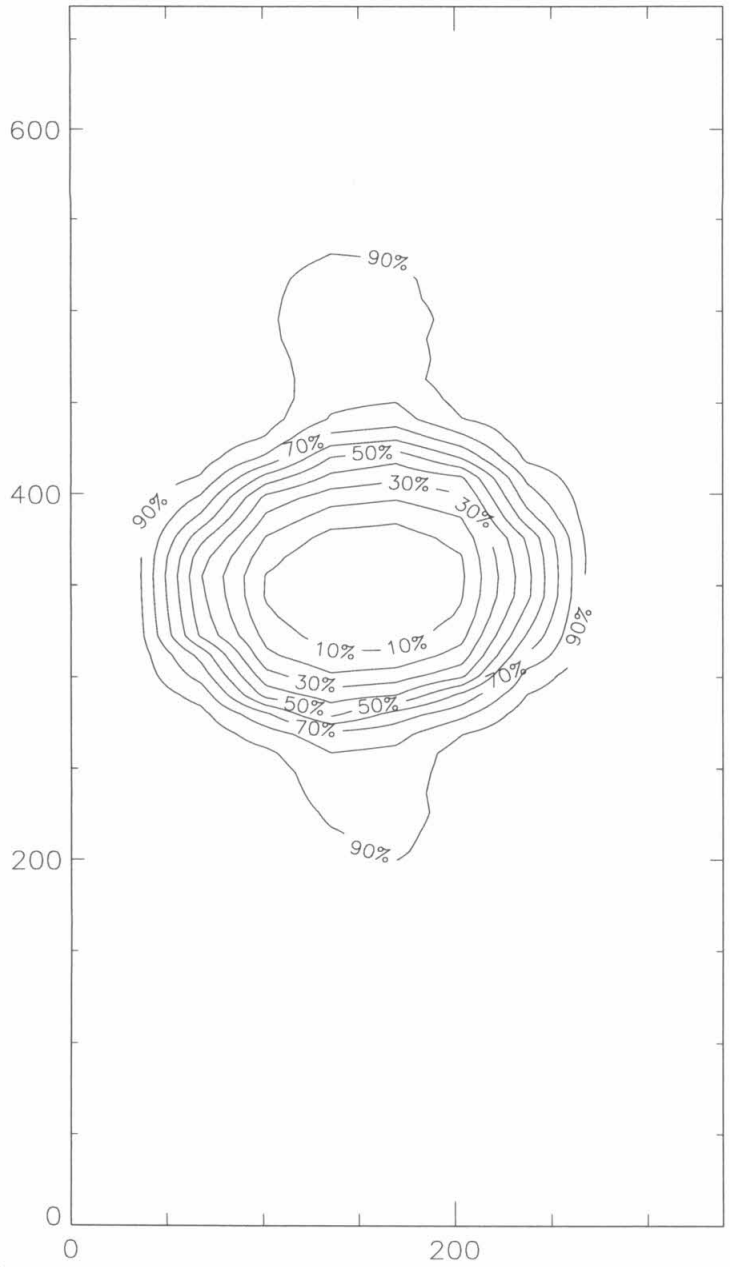

Figure 3.32 Contours of constant probe recovery temperature for the $u_{He}/u_{air} = 1.7$, no ramp case at $x/d = 16.4$. Axes are in hundredths of jet exit diameters. $T_{max} = 296$ K, $T_{min} = 236$ K

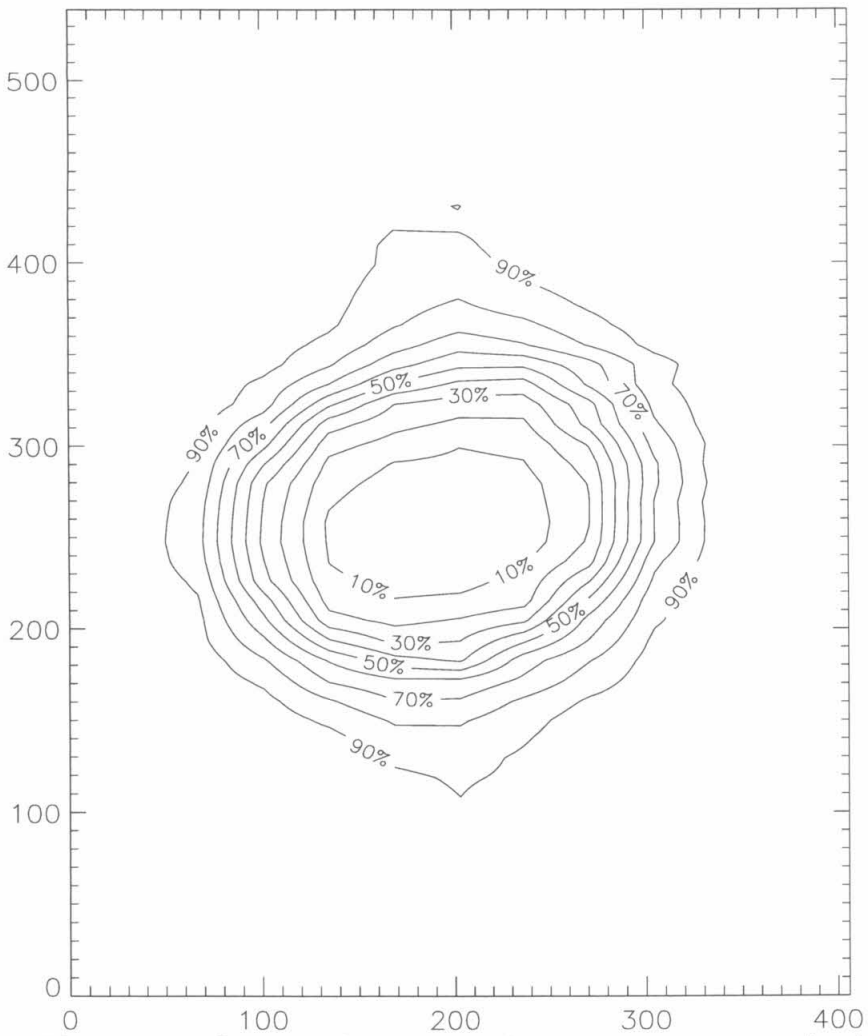

Figure 3.33 Contours of constant probe recovery temperature for the $u_{He}/u_{air} = 1.7$, no ramp case at $x/d = 32.8$. Axes are in hundredths of jet exit diameters. $T_{max} = 296$ K, $T_{min} = 250$ K

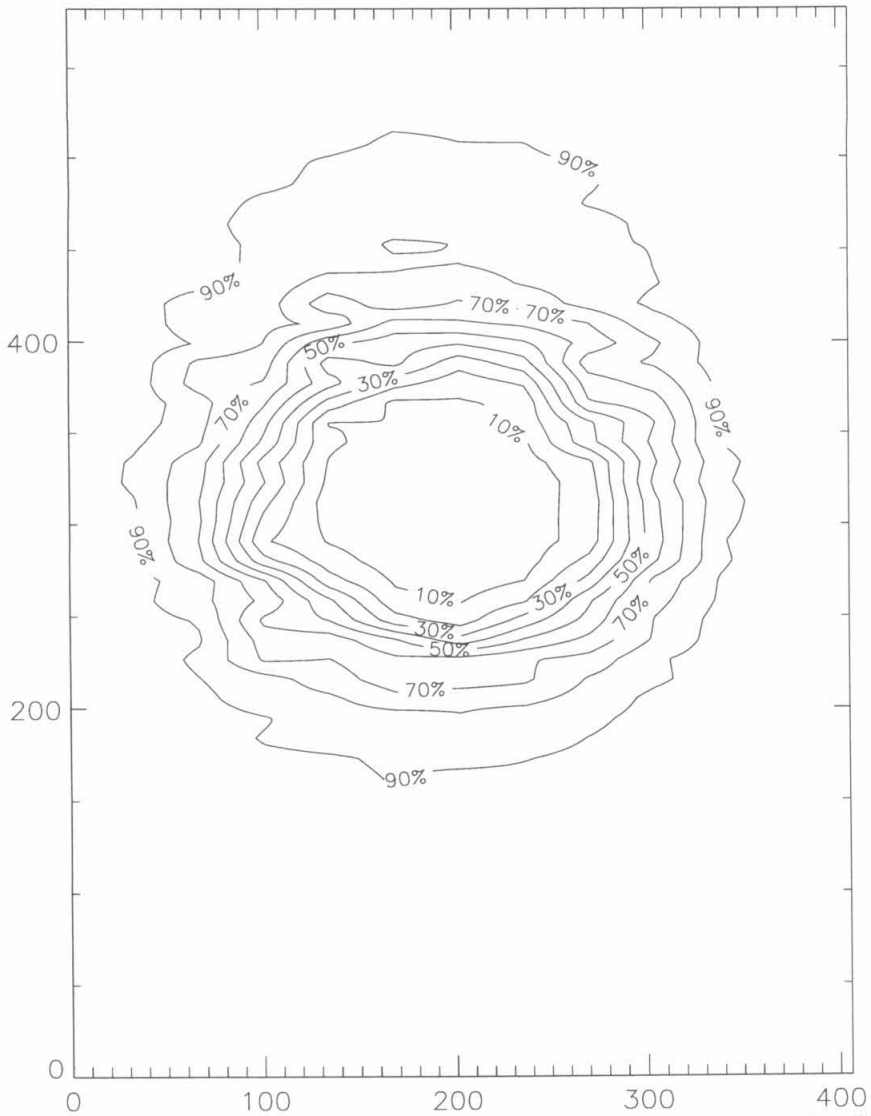

Figure 3.34 Contours of constant probe recovery temperature for the $u_{He}/u_{air} = 1.7$, no ramp case at $x/d = 49.2$. Axes are in hundredths of jet exit diameters. $T_{max} = 294$ K, $T_{min} = 258$ K

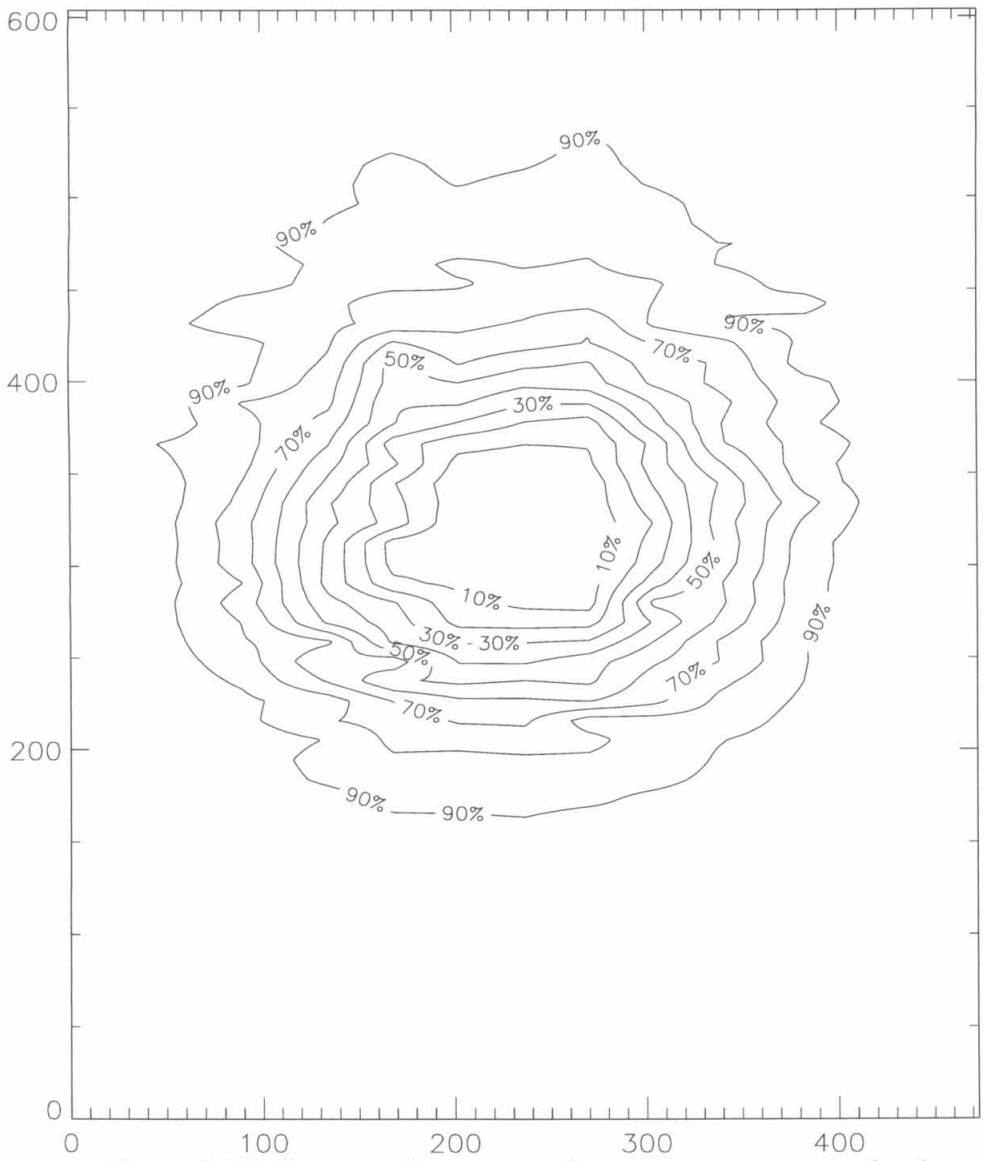

Figure 3.35 Contours of constant probe recovery temperature for the $u_{He}/u_{air} = 1.7$, no ramp case at $x/d = 66.4$. Axes are in hundredths of jet exit diameters. $T_{max} = 292$ K, $T_{min} = 260$ K

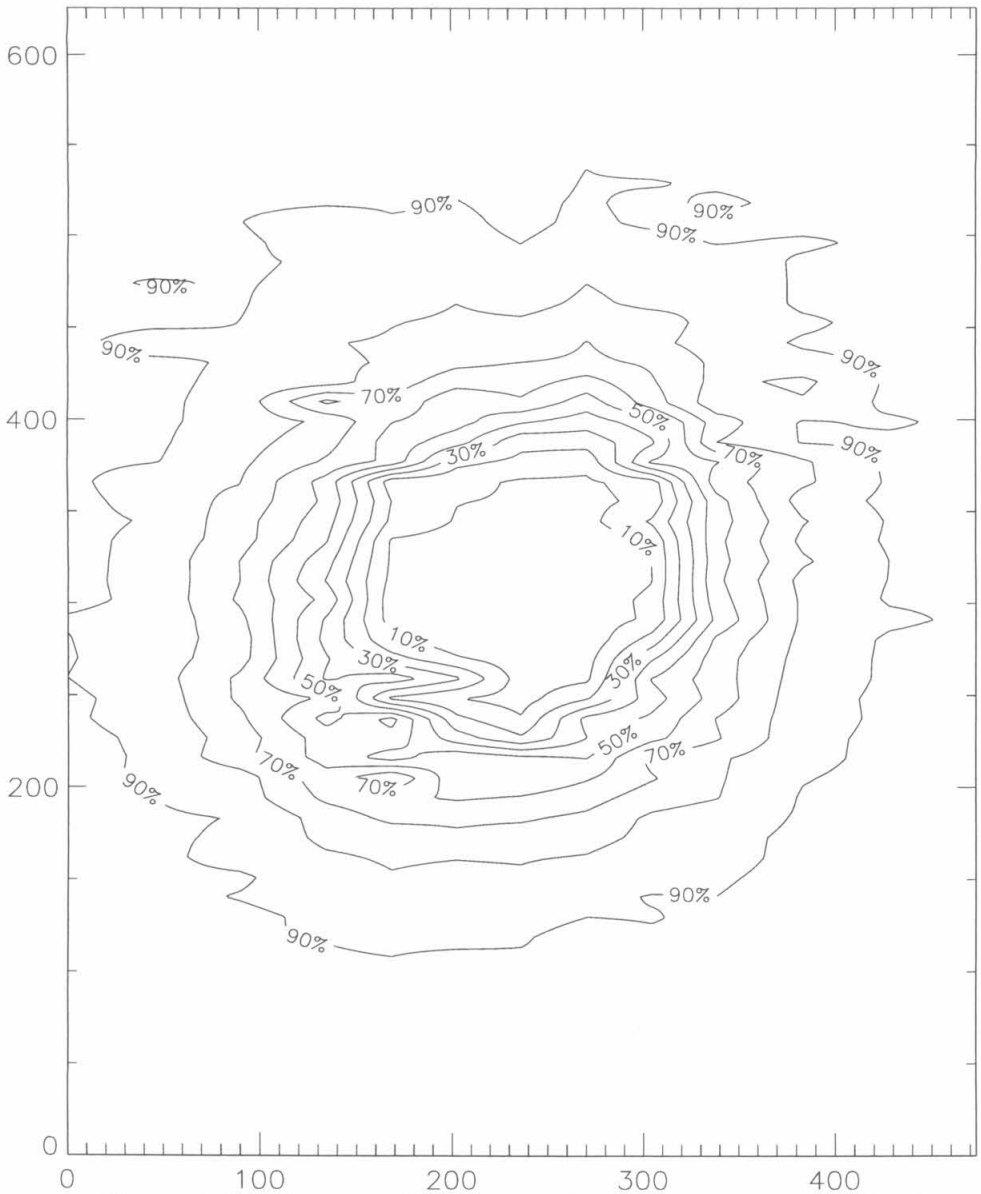

Figure 3.36 Contours of constant probe recovery temperature for the $u_{He}/u_{air} = 1.7$, no ramp case at $x/d = 83.6$. Axes are in hundredths of jet exit diameters. $T_{max} = 293$ K, $T_{min} = 261$ K

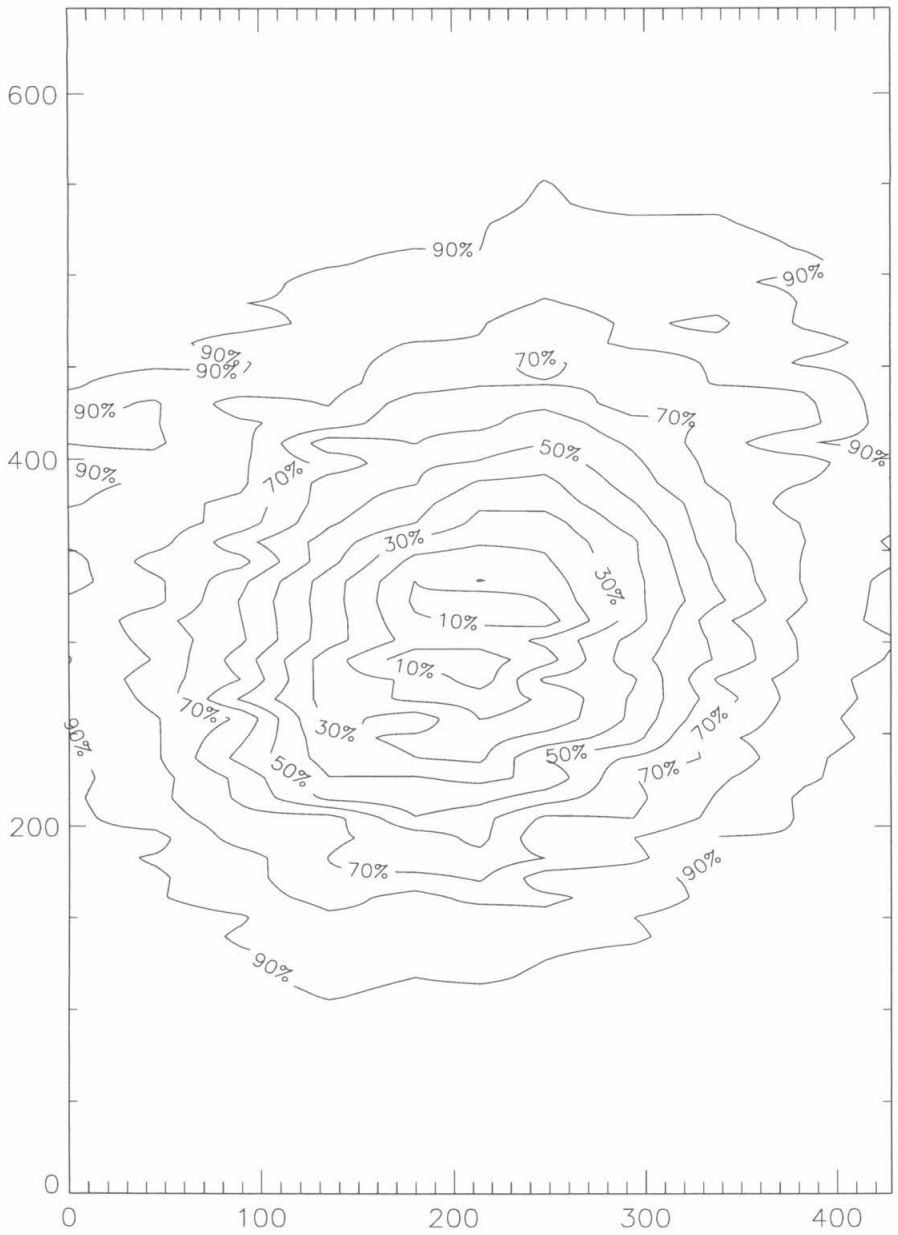

Figure 3.37 Contours of constant probe recovery temperature for the $u_{He}/u_{air} = 1.7$, no ramp case at $x/d = 99.9$. Axes are in hundredths of jet exit diameters. $T_{max} = 290$ K, $T_{min} = 267$ K

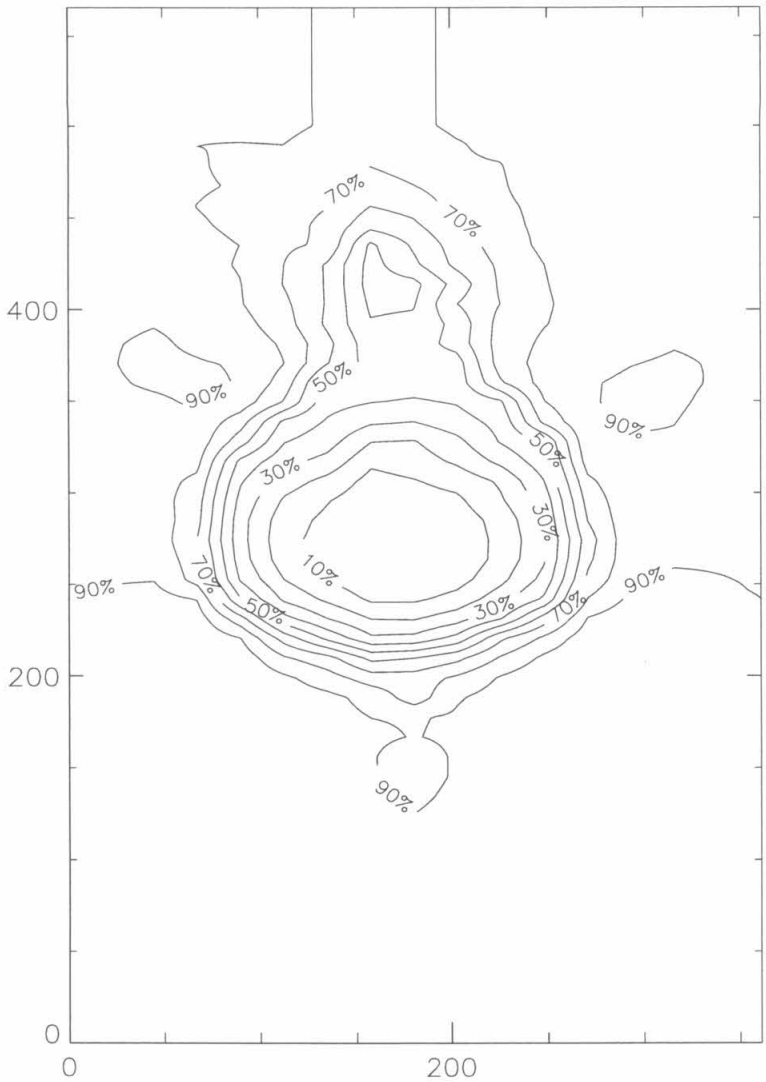

Figure 3.38 Contours of constant probe recovery temperature for the $u_{He}/u_{air} = 1.7$, 4.5° ramp case at $x/d = 16.4$. Axes are in hundredths of jet exit diameters. $T_{max} = 301$ K, $T_{min} = 240$ K

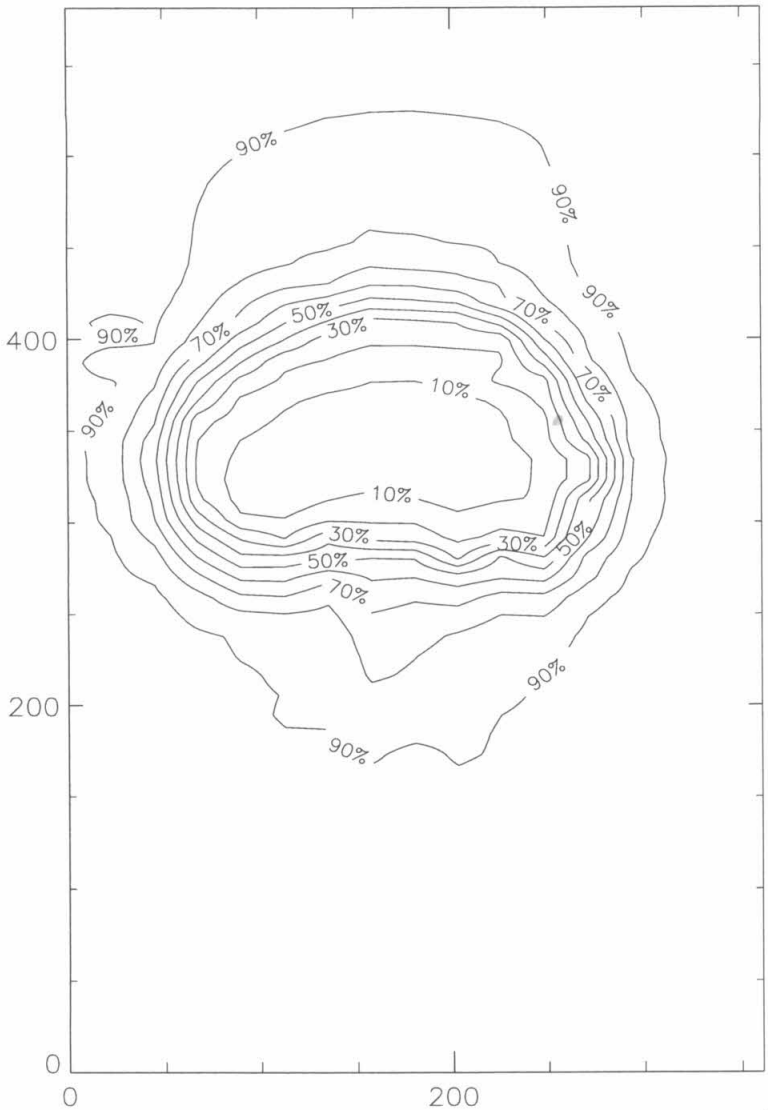

Figure 3.39 Contours of constant probe recovery temperature for the $u_{He}/u_{air} = 1.7$, 4.5° ramp case at $x/d = 32.8$. Axes are in hundredths of jet exit diameters. $T_{max} = 302$ K, $T_{min} = 256$ K

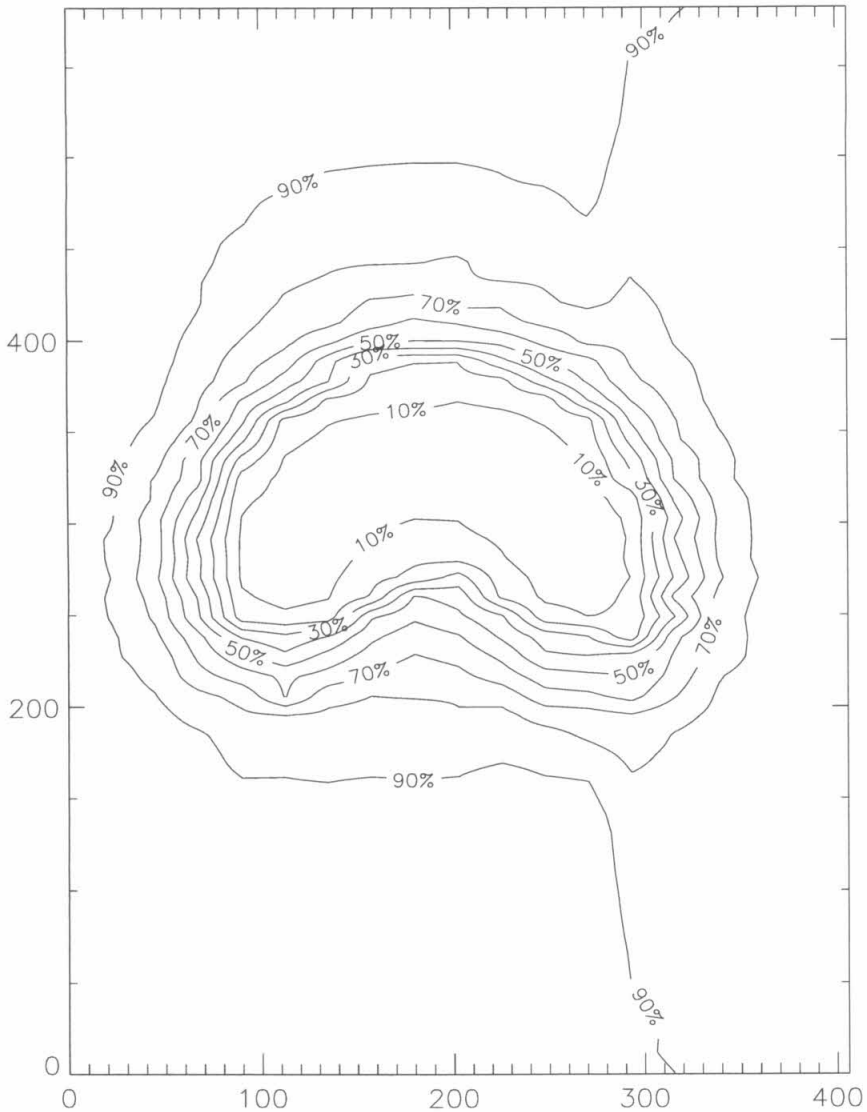

Figure 3.40 Contours of constant probe recovery temperature for the $u_{He}/u_{air} = 1.7$, 4.5° ramp case at $x/d = 49.2$. Axes are in hundredths of jet exit diameters. $T_{max} = 301$ K, $T_{min} = 262$ K

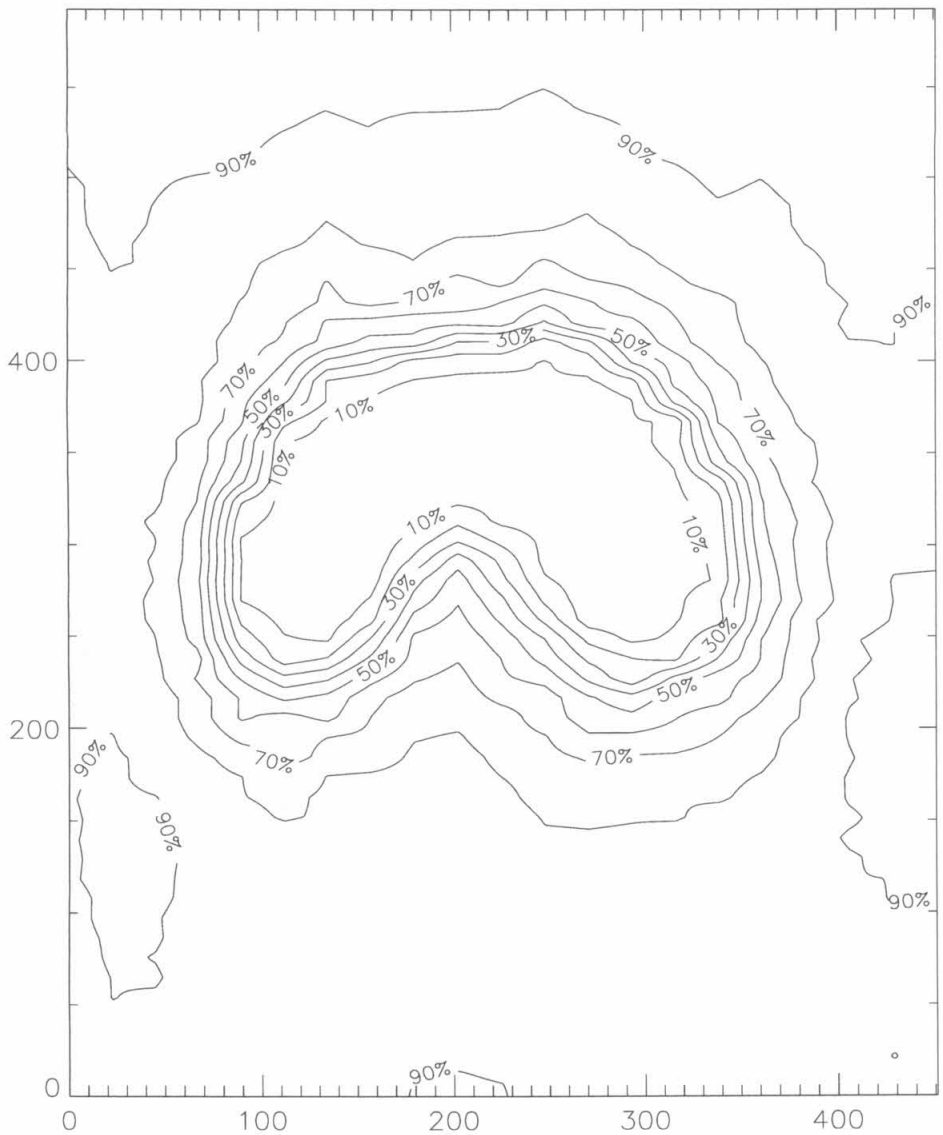

Figure 3.41 Contours of constant probe recovery temperature for the $u_{He}/u_{air} = 1.7$, 4.5° ramp case at $x/d = 66.4$. Axes are in hundredths of jet exit diameters. $T_{max} = 296$ K, $T_{min} = 265$ K

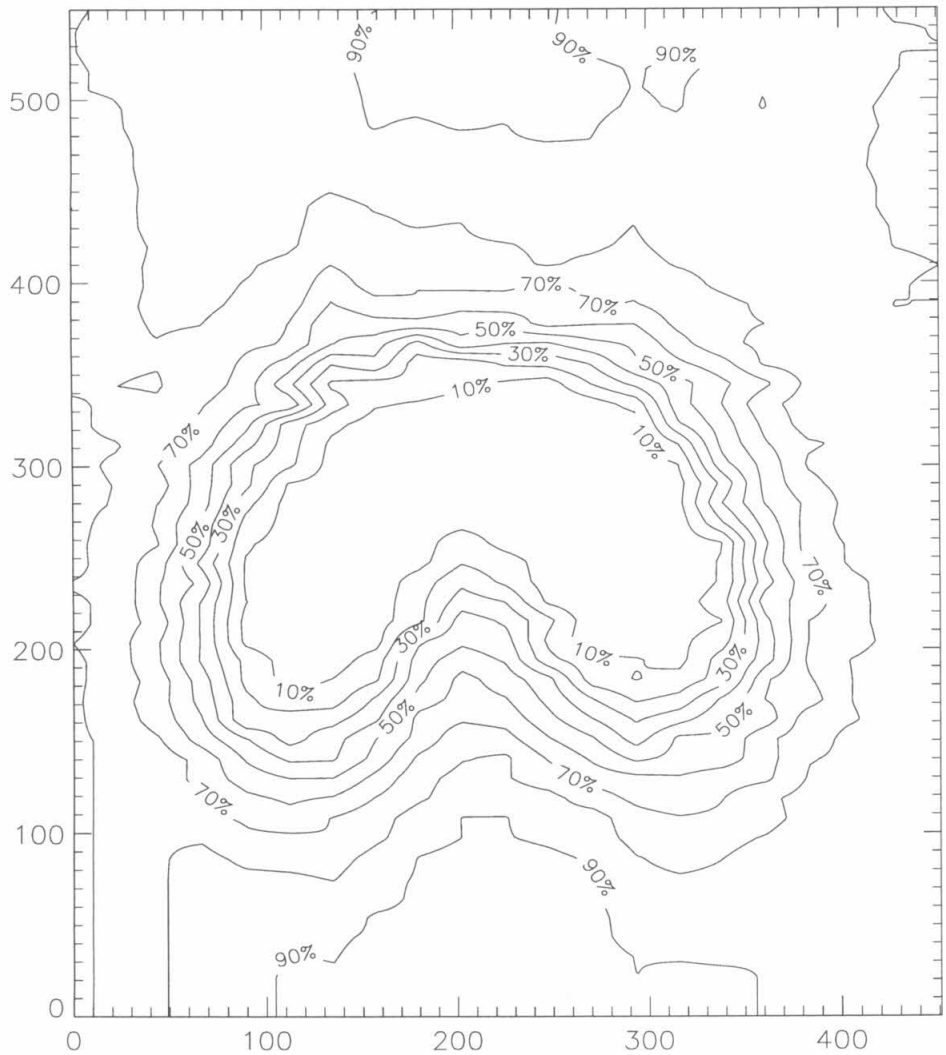

Figure 3.42 Contours of constant probe recovery temperature for the $u_{He}/u_{air} = 1.7$, 4.5° ramp case at $x/d = 83.6$. Axes are in hundredths of jet exit diameters. $T_{max} = 293$ K, $T_{min} = 269$ K

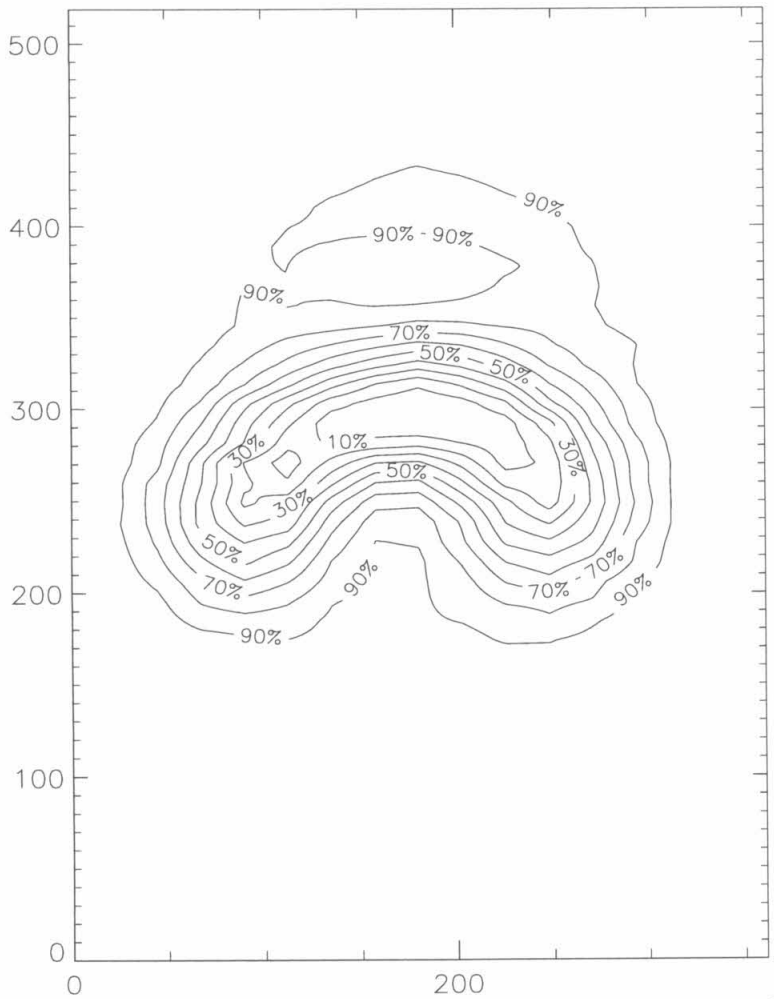

Figure 3.43 Contours of constant probe recovery temperature for the $u_{He}/u_{air} = 1.32$, 7.0° ramp case at $x/d = 32.8$. Axes are in hundredths of jet exit diameters. $T_{max} = 297$ K, $T_{min} = 258$ K

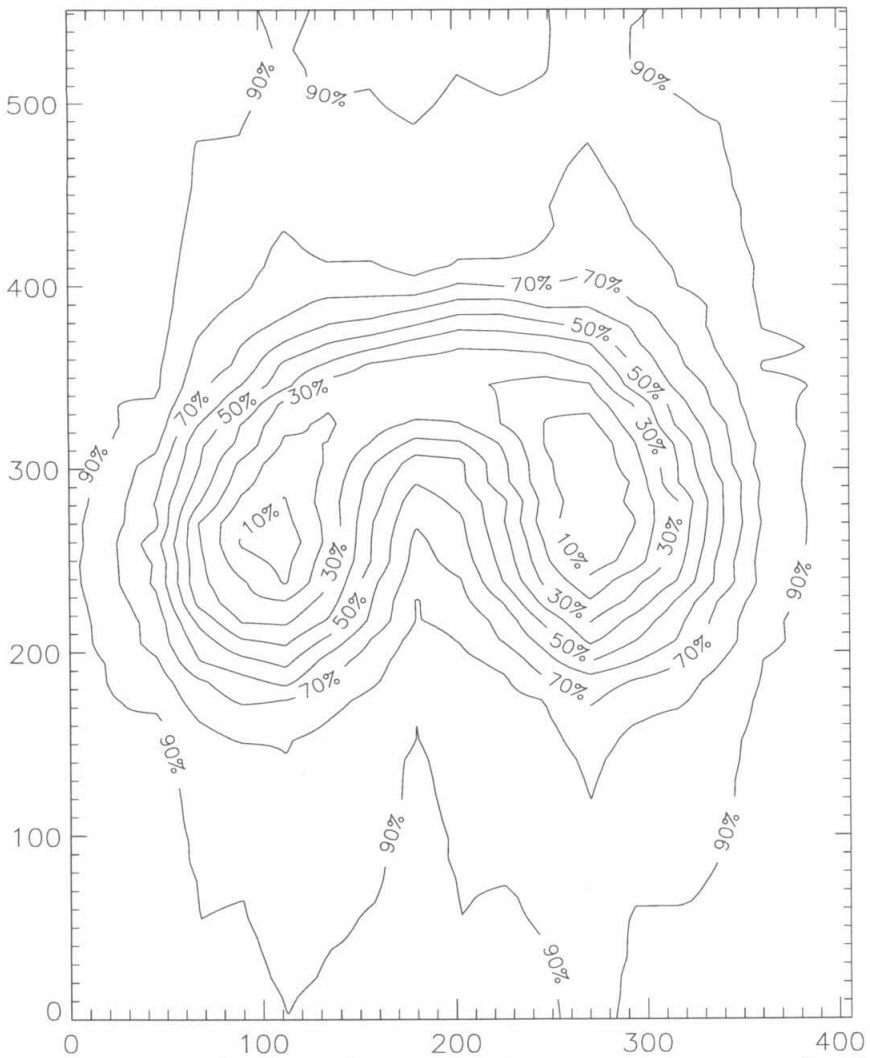

Figure 3.44 Contours of constant probe recovery temperature for the $u_{He}/u_{air} = 1.32$, 7.0° ramp case at $x/d = 49.2$. Axes are in hundredths of jet exit diameters. $T_{max} = 297$ K, $T_{min} = 278$ K

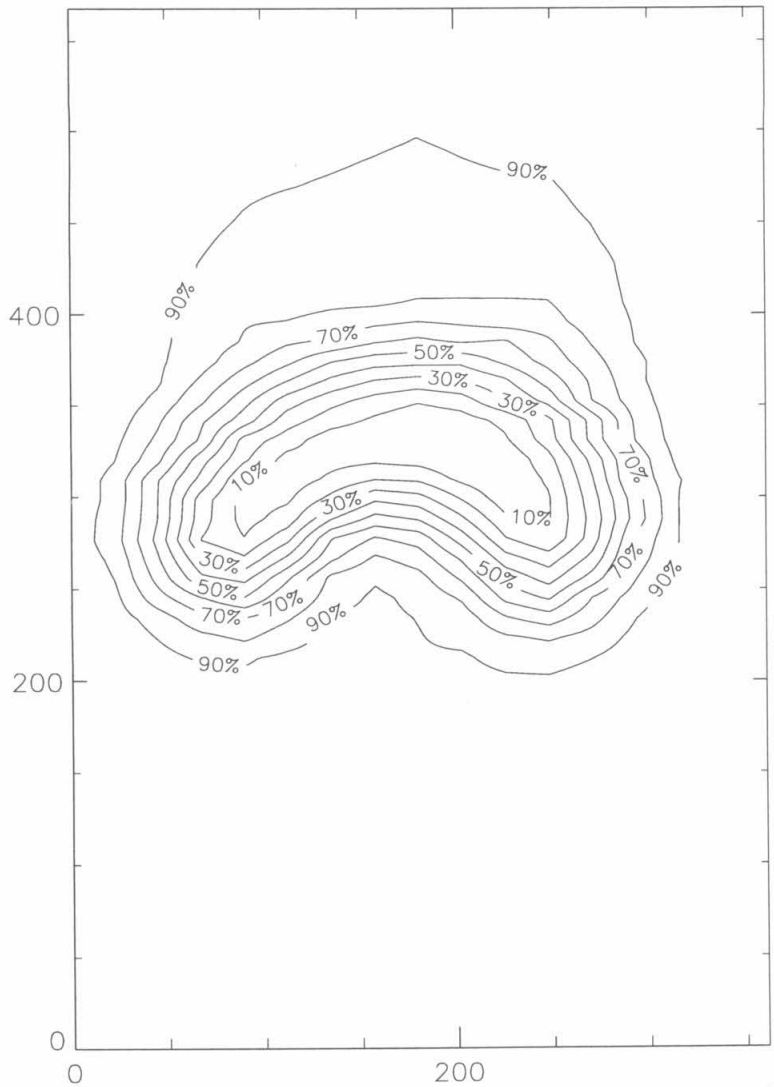

Figure 3.45 Contours of constant probe recovery temperature for the $u_{He}/u_{air} = 1.7$, 7.0° ramp case at $x/d = 32.8$. Axes are in hundredths of jet exit diameters. $T_{max} = 291$ K, $T_{min} = 261$ K

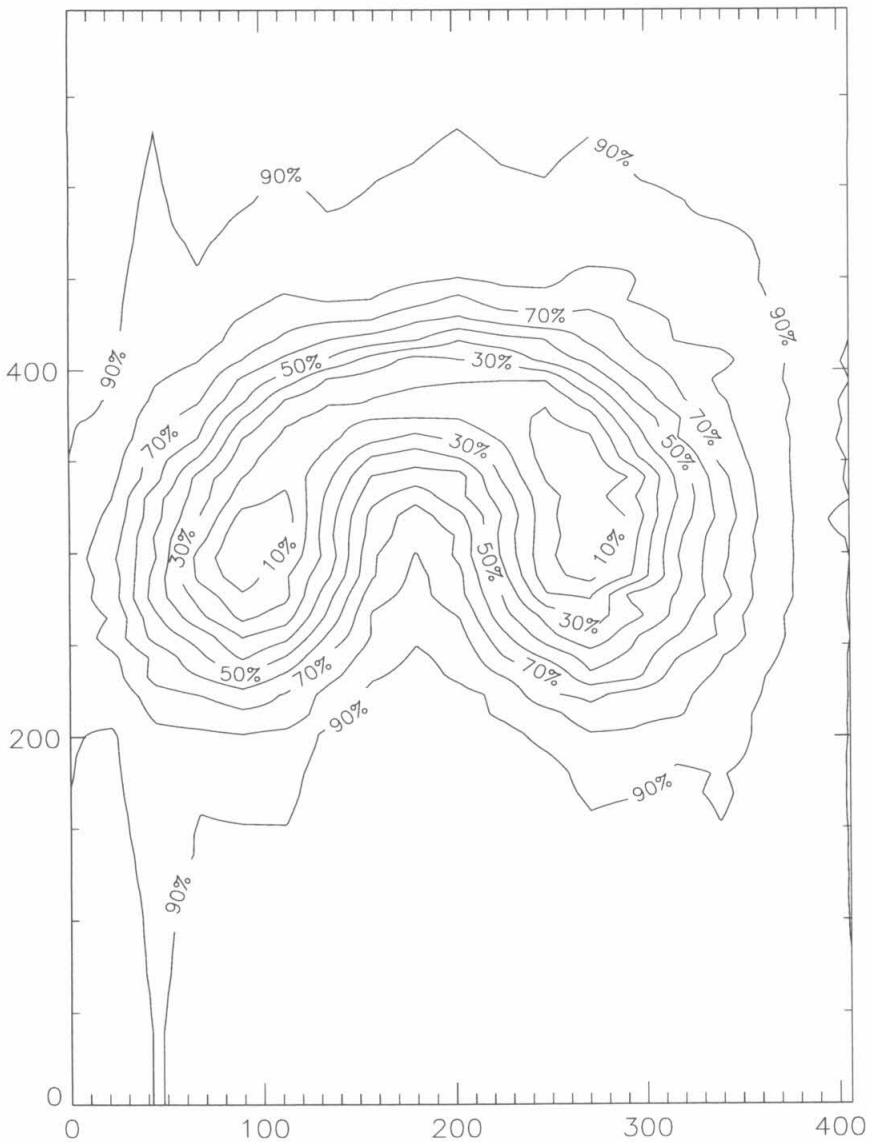

Figure 3.46 Contours of constant probe recovery temperature for the $u_{He}/u_{air} = 1.7$, 7.0° ramp case at $x/d = 49.2$. Axes are in hundredths of jet exit diameters. $T_{max} = 295$ K, $T_{min} = 272$ K

Chapter 4

Flow Visualization Results

4.1 Schlieren Method

All of the schlieren photos shown in this section are printed in landscape. If the page is rotated 90° degrees clockwise the flow will be from left to right. The schlieren photos in Figures 4.1 through 4.4 are for the 1.32 velocity ratio case with no ramp installed in the test section.

Figure 4.1 shows the flow in the nozzle and at the injector exit. Weak waves can be seen coming off of the portion of the injector where the outer tube constricts to meet the inner tube. These waves can been seen hitting the top and bottom tunnel walls downstream of the nozzle exit, indicating that the injector was inside the test rhombus of the nozzle. The condensation shock can also be seen just downstream of the throat.

Figure 4.2 is a close up view of Figure 4.1 showing the flow near the injector exit. The flow appears to be coming straight out of the injector and into the freestream; no waves can be seen originating at the injector exit. This indicates that the pressure between the air and the freestream is matched.

Figures 4.3 and 4.4 show the jet as it moves into the test section.and then further downstream. The vertical bar in Figure 4.4 can just be seen at the extreme downstream end of Figure 4.3. Some of the turbulent structure of the jet can be made out in these photos.

Figures 4.5 through 4.7 show schlieren pictures from the case with a 7.0° ramp

and a velocity ratio $u_{He}/u_{air} = 1.32$. They progress in order downstream from the nozzle. The compression of the jet immediately downstream of the shock can be seen in Figure 4.6. The same figure also shows how the jet was initially turned by an angle greater than that of the surrounding air. This effect is strongest for the 7.0° ramp cases and cannot be discerned in the pictures from the 4.5° runs. The motion of the jet relative to the air in this initial region can be considered that portion of the flow immediately after the impulse where the jet fluid is moving like a solid body with respect to the air. After that point the effects of the vorticity take over and the jet is transformed into a vortex pair, absorbing part of the energy of the relative motion [23].

By the time the jet reaches the part of the tunnel pictured in Figure 4.7 it is very hard to pick out from the rest of the flow; the increase in background noise as the flow approaches the end of the ramp is partially the cause of this. The other reason is that the jet is rapidly growing diffuse, weakening the schlieren signal.

4.2 Rayleigh Scattered Images

Images were taken at every streamwise station where pressure and temperature surveys were made as well as at selected stations in between them. The average data set included 30 images of the jet, 5 reference images taken with the tunnel and jet off, 2 dark images (used to correct for dark noise), and 2 images of a grid placed in the imaging plane in the tunnel (used to correct the images for the off-axis viewing angle as well as to provide a position reference). See Appendix B for a description of the data reduction of the Rayleigh scattered images. Appendix E contains additional images which supplement those described in this section.

The images displayed in Figures 4.8 and 4.9 are cross sections of the velocity ratio 1.32 jet taken one diameter downstream of the injector exit. The very bright circular region offset to the right in those pictures is caused by scattering off of the lip of the injector exit. The camera's off-axis viewing angle causes them to be offset from the axis of the jet. Small bright regions can be seen above and below the jet. It

is believed that these are caused by a non-uniform distribution of ice crystal size and number density which is in turn caused by the flow over the injector in the nozzle. As the injector passes through the expansion section of the nozzle, a component of the flow's velocity is parallel to the y-axis. This draws fluid along the injector's outer wall to it's top and bottom, where the fluid is then drawn into the freestream. Section B.2 contains an analysis showing that the intensity of light scattered by the ice crystals is proportional to the third power of the crystal radius; this includes the effect of decreased ice crystal number density with increasing crystal size due to the constant amount of water in the air. This third-order dependence of the scattered intensity on the ice crystal size ensures that any slight variation in crystal size in the tunnel shows up as a large change in signal at the ccd camera.

Figures 4.10 and 4.11 were taken 16.4 diameters downstream of the jet exit (for the velocity ratio 1.32 case); the non-uniform regions can still be seen as lighter areas above and below the jet. The variations from frame to frame indicate that the flow is unsteady and turbulent. By 32.8 diameters downstream (Figures 4.12 and 4.13) of the jet exit the size of the jet has noticeably increased and the non-uniform regions can be seen moving into other parts of the jet. The jet cross sections appear quite similar to what would be expected for a subsonic turbulent jet.

The jet continues increasing in size in Figures 4.14-4.19, the first two having been taken 49.2 diameters downstream and the last two 83.6 diameters downstream. Most of the pictures taken at or after x/d=66.4 show a marked increase in the randomness of the jet's shape. For comparison, Figures 4.20 and 4.21 were taken at x/d=83.6, just like Figures 4.18 and 4.19, but the jet velocity ratio was 1.7 instead of 1.32. The range of sizes and shapes of the jet shown by the images does not appear to vary much with only the change in velocity ratio.

Figures 4.22 through 4.27 were all taken with the 7.0° ramp and a velocity ratio of 1.32. Comparing them with their counterparts taken without the shock interaction, it is clear that the structure of the jet is much more chaotic for this case. This is especially true for frames like the one in Figure 4.27 where it appears that the jet has split into several distinct smaller regions. The pictures of the flow behind the

shock wave do not often show a distinct pair of vortices as seen in the time averaged measurements. When they do show the jet being split by the freestream fluid, they are quite often non-symmetric; the finger of freestream fluid moving into the jet tilts to one side or the other (see Appendix E for additional pictures of the jet being split by the freestream). Figure 4.25 is an exception to this and has a symmetric appearance quite similar to the time averaged measurements. The less structured flow pictured in the other images (*e.g.*, 4.27) leads to the conclusion that the flow deviates significantly from the mean and that turbulence effects which are not present in the previous two-dimensional studies are important in its development. In spite of this, the larger size and more chaotic nature of the jet after the shock interaction also leads to the conclusion that the shock does assist in the mixing of the jet with the freestream.

As mentioned above, the nonuniform distribution of ice crystals above and below the injector made any quantitative measure of the jet difficult. However, since the crystals started only above and below the jet it was possible to make some measurements involving only the horizontal axis through the jet centerline. The measurements could only be made at the most upstream stations, since as the jet moved downstream the turbulent nature of the flow guaranteed that some of the larger ice crystals would move down onto the horizontal axis of the jet.

Figure 4.28 was made by averaging together all 30 of the laser pictures taken at x/d=16.4 for the case with a velocity ratio of 1.32 and no shock wave. The horizontal line running across it is where the data in Figure 4.29 was taken from. The bright regions to the top and the bottom of the jet are plainly visible, but they have not spread visibly to the sides of the jet by the x/d=16.4 station. Therefore, horizontal slices of the light scattered data at that station do not suffer from the loss of information caused by the non-uniform ice crystals. Figure 4.30 is a horizontal slice of the time averaged temperature data for the same case. A comparison of the shapes of the data in Figures 4.29 and 4.30 shows that they are similar.

Figures 4.31 through 4.33 correspond to Figures 4.28 through 4.30, except that the jet velocity ratio was 1.7 instead of 1.32. The shapes of the image intensity and

temperature profiles in Figures 4.32 and 4.33 are similar, as in the $u_{He}/u_{air} = 1.32$ case; this self consistency of the data helps support the claim that the temperature data is an accurate time average of the jet and that the individual light scattered images provide meaningful information on the instantaneous condition of the jet.

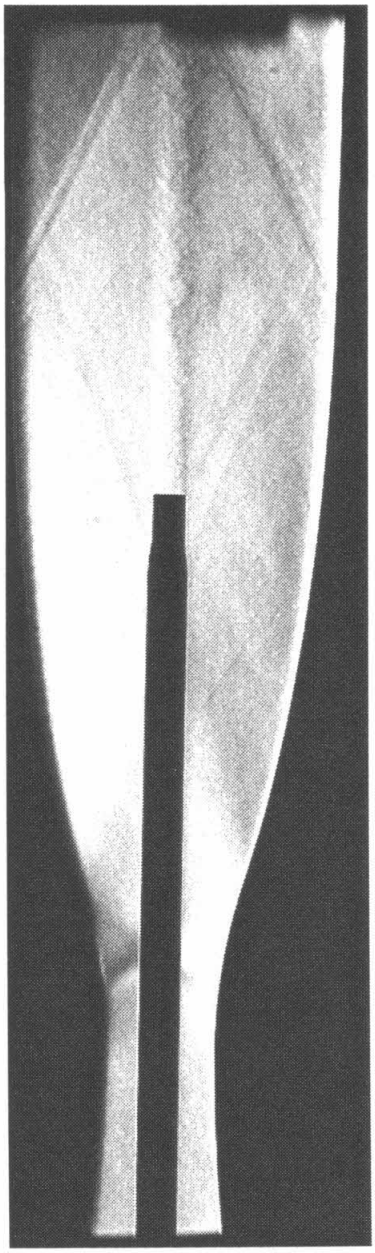

Figure 4.1 Schlieren for $u_{He}/u_{air} = 1.32$ case with no ramp. Station number 1

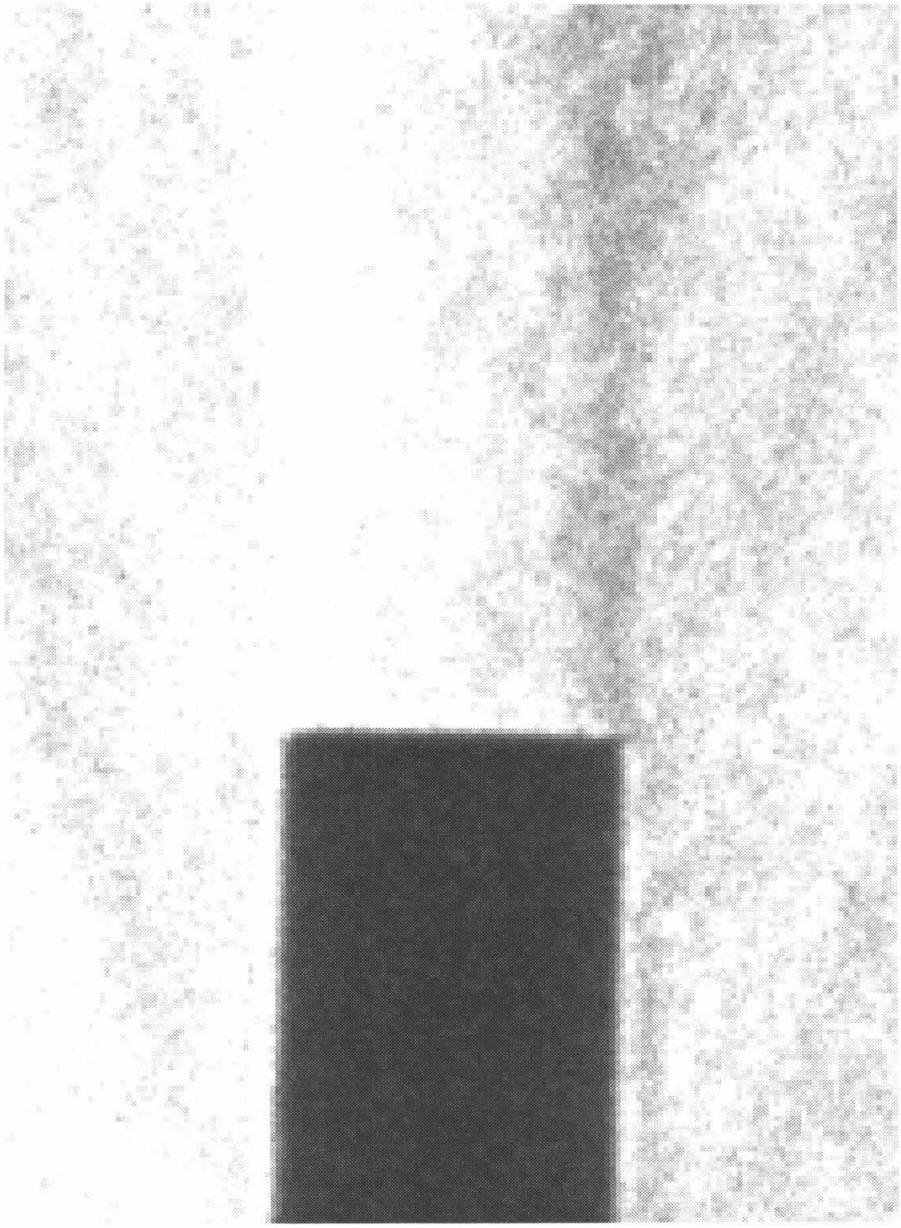

Figure 4.2 Close-up schlieren for $u_{He}/u_{air} = 1.32$ case with no ramp. Station number 1

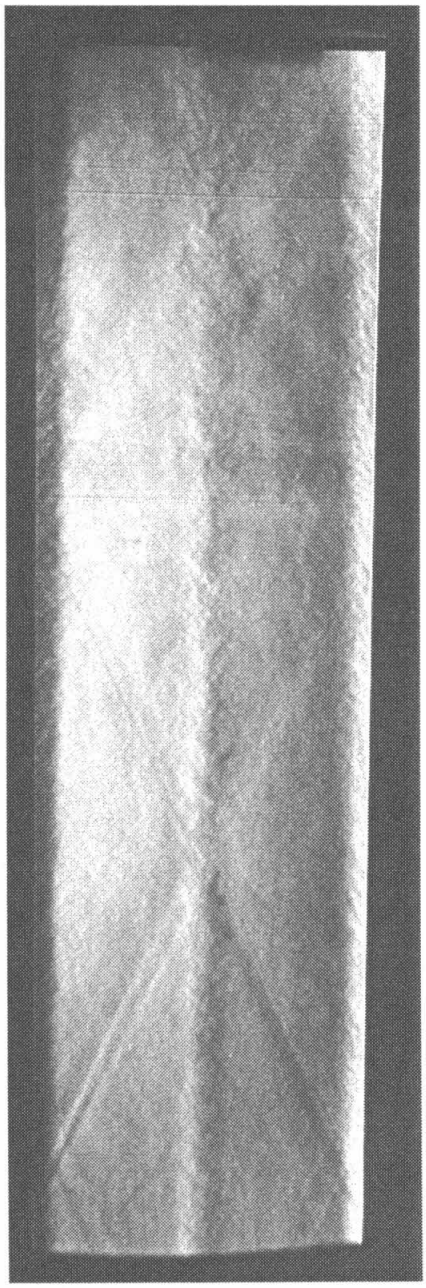

Figure 4.3 Schlieren for $u_{He}/u_{air} = 1.32$ case with no ramp. Station number 2

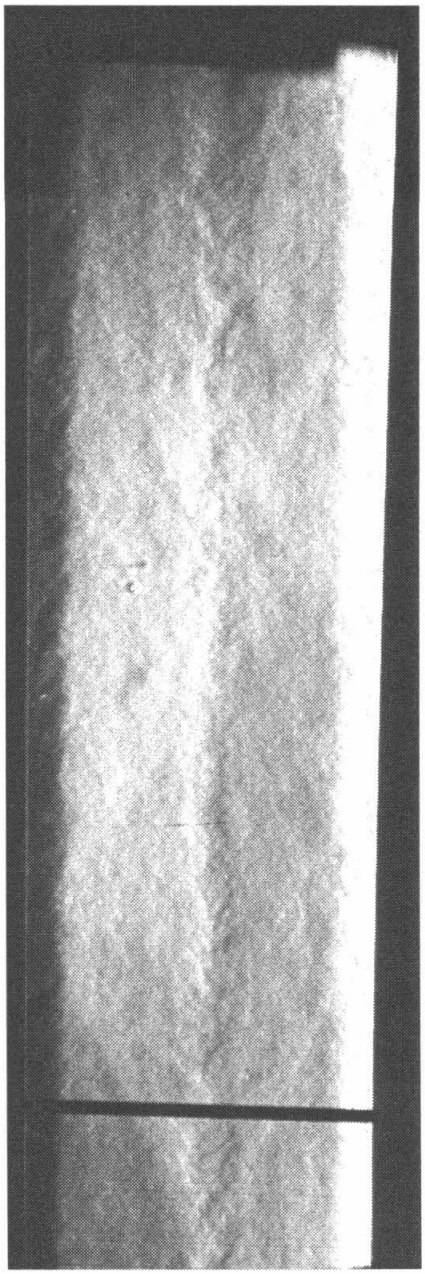

Figure 4.4 Schlieren for $u_{He}/u_{air} = 1.32$ case with no ramp. Station number 3

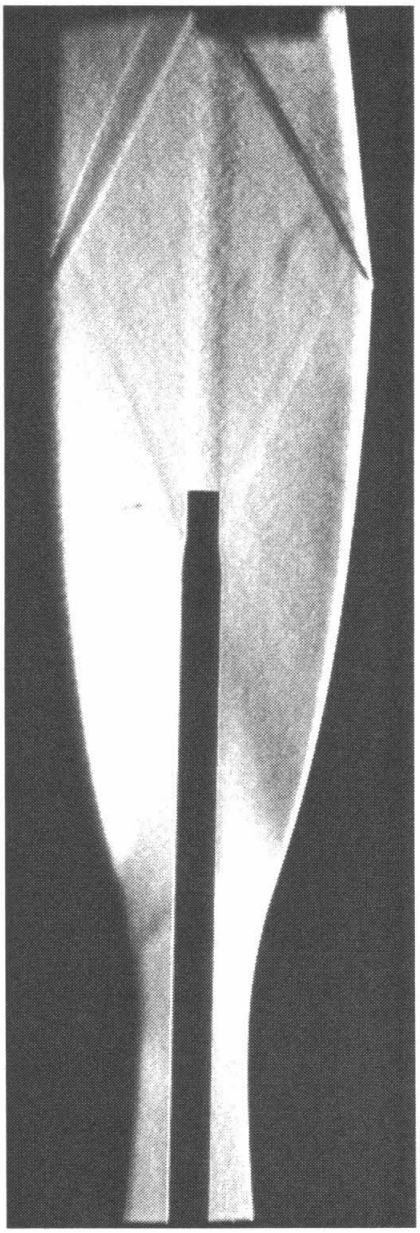

Figure 4.5 Schlieren for $u_{He}/u_{air} = 1.32$ case with 7° ramp. Station number 1

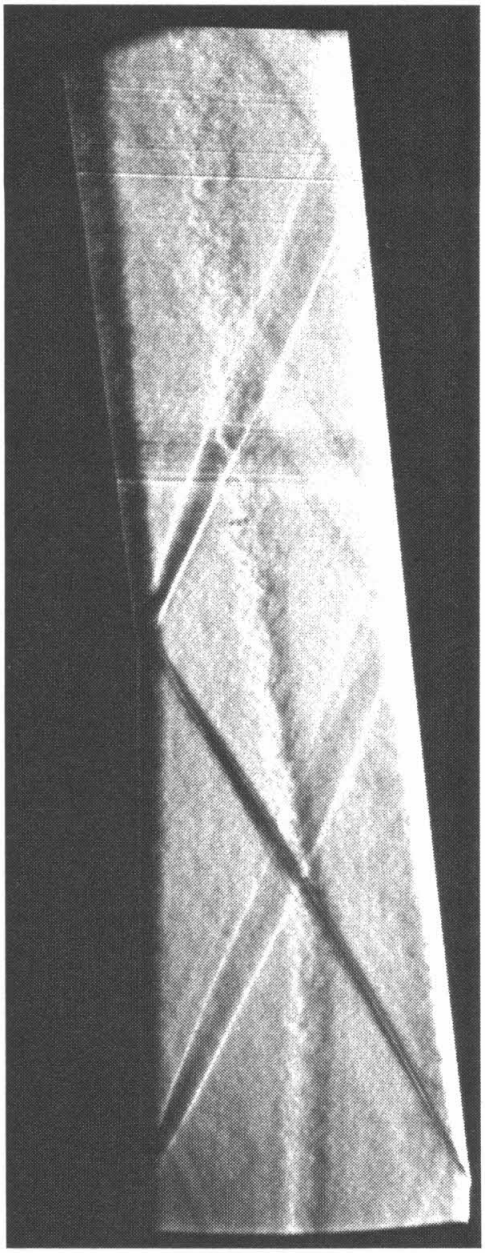

Figure 4.6 Schlieren for $u_{He}/u_{air} = 1.32$ case with 7° ramp. Station number 2

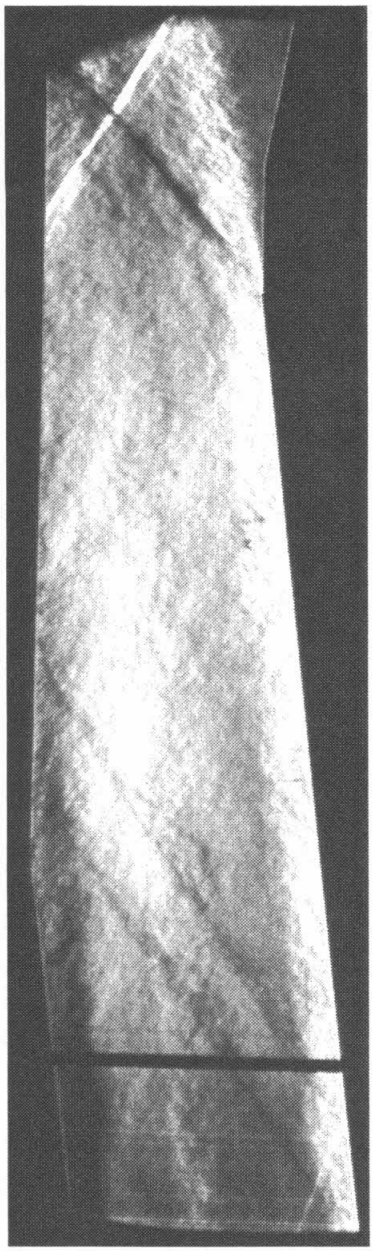

Figure 4.7 Schlieren for $u_{He}/u_{air} = 1.32$ case with 7° ramp. Station number 3

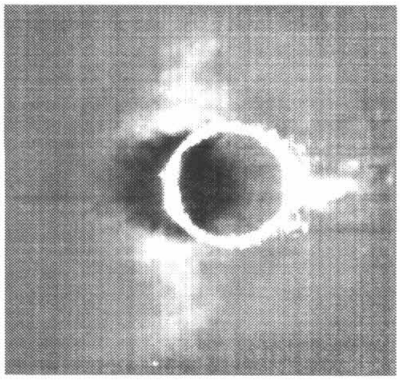

Figure 4.8 Rayleigh scattered image for the $u_{He}/u_{air} = 1.32$, no ramp case at x/d=01.0.

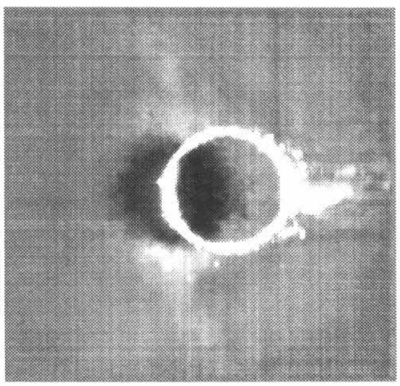

Figure 4.9 Rayleigh scattered image for the $u_{He}/u_{air} = 1.32$, no ramp case at x/d=01.0.

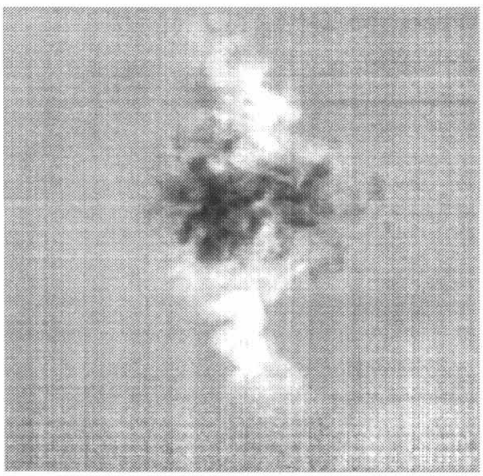

Figure 4.10 Rayleigh scattered image for the $u_{He}/u_{air} = 1.32$, no ramp case at x/d=16.4.

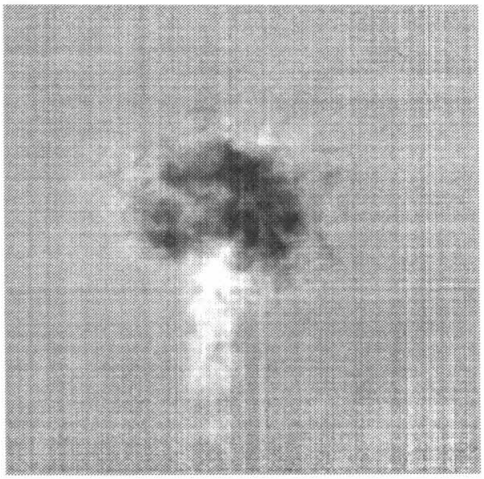

Figure 4.11 Rayleigh scattered image for the $u_{He}/u_{air} = 1.32$, no ramp case at x/d=16.4.

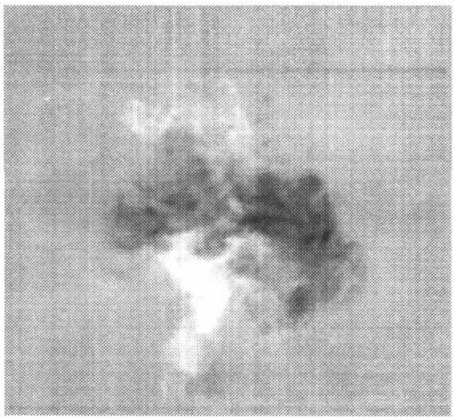

Figure 4.12 Rayleigh scattered image for the $u_{He}/u_{air} = 1.32$, no ramp case at x/d=32.8.

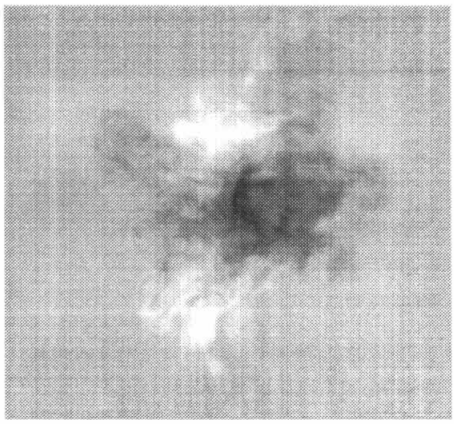

Figure 4.13 Rayleigh scattered image for the $u_{He}/u_{air} = 1.32$, no ramp case at x/d=32.8.

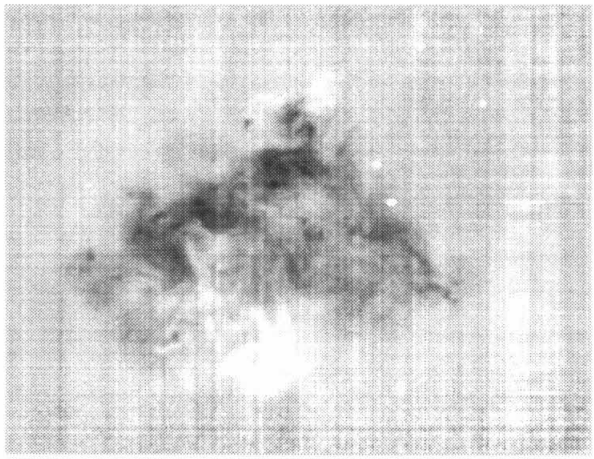

Figure 4.14 Rayleigh scattered image for the $u_{He}/u_{air} = 1.32$, no ramp case at x/d=49.2.

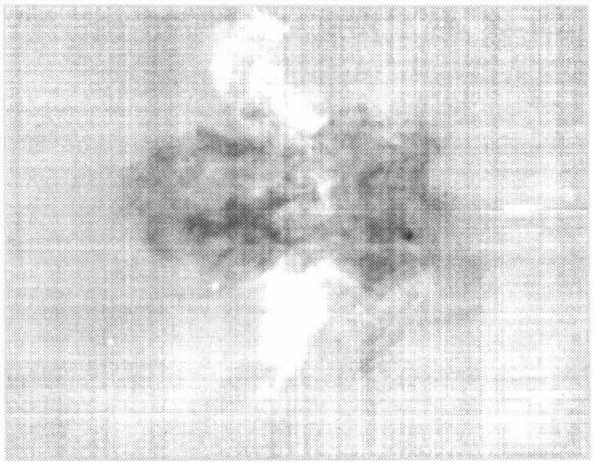

Figure 4.15 Rayleigh scattered image for the $u_{He}/u_{air} = 1.32$, no ramp case at x/d=49.2.

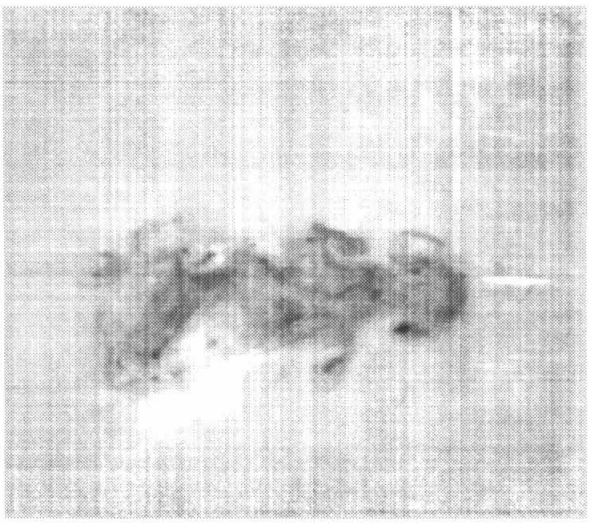

Figure 4.16 Rayleigh scattered image for the $u_{He}/u_{air} = 1.32$, no ramp case at x/d=66.4.

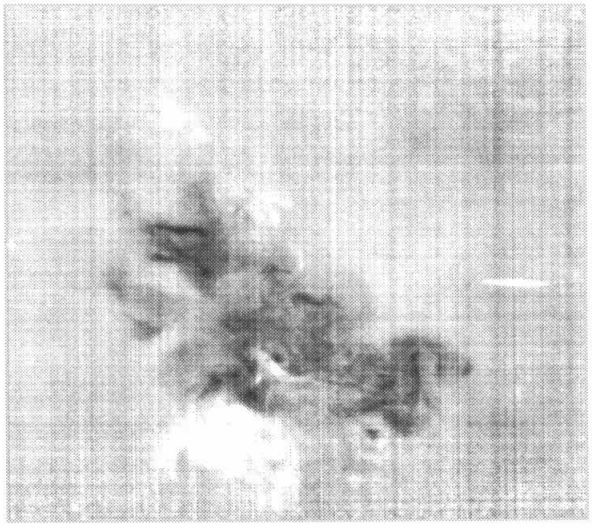

Figure 4.17 Rayleigh scattered image for the $u_{He}/u_{air} = 1.32$, no ramp case at x/d=66.4.

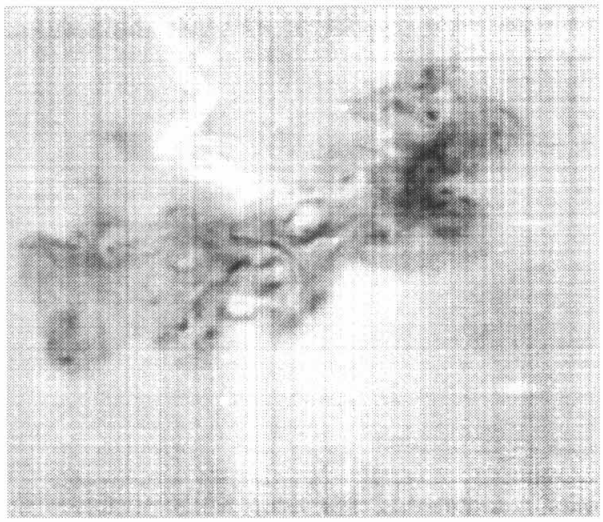

Figure 4.18 Rayleigh scattered image for the $u_{He}/u_{air} = 1.32$, no ramp case at x/d=83.6.

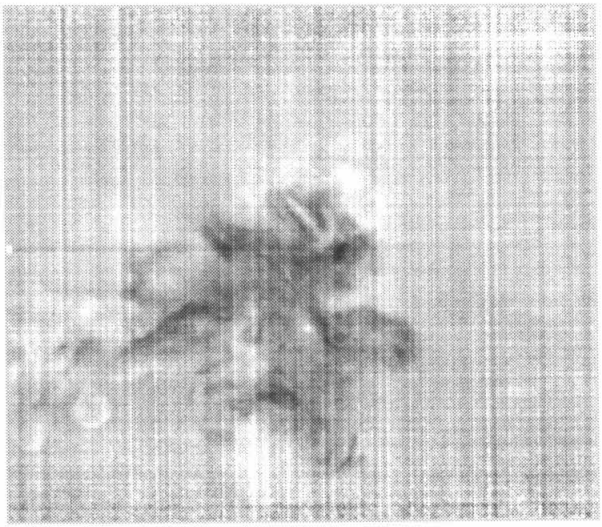

Figure 4.19 Rayleigh scattered image for the $u_{He}/u_{air} = 1.32$, no ramp case at x/d=83.6.

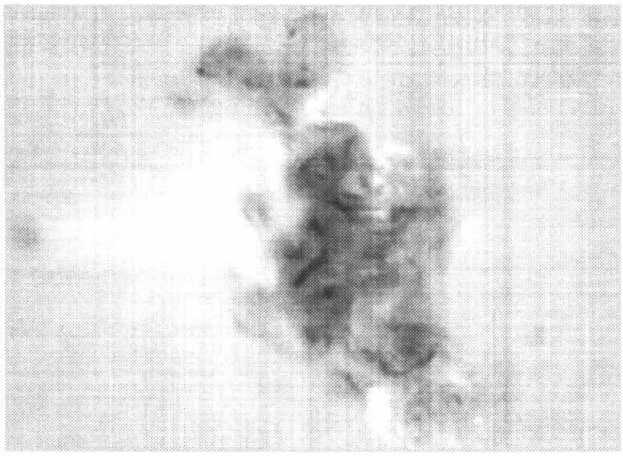

Figure 4.20 Rayleigh scattered image for the $u_{He}/u_{air} = 1.7$, no ramp case at x/d=83.6.

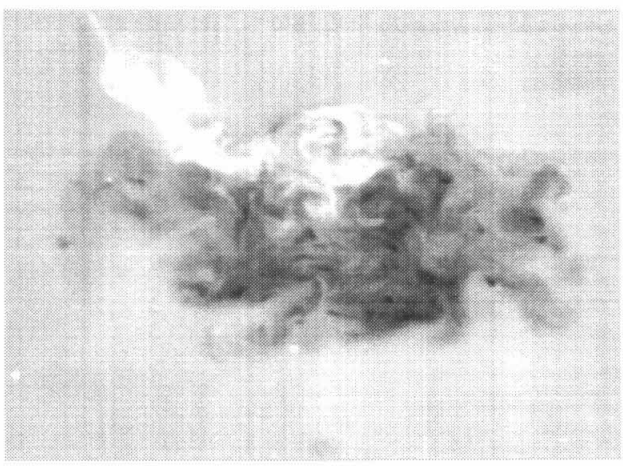

Figure 4.21 Rayleigh scattered image for the $u_{He}/u_{air} = 1.7$, no ramp case at x/d=83.6.

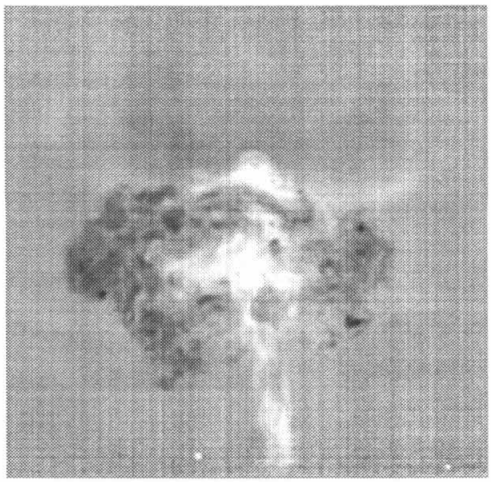

Figure 4.22 Rayleigh scattered image for the u_{He}/u_{air} = 1.32, 7.0° ramp case at x/d=32.8.

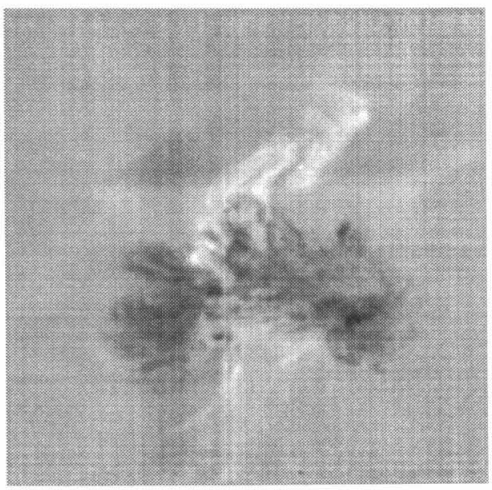

Figure 4.23 Rayleigh scattered image for the u_{He}/u_{air} = 1.32, 7.0° ramp case at x/d=32.8.

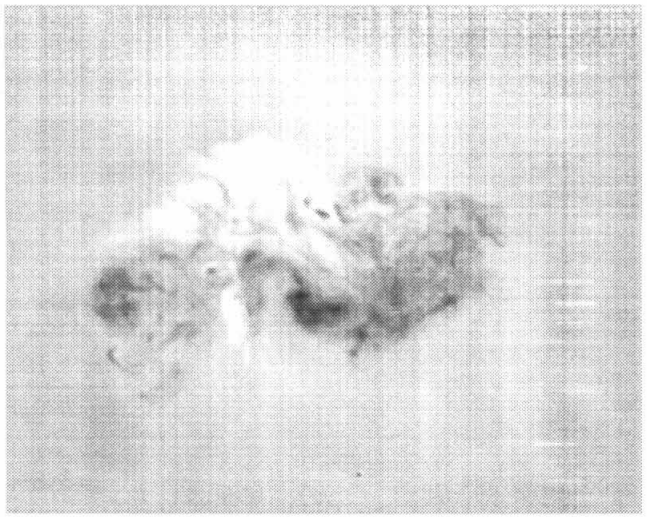

Figure 4.24 Rayleigh scattered image for the $u_{He}/u_{air} = 1.32$, 7.0° ramp case at x/d=49.2.

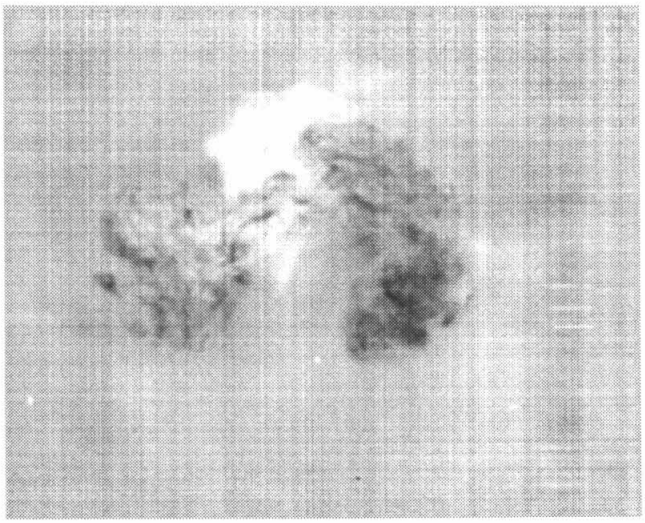

Figure 4.25 Rayleigh scattered image for the $u_{He}/u_{air} = 1.32$, 7.0° ramp case at x/d=49.2.

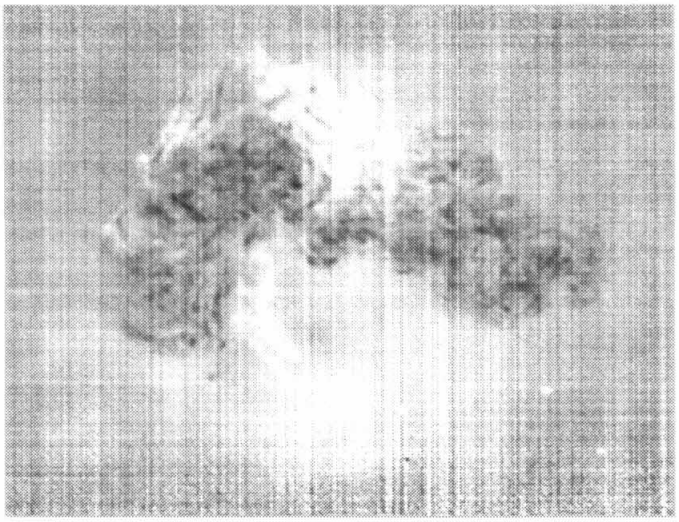

Figure 4.26 Rayleigh scattered image for the u_{He}/u_{air} = 1.32, 7.0° ramp case at x/d=66.4.

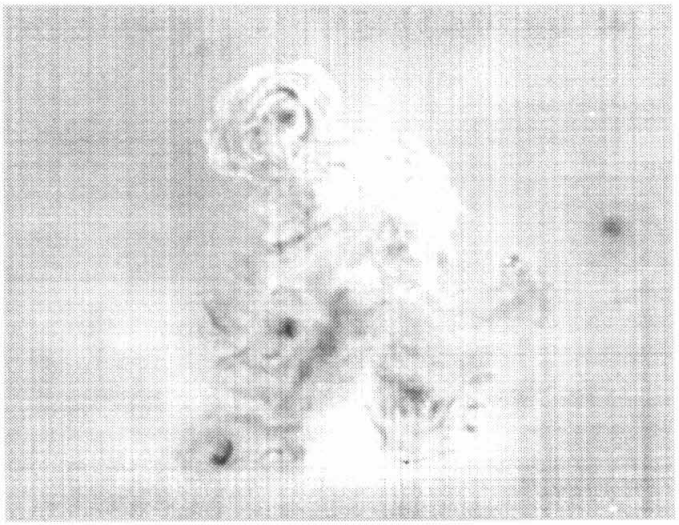

Figure 4.27 Rayleigh scattered image for the u_{He}/u_{air} = 1.32, 7.0° ramp case at x/d=66.4.

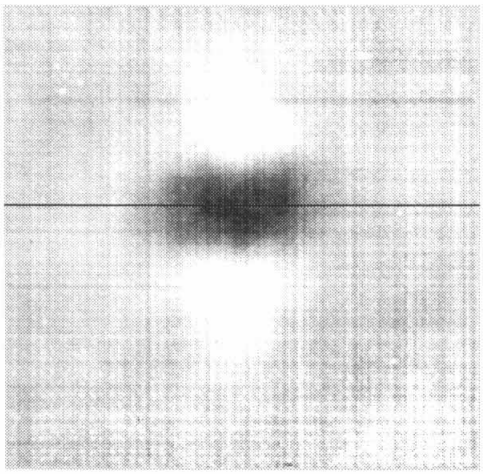

Figure 4.28 Average light scattered images from $u_{He}/u_{air} = 1.32$, no ramp case at x/d=16.4

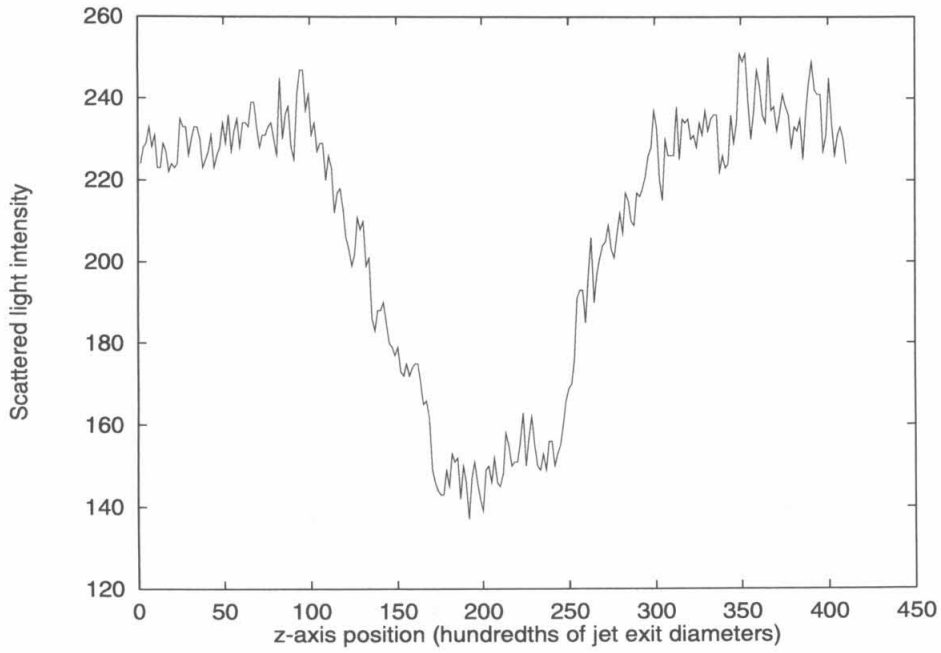

Figure 4.29 Row taken from average of light scattered images for $u_{He}/u_{air} = 1.32$, no ramp case at x/d=16.4

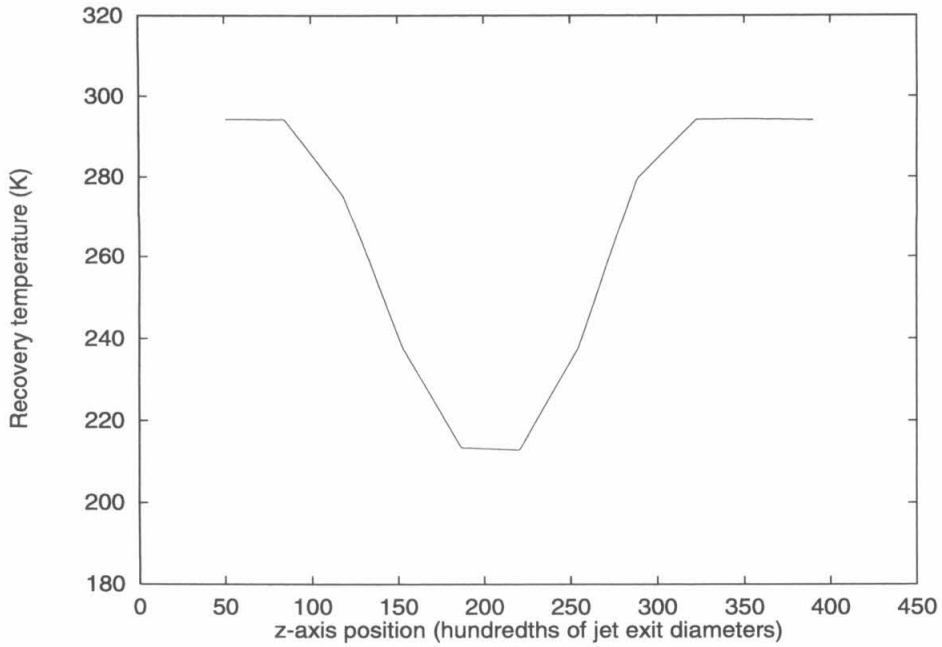

Figure 4.30 Row taken from time averaged temperature data for $u_{He}/u_{air} = 1.32$, no ramp case at x/d=16.4

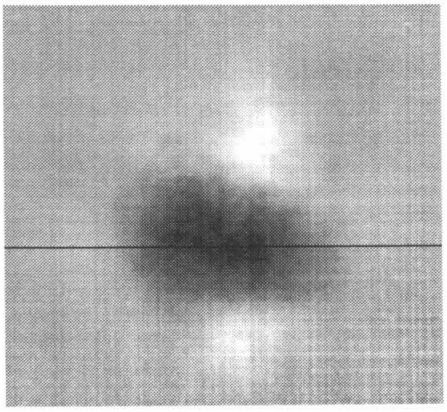

Figure 4.31 Average light scattered images from $u_{He}/u_{air} = 1.7$, no ramp case at x/d=16.4

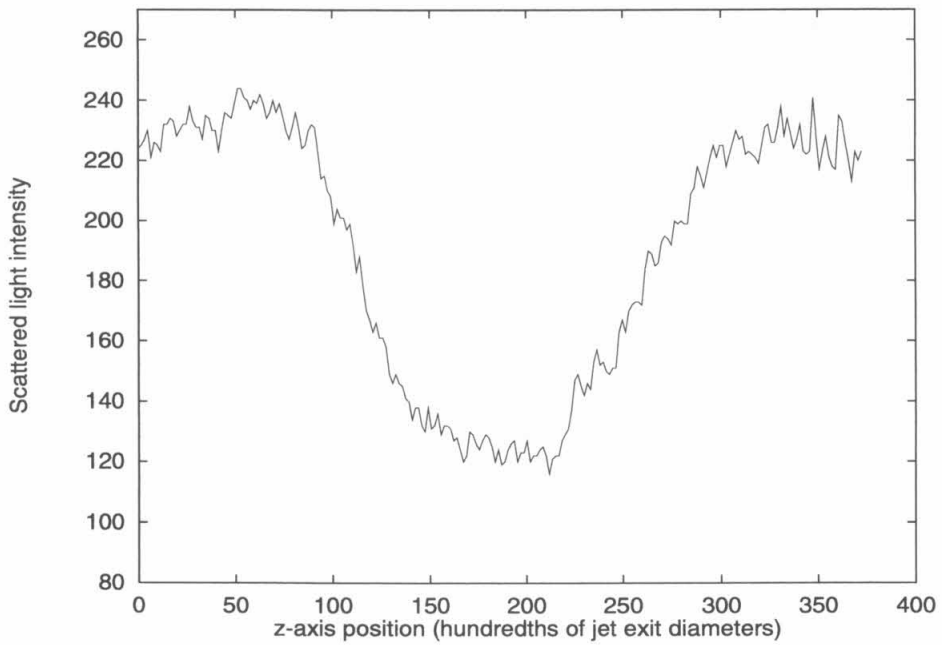

Figure 4.32 Row taken from average of light scattered images for $u_{He}/u_{air} = 1.7$, no ramp case at x/d=16.4

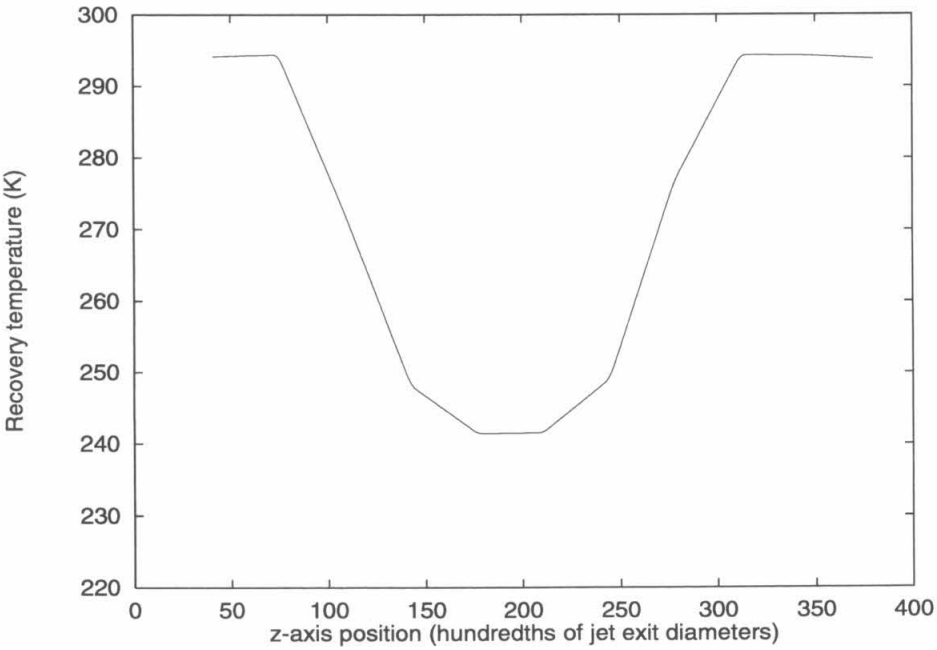

Figure 4.33 Row taken from time averaged temperature data for $u_{He}/u_{air} = 1.7$, no ramp case at x/d=16.4

Chapter 5

Growth and Deformation of the Jet

All of the figures in this chapter have keys which refer by number to the 5 experimental cases studied. In order, they are: (1) no ramp with $u_{He}/u_{air} = 1.32$, (2) no ramp with $u_{He}/u_{air} = 1.7$, (3) 4.5° ramp with $u_{He}/u_{air} = 1.7$, (4) 7.0° ramp with $u_{He}/u_{air} = 1.32$, and (5) 7.0° ramp with $u_{He}/u_{air} = 1.7$. The purpose of these figures is to summarize how the size and shape of the jet changed with downstream distance for the different experimental cases.

Figures 5.1 and 5.2 are plots of the area information contained in the pressure and temperature cross sections of Chapter 3. Figure 5.1 summarizes the pressure information, while Figure 5.2 summarizes the temperature information. The plots are understood to meet at an area of one at x/d=0.0. Both of these figures show the jet starting out larger for the 4.5° ramp case, but the growth rates of the jet area for the 7.0° cases are larger. These plots also reveal, as do the others described here, that the behavior of the flow depends much more heavily on the ramp angle than on the velocity ratio between the jet and the freestream.

Figure 5.3 shows the jet area measurements with the downstream distance scaled by the characteristic distance ($\hat{x}$ from Table 2.3) for each case with a shock wave. The slopes of the different curves match fairly well, indicating that the time scale based on Yang's model gives a rough collapse of the growth rate data. The horizontal offset between the curves is most likely caused by two things: first, by variation in the development of the flow upstream of the shock wave due to the case-to-case

variation of the velocity ratio between the jet and the freestream, and secondly, by the different changes in velocity ratio across the shock wave due to the change in shock strength for the different cases.

The results of the radius of gyration calculations described in Appendix C are displayed in Figures 5.4 (for the pressure data) and 5.5 (for the temperature data). They are a measure of the size of the jet, like the area measurements above, but they are a linear rather than a square measure. In spite of this difference they show the same trends with downstream distance and ramp angle as the area measurements.

Figures 5.6 and 5.7 plot the ratio of the horizontal and vertical components of the radius of gyration versus downstream distance as derived from pressure and temperature data, respectively. They can be considered a measure of the aspect ratio of the cross section of the jet. Yang's [32] two-dimensional calculations included cases with elliptical jets with aspect ratios of up to two; these calculations showed that the change in shape of the jet did not significantly affect the development of the flow.

Figures 5.8 and 5.9 consist of plots of the height of the jet's center of mass relative to the bottom tunnel wall, which were calculated from pressure and temperature contours, respectively. The trend for all cases is to increase height with downstream distance, but that is to be expected, since the top and bottom tunnel walls were not parallel, but instead slightly open to account for the boundary layer's growth. The rate of motion away from the bottom wall due solely to the increased tunnel height was approximately 0.87 diameters per 100 diameters of downstream travel (an angle of 0.5°).

The flow field induced by the two counter-rotating streamwise vortices generated by the shock-jet interaction is such that the vortices tend to move along the vertical (y) axis. The flow field from one tends to move the other up and vice versa. However, the incomplete formation of the vortices in these experiments, along with the influence of the tunnel walls (which cause the vortices to see their own reflections), prevents meaningful comparisons with the vortex propagation measurements made by Budzinski [3] and Yang [32].

5.1 Vortex Separation

Figures 5.10 and 5.11 show the horizontal separation of the vortices. These data were generated by finding the center of mass for the jet, splitting the jet in half along a vertical line going through the center of mass, and then finding the separation of the center of masses of the two halves. While this method of measuring the width of the jet does not have much relevance to the cases with no shock, it does provide a measure of the vortex separation if the vortex cores are distinct from one another. Both the pitot pressure and the temperature plots show increasing separation and rate of separation for the 7.0° ramp cases when compared with the 4.5° cases, and all of the data is grouped by ramp angle rather than velocity ratio.

The plots in Figures 5.12 and 5.13 are of the horizontal component of the radius of gyration. This provides another measure of the width of the jet along the z-axis. Comparison of these plots with the two previous reveals the same basic trends of increasing separation with increasing ramp angle and little dependence on the velocity ratio.

5.2 Comparison with Previous Investigations

Figure 5.14 is a black and white reproduction of a figure taken from Budzinski's thesis [3]; it shows a series of images from the analogous two-dimensional flow which he studied. The density ratio across the interface and the pressure ratio across the shock are close to those for the $7.0°, u_{He}/u_{air} = 1.32$ case of the present study. The pictures were taken using a laser light sheet to scatter light off of the atoms and molecules present in the shock tube. The brighter regions inside the jet are an artifact of the false coloring of the original image.

The individual frames show the development of the two-dimensional flow in time in order from (a) to (j). The shock can be seen traveling from the bottom to the top in frames (b), (c), and (d). Using Yang's [32] method to calculate a characteristic time, the values of t/τ for the frames of interest are 10 for (e), 15 for (f), 20 for (g), and 31 for (h).

Using $\hat{x} = 3.81$ for the distance scale, which corresponds to the development of the flow by 1 τ in time, and x/d=17 for location of the shock intersection with the jet gives an equivalent t/τ value of 13 for the jet at the x/d=66.4 station. A comparison of Figure 3.22 and Figures 5.14(e) and (f) suggests that Yang's models for the circulation and characteristic time can probably be applied to the time averaged three-dimensional flow with some success. The flow appears to be slightly more developed into a distinct vortex pair at the corresponding dimensionless time scale for Budzinski's data. One factor contributing to this discrepancy is the unsteady nature of the flow studied here. The time resolved light scattered images show that the position of the jet in the tunnel changes with time, which indicates that the time averaged measurements have, to some extent, spatially averaged the flow. Thus, it is possible that the flow may, on average, be as developed as the corresponding one studied by Budzinski, but since the vortex pair is also moving within the tunnel the separation of the pair has been washed out somewhat in the time averaged measurements.

Figures 4.24 through 4.26, as well as Figures E.8 through E.11, show jet cross sections where the flow appears to be quite well developed. The turbulence present in the flow causes quite a bit of variation from frame to frame, but they all show, to a greater or lesser extent, a jet of freestream fluid moving up and diving the helium jet.

In addition to the changes to Yang's model discussed in Section 1.2.3, it was necessary to make estimates on the size and density of the jet at the point where it interacted with the shock. These were based on the temperature data taken at that point for the cases without a shock, but the unsteady nature of the flow guaranteed that the time averaged measurements did not provide complete information. Considering the spatial averaging of the flow as well as the approximations made to get numbers to put into Yang's model, the agreement between the pictures taken by Budzinski and the time averaged measurements of Chapter 3 is rather good.

Similar comparisons with jet profiles calculated by Yang and measured by Jacobs (in Yang [32]) also show the same general shape as the time averaged profiles

taken in these experiments. Figure 5.15(a) shows the result of one of Yang's calculations at t/τ=9.6, while Figure 5.15(b) is for a value of t/τ of 15. Figure 5.16(a) shows a picture taken by Jacobs (also from Yang's thesis) using planar laser induced fluorescence for which t/τ=12, and Figure 5.16(b) is for the same conditions at a non-dimensionalized time of t/τ=14.

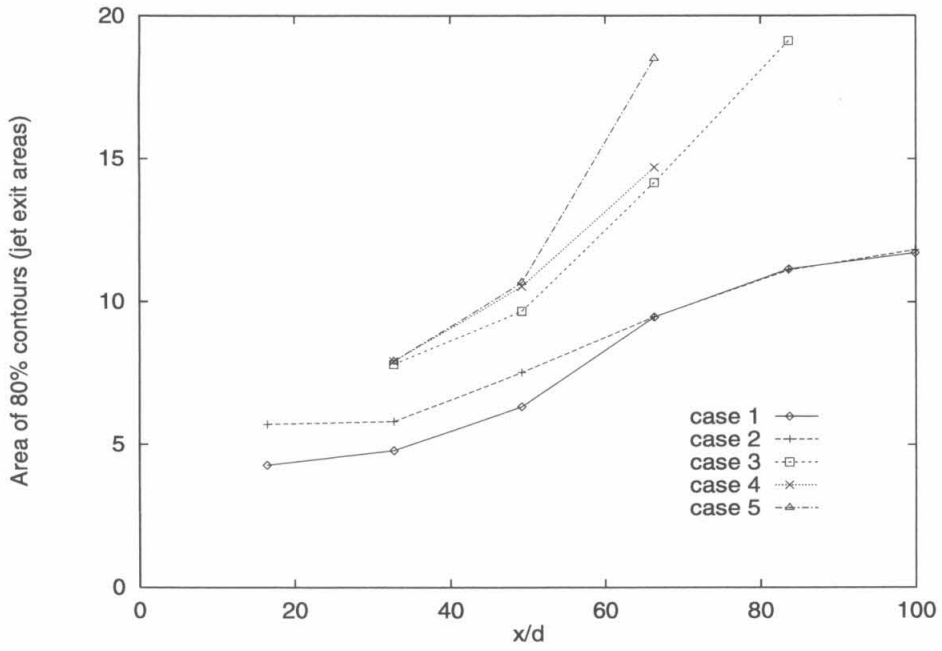

Figure 5.1 Jet area from pitot pressure data

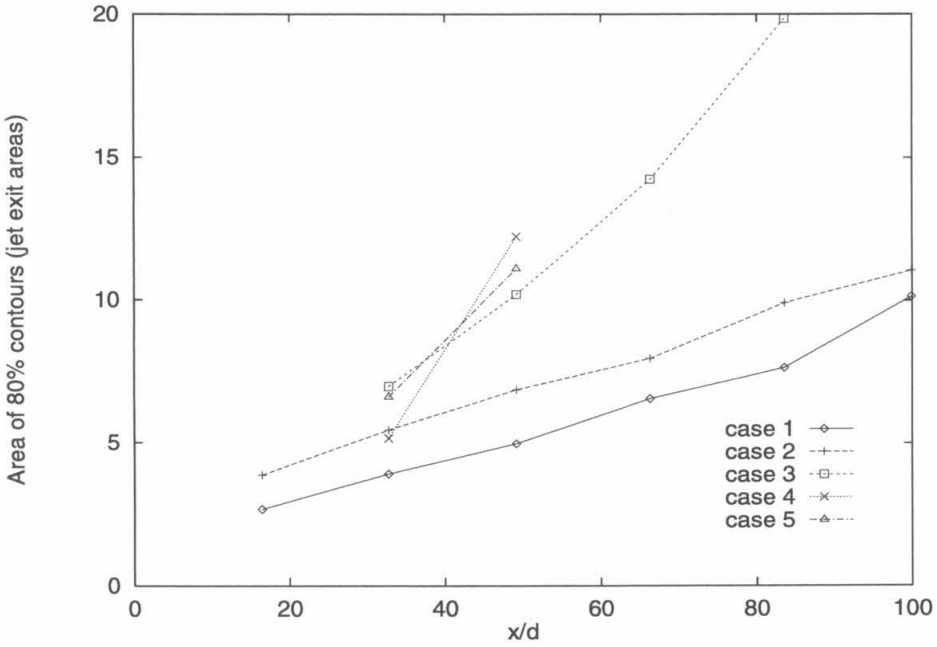

Figure 5.2 Jet area from recovery temperature data

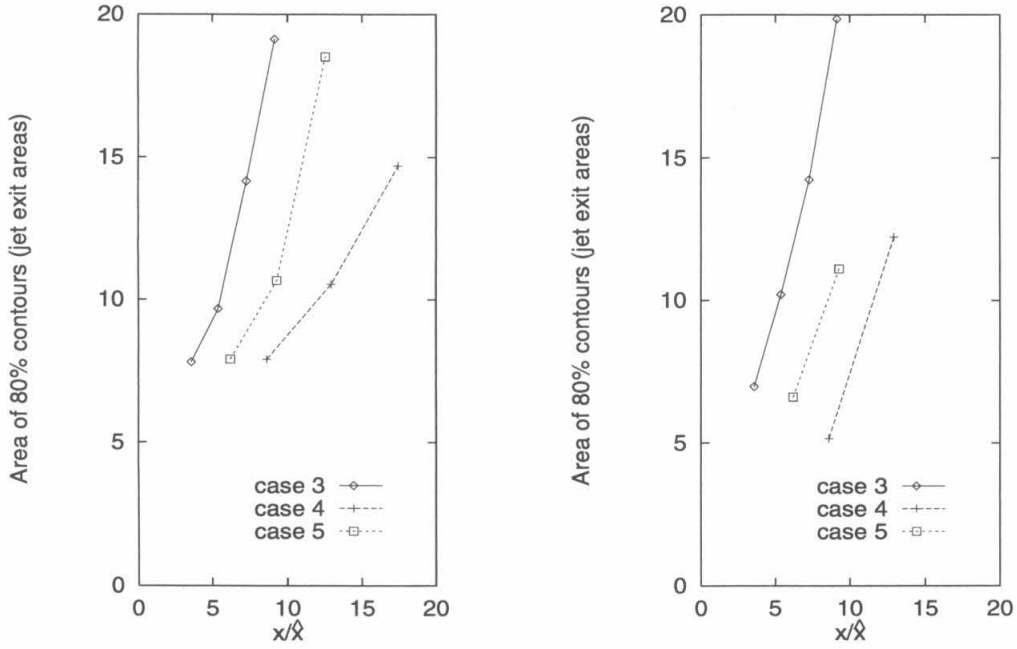

Figure 5.3 Jet area from recovery temperature and pressure data for cases with a shock. Streamwise coordinate scaled by characteristic distance

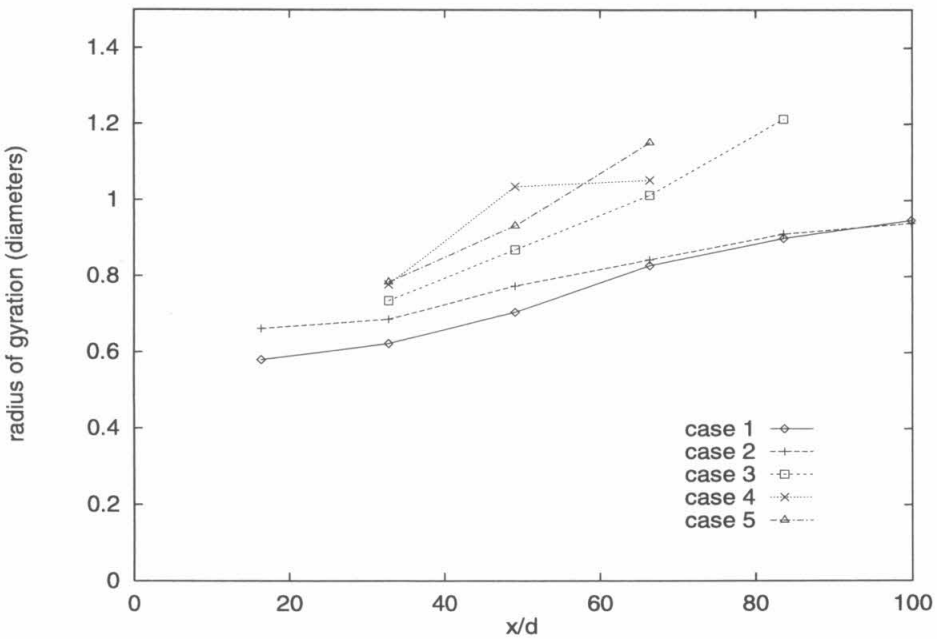

Figure 5.4 Jet radius from pitot pressure data

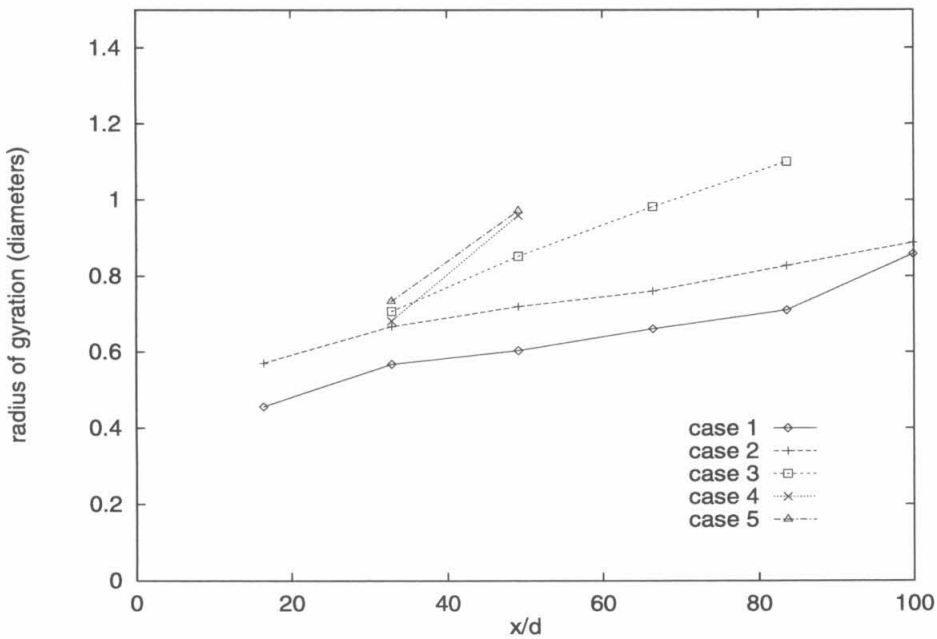

Figure 5.5 Jet radius from recovery temperature data

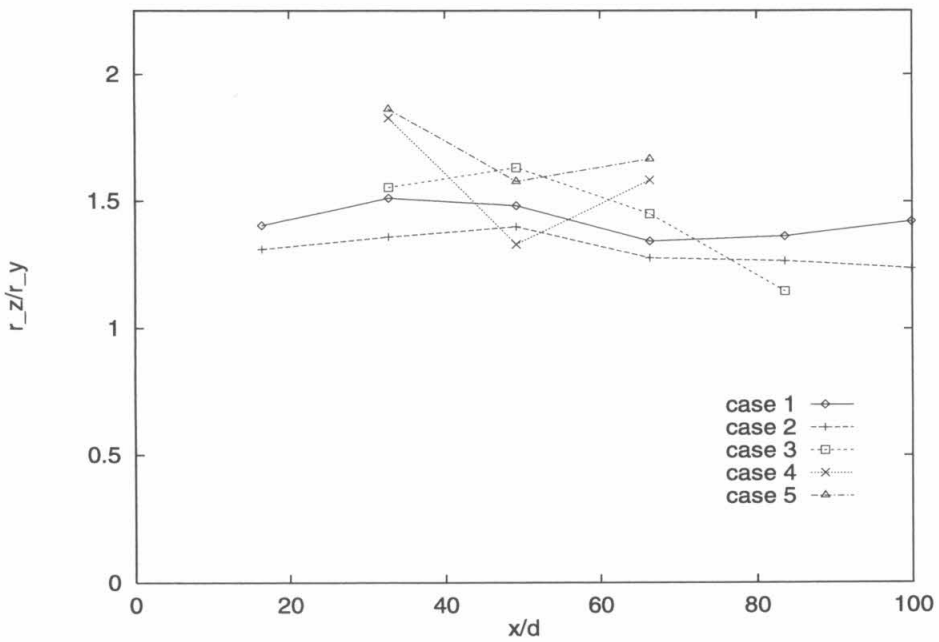

Figure 5.6 Jet aspect ratio from pitot pressure data

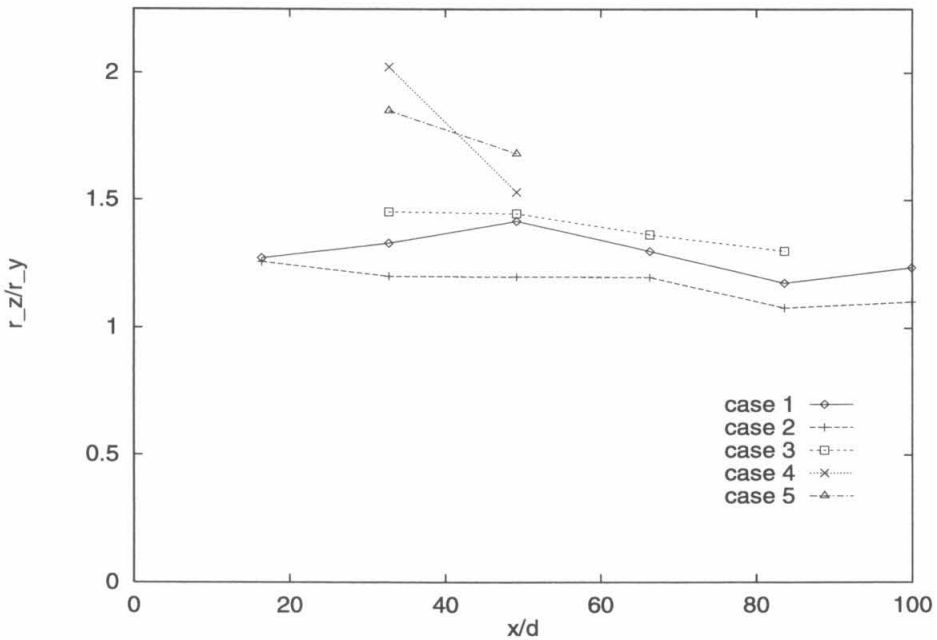

Figure 5.7 Jet aspect ratio from recovery temperature data

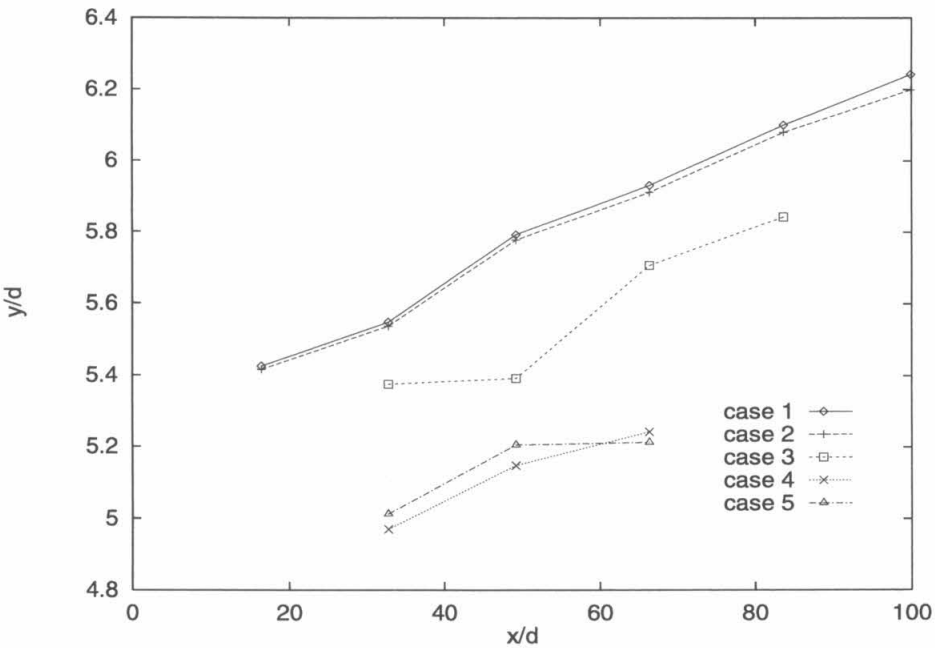

Figure 5.8 Jet height above tunnel wall from pitot pressure data

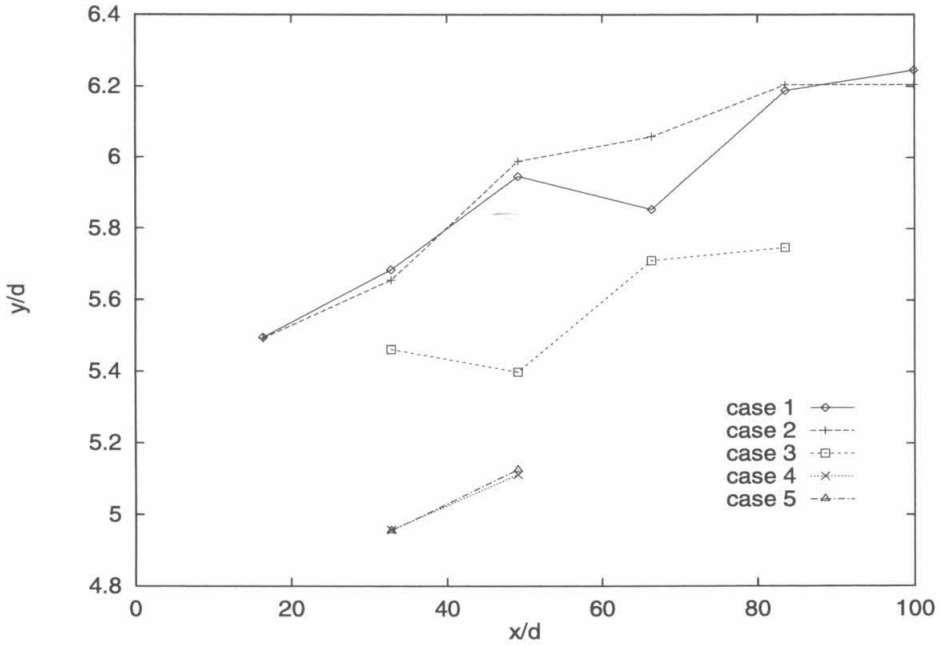

Figure 5.9 Jet height above tunnel wall from recovery temperature data

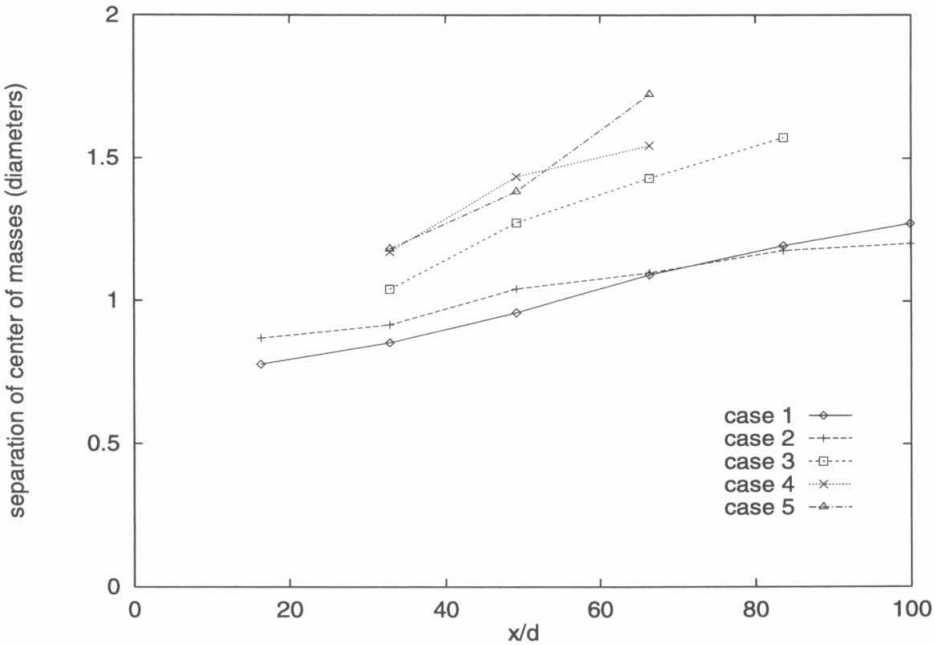

Figure 5.10 Jet width from pitot pressure data

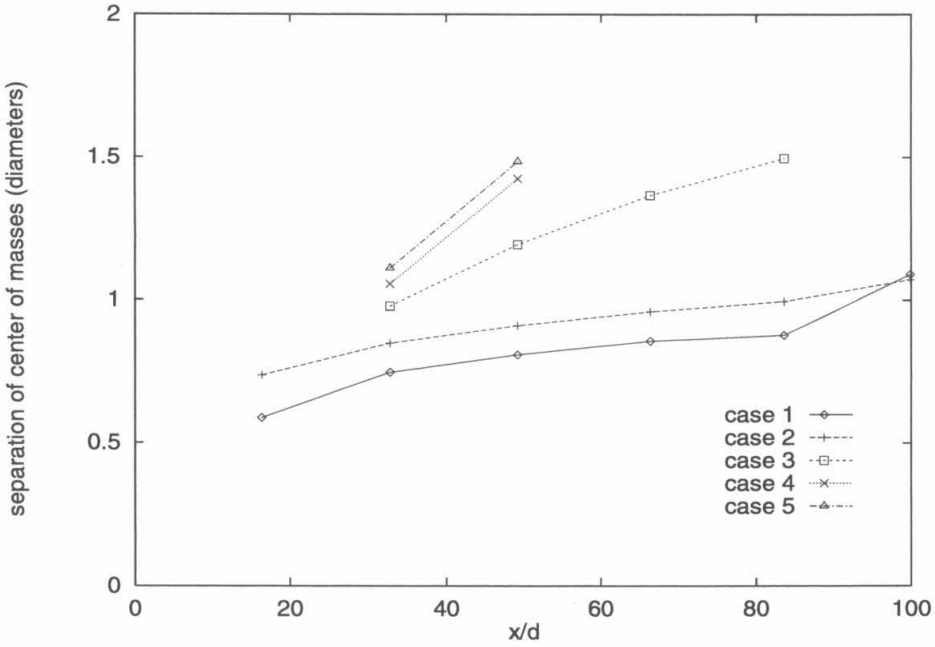

Figure 5.11 Jet width from recovery temperature data

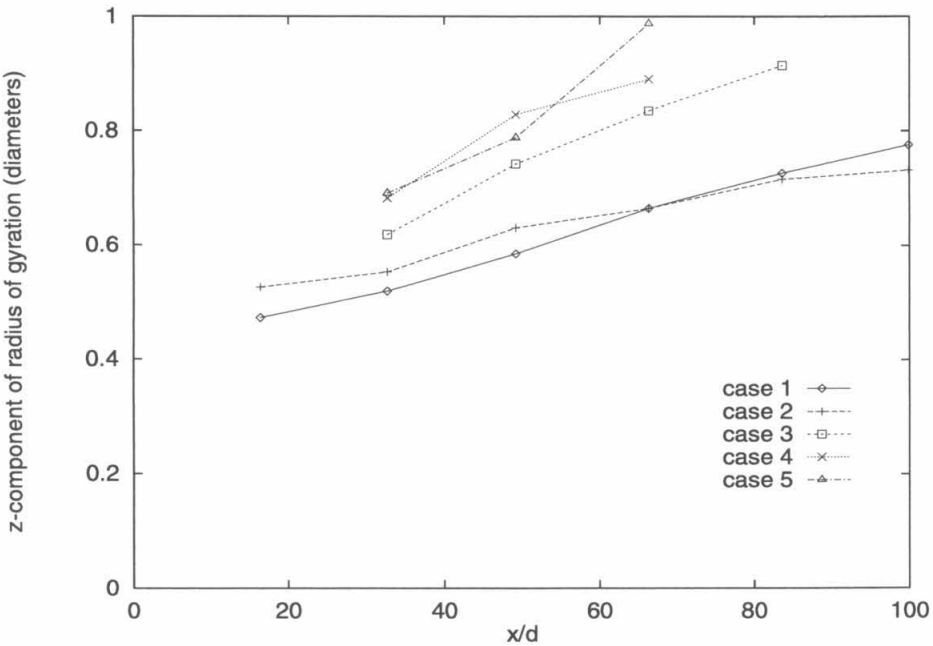

Figure 5.12 Horizontal component of jet radius from pitot pressure data

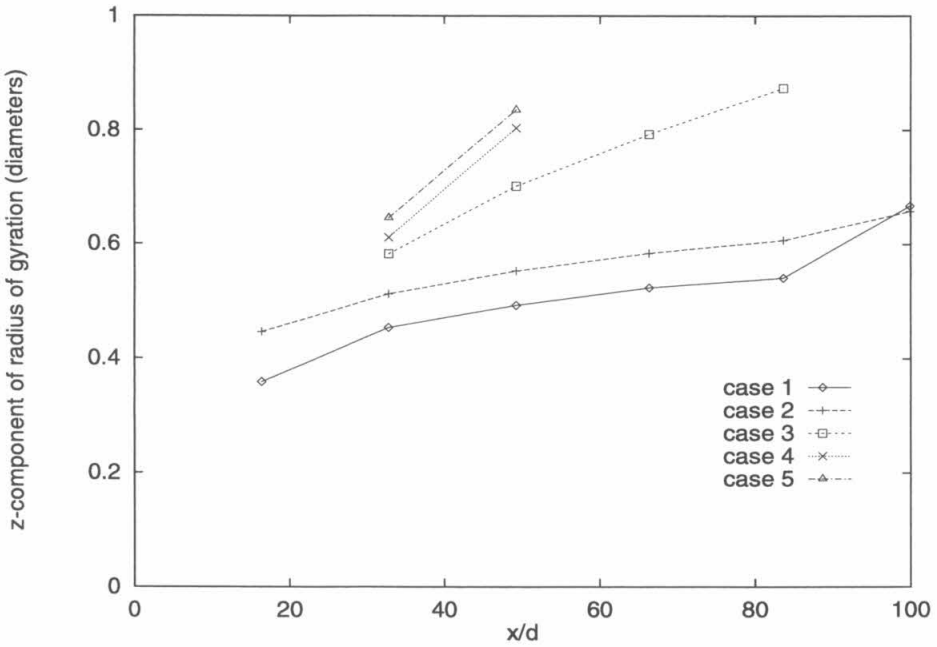

Figure 5.13 Horizontal component of jet radius from recovery temperature data

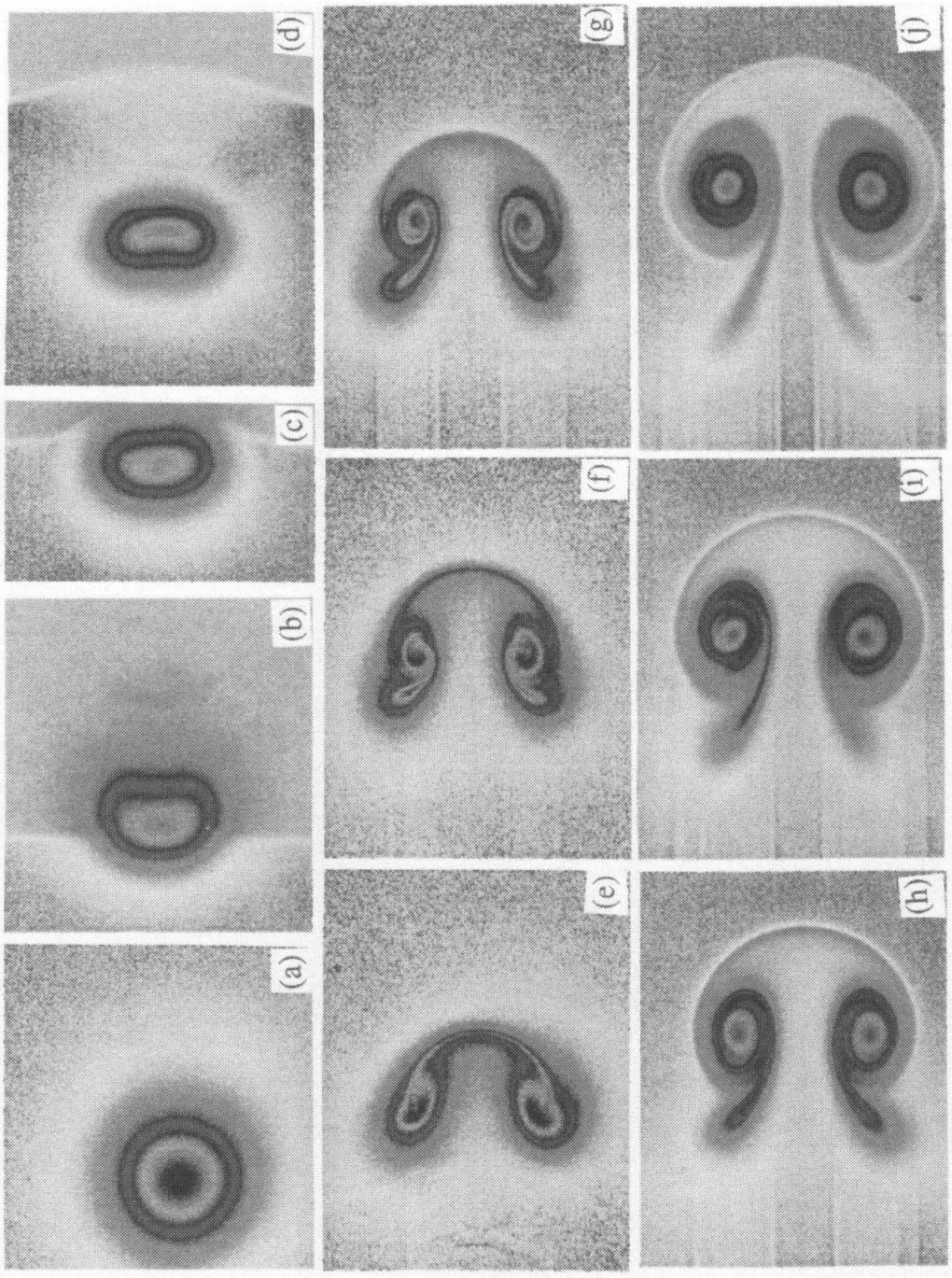

Figure 5.14 Series of Rayleigh scattered images from Budzinski's thesis

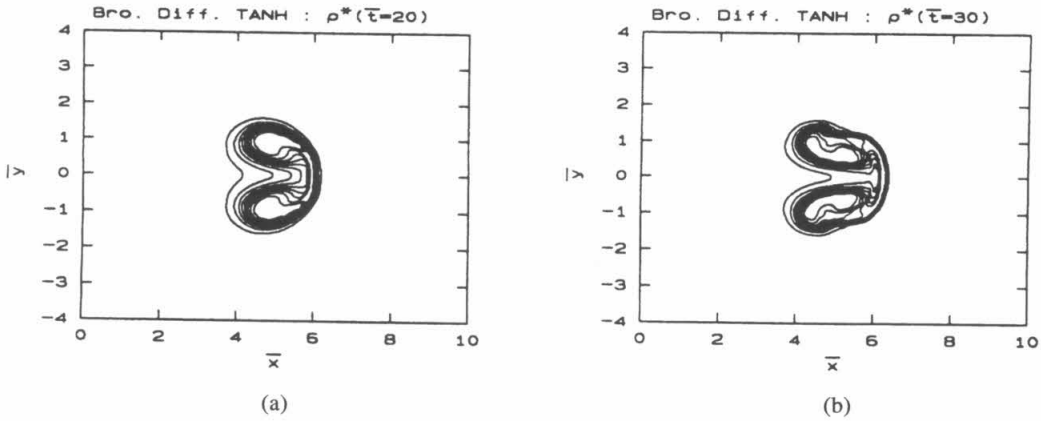

Figure 5.15 Figure from Yang's thesis showing his calculations at t/τ=9.6 (a) and t/τ=14.5 (b)

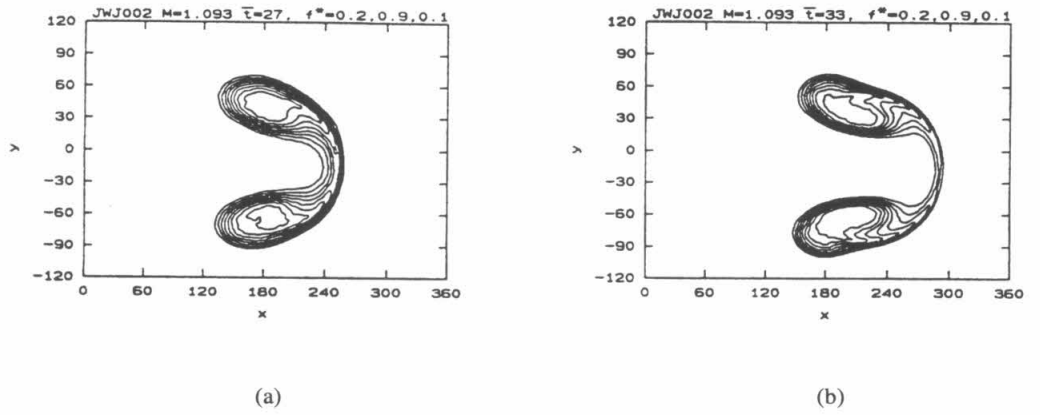

Figure 5.16 Figure from Yang's thesis showing Jacobs' data at t/τ=11.8 (a) and t/τ=14.4 (b)

Chapter 6

Discussion and Conclusions

Experiments on the steady three-dimensional interaction of a coflowing light gas jet with a weak oblique shock wave were performed. Planar Rayleigh scattering of a laser light sheet off of the ice crystals present in the freestream was used to get time resolved flow visualization of the jet cross sections, and time averaged cross sectional views of the jet were obtained through pitot pressure and temperature surveys of the flowfield.

The three-dimensional aspects of these experiments, along with the turbulent nature of the light gas jet, gave rise to additional complications not present in the two-dimensional studies. The oblique shock had a pressure gradient with a component parallel to the freestream; this made it impossible for the three-dimensional problem to have no shear between the jet and the freestream both up- and downstream of the shock wave. In contrast, the two-dimensional studies performed in the past have not had any appreciable shear between the jet and the surrounding medium.

In the mean, the shear between the jet and the freestream did not appear to have a large effect on the post-shock development of the flow. The shape and structure of the pressure and temperature cross sections from these experiments agreed well with the shape and structure of corresponding cross sections from two-dimensional experiments and calculations.

The two-dimensional model appears to give a good representation of the mean

three-dimensional flow. In a time averaged sense, the predictions of increased mixing due to the presence of the shock should be extensible from the two-dimensional to the three-dimensional case. However, the light scattered images taken in these experiments produced qualitative time-resolved information showing significant temporal variation from the mean flow.

The experiments which have been presented here did not extend into non-dimensional time scales where previous two-dimensional studies predicted the formation of relatively large tail lobes extending from the vortex pair. It is possible that shear between the jet and freestream in the three-dimensional case may prevent the formation of these tails. If so, this would have an effect on the mixing predictions made by investigators of the two-dimensional flow. They noted that the light gas vortices tended be self stabilizing and that much of the mixing after the formation of the tail regions occurred in the tails. The rapid shearing off of these tails in the three dimensional case could increase the mixing rate over that predicted by two-dimensional studies.

The summary plots of the time averaged data consistently showed the jet size increasing with shock strength. Also, the data in plots of various measurements of the jet size and position were consistently grouped according to shock strength. Thus, it was concluded that for the different velocity ratios studied, the variation in flow development from case to case due to changes in shear was minor compared to the effect of changes in shock strength.

Qualitatively, when comparing Rayleigh scattered images taken at the same distance from the jet exit the jet's structure is seen to be less regular for the shock interaction case. This, along with the increase in jet area shown by the same pictures for the shock interaction case, indicates that the presence of the shock wave has enhanced mixing in a time resolved sense.

Appendix A

Helium Injection and Temperature Control

A long narrow length of tubing was needed to deliver the helium through the nozzle with a minimum of disturbance to the flow external to the injector (refer to Figure 2.1). The injector itself was a thin-walled 6 gage (inner diameter 4.65 mm, outer diameter 5.16 mm) tube inside of a 6.35 mm outside diameter thin-walled tube (see Figure A.1). The total length of the 4.65 mm diameter tube was 900 mm.

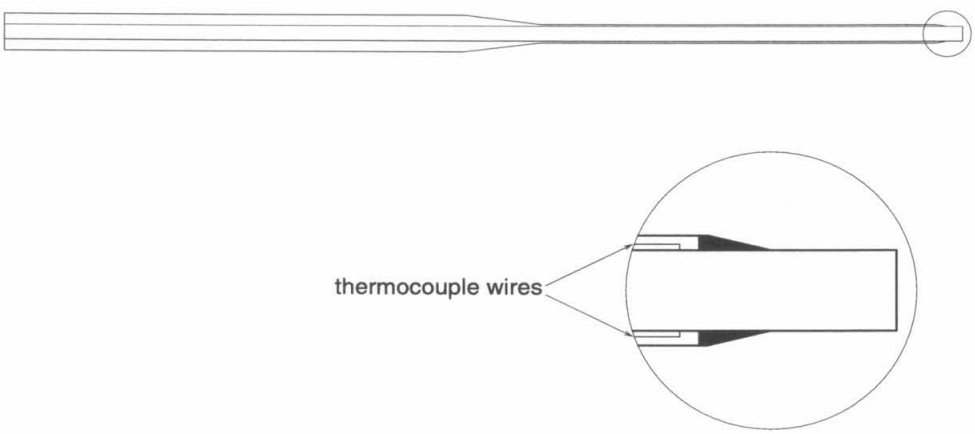

Figure A.1 Injector diagram

All references to the jet exit diameter are based upon the 4.65 mm inner diameter of the inner tube. A vacuum was maintained between the two tubes in order to minimize heat exchange between the helium and the air upstream of the injector

exit.

Two pairs of thermocouple wires were fed between the inner and outer tubes to near the injector exit, where they were silver-soldered to the outside of the inner tube. They provided temperature feedback to the system controlling the helium injection. A small conical section was silver soldered between the inner and outer tubes near the injector exit to provide a seal on that end, and a 1.5 diameter long extension to the inner tube was soft soldered onto the end to minimize the influence on the flow due to the presence of the conical section.

The other end of the inner tube was silver soldered to a 127 mm diameter fitting. This fitting was sealed with a Cajon connector (see Figure A.2). On the other end of the Cajon connector was a Swagelock connector which was sealed to the outer tube, which also had been increased to 127 mm outer diameter. The o-ring seal of the Cajon connector allowed for a change in relative lengths of the inner and outer tubes without losing the vacuum between them. This was needed to accommodate the thermal contraction difference present between the inner and outer tubes during operation of the injector.

Figure A.2 is a photo showing the upstream end of the disassembled injector.

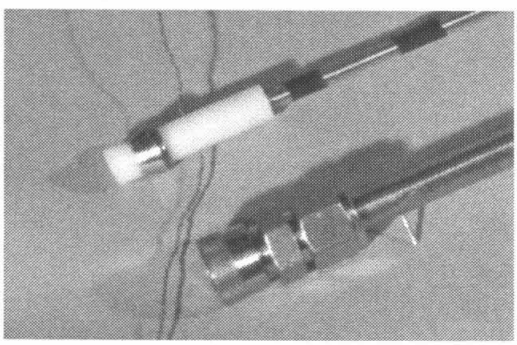

Figure A.2 Photo of disassembled injector

The white portion of the top piece is the fitting on the end of the inner tube. When the top tube was placed inside of the bottom tube the o-ring in the Cajon connector on the end of the bottom tube sealed against this fitting. It was originally made

of delrin and attached to the inner tube using low temperature rtv silicone (as depicted in the photo). It was later changed to stainless steel and silver soldered to the inner tube. This modification was made to correct for a leak in the metal to plastic joint which manifested itself when the injector assembly was subjected to low temperatures. The black bands on the top piece are a heat shrink material which was used to hold the thermocouple wire against the inner tube. The twisted thermocouple wire pairs can be seen coming out of the delrin fitting. After the delrin fitting was replaced by stainless steel the thermocouple wires were fed through tabulations mounted to the outer tube (the one used to pull the vacuum between the tubes can be seen protruding out of the bottom tube in Figure A.2). A length of insulation was stripped from every wire just past the tabulation, and a tygon tube was put over it. The gap between the tygon tube and the bare thermocouple wire was then filled with rtv silicone to complete the seal.

For all test cases in this investigation the flow at the exit of the injector was supersonic on the centerline but fell to subsonic toward the edge, as is consistent with compressible, non-adiabatic flow through a constant area duct [12]. Calculation of the jet exit Reynolds numbers shows that the jet was also turbulent for all test cases (see Table 2.1).

A.1 Measurement of the Jet Exit Conditions

A static pressure of 5780 Pa was used for calculations at the jet exit. Knowledge of the pressure and temperature at the jet exit allowed calculation of the velocity, density, and Mach number across the jet.

Figure A.3 shows the velocity at the jet exit when the helium mass flowrate was set to 50 slpm and the wall temperature near the injector exit was held at 210K. Figure A.4 shows the velocity at the jet exit when the helium mass flowrate was set to 92.7 slpm and the wall temperature near the injector exit was held at 210K.

The pitot probe and temperature probe were traversed across the jet within 0.1 diameters of the injector exit. Schlieren photos of the jet exit supported the

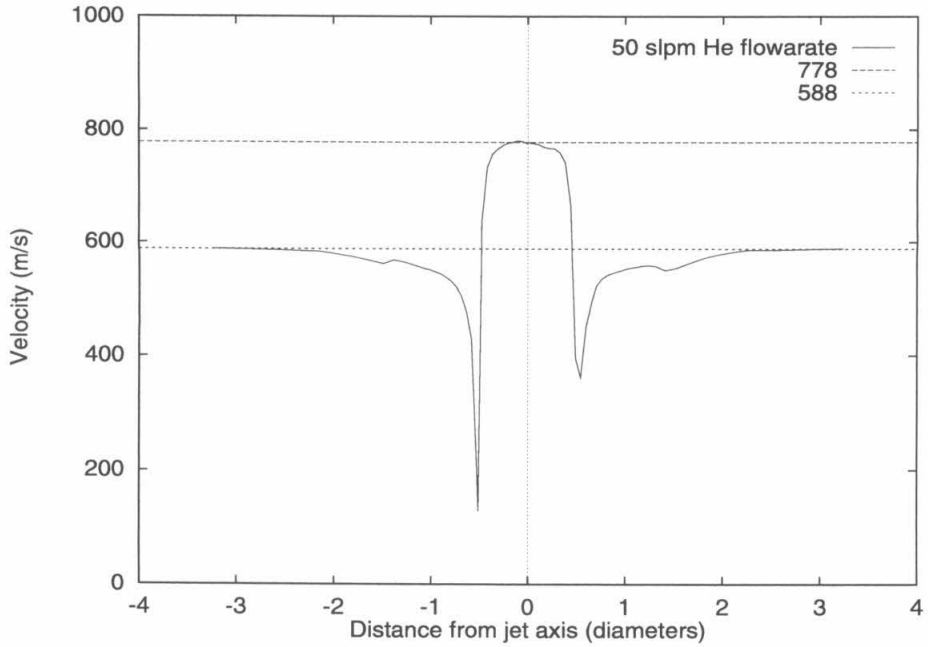

Figure A.3 Velocity across jet exit for 50 slpm He mass flowrate

assumption that the static pressure of the jet was matched with freestream. The large difference in stagnation pressure between the jet and freestream made it likely that fluid was being pumped along the thermocouple wire from the freestream into the jet region. This effect was minimized at the center of the jet, so the summary of jet exit conditions shown in Table 2.1 contains numbers based on readings taken on the jet centerline.

A.2 A Control Model for the Helium Injection System

A diagram of the main components of the injection system is shown in Figure A.5. The entire apparatus acts as a gas blending system which controls the temperature and mass flowrate of the gas coming out of the injector. High pressure helium from the gas bottles passes through a pressure regulator and filter to two mass flow controllers. The helium that goes through one controller continues on into

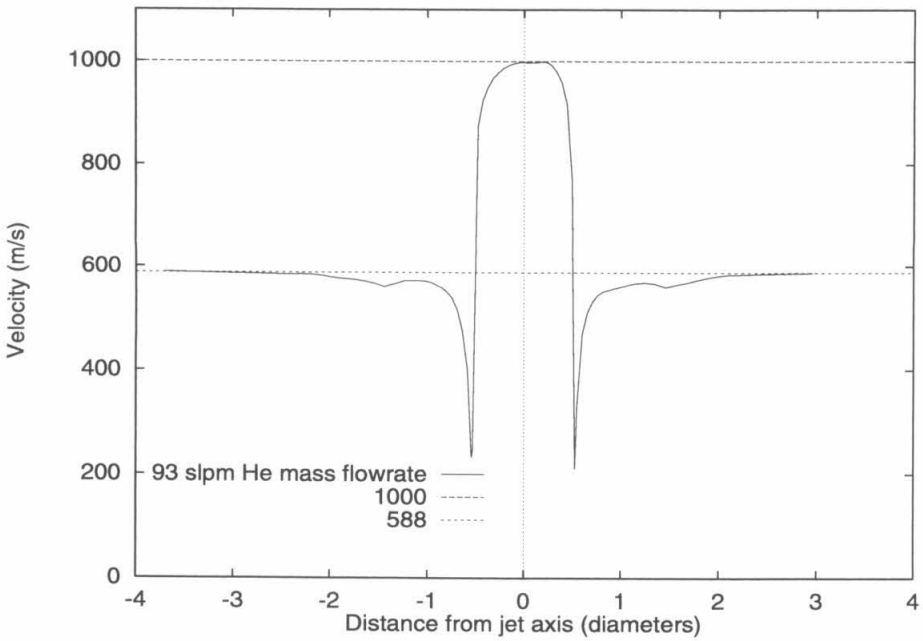

Figure A.4 Velocity across jet exit for 93 slpm He mass flowrate

the injector, while the helium that goes through the other controller goes through a liquid nitrogen bath before entering the injector. The relatively long (approximately 2 meter) length of tubing the helium passes through before the injector exit ensures that the two streams are well mixed. The thermocouples near the end of the injector provide feedback to a computer which controls the relative amount of helium from each mass flow controller.

A simple block diagram used in the development of the temperature control system is shown in Figure A.6 where $T_s(t)$ is the set temperature, $e(t)$ the error signal, $p(t)$ the change in temperature, $H_c(s)$ the transfer function of the control system, $H_p(s)$ the transfer function of the injector system, $L(t)$ the external load, and $T_p(t)$ the process temperature. The objective in designing the control system was to have $T_p(t)$ track $T_s(t)$ as quickly and accurately as possible. A standard PID controller was found inadequate for this task, so an effort to model the injector was made in the hope of constructing a better performing control system.

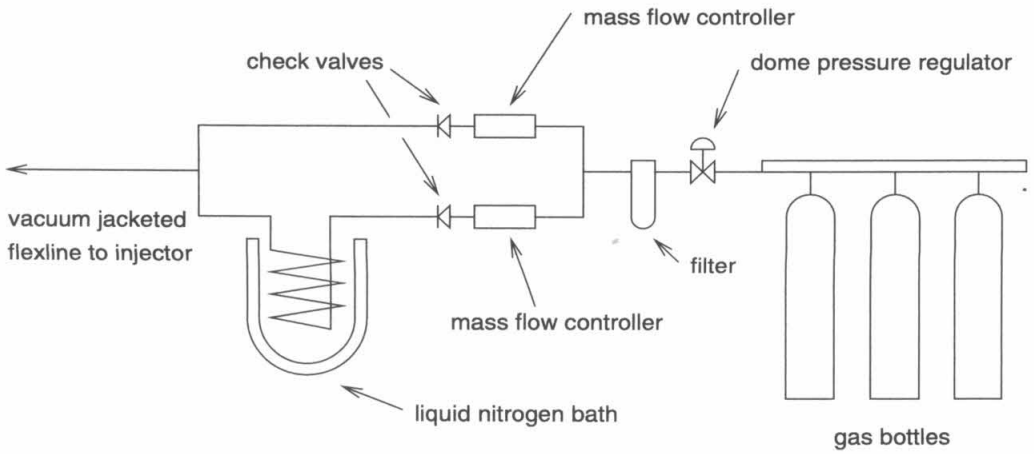

Figure A.5 Injection system schematic

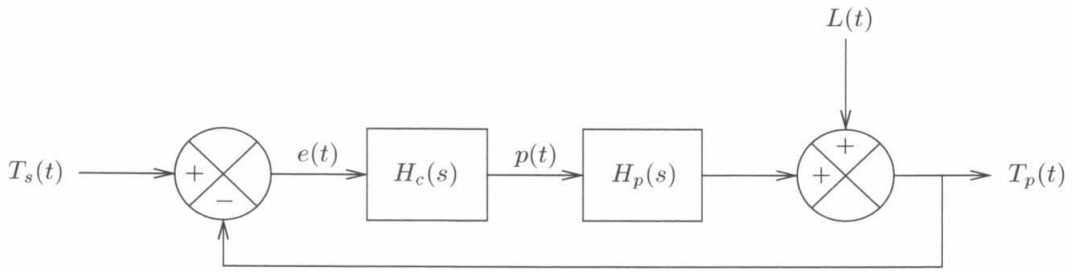

Figure A.6 Control system block diagram

The transfer function for the injector system in this model lumps together the thermal properties of the injector tubing and flowing gas with the response characteristics of the mass flow controllers feeding the injector, the temperature feedback system, and the computer receiving temperature data and sending commands to the mass flow controllers. The problem of determining an analytic representation of $H_p(s)$ is simplified by assuming that the response times of the mass flow controllers, thermocouples used for temperature feedback, and the computer are all *small* compared with that of the injector tubing.

There is approximately 100 cm of 9.5 mm diameter tubing from the point at

which the streams from both mass flow controllers meet to the entrance of the narrow injection tube. The narrow injection tube is approximately 91 cm long and 4.65 mm in diameter. Thus, the total volume of the injector tubing is 0.086 liters. The two mass flowrates used in these experiments were 50 slpm and 92.7 slpm. Assuming the injectants are at standard temperature and pressure these flowrates result in residence times of approximately 0.10 and 0.056 seconds, respectively. No attempt was made to measure the properties of the helium while it was in the injector, but knowledge of the lower limit of the inlet temperature (77 K) and upper limit of the inlet pressure (4 atmospheres) gives a maximum density of 14 times that at stp. Multiplying the residence times by 14 results in a maximum of 1.4 seconds, which is still insignificant.

The dominating factor in the response of the entire injector system is the time it takes for thermal energy to flow through the injector. The temperature of the helium at the exit changes very slowly in response to a change in the temperature of the helium at the entrance. The response curves in Figure A.8 show open loop response times on the order of 10 to 20 minutes. This is due to the thermal mass of the injector and the excellent thermal contact between the helium and the injector tubing.

These observations lead to the conclusion that the helium injector can be described as a distributed parameter system where the time associated with energy transport is orders of magnitude larger than the time associated with the flow of helium through the injector. Seborg, Edgar, and Mellichamp ([24], page 153) state:

> An overdamped response, sometimes with a right-half plane zero, often is observed experimentally for distributed reaction processes. Hence, a general empirical model of the form
>
> $$G(s) = \frac{K(\tau_a s + 1)e^{-\theta s}}{(\tau_1 s + 1)(\tau_2 s + 1)} \qquad \text{(A.1)}$$
>
> may be appropriate for these systems.

In equation (A.1) τ_a, τ_1, and τ_2 are the time constants associated with the injection

system, while θ is a time delay associated with the transit time of fluid through the injector and K is the gain of the system. The residence time of the fluid in the injector calculated above is so small compared with the time constants that θ can safely be set to zero and the exponential term dropped from (A.1).

This results in the form of $H_p(s)$ proposed to model the injector system dynamics:

$$H_p(s) = \frac{K(\tau_3 s + 1)}{(\tau_1 s + 1)(\tau_2 s + 1)} \tag{A.2}$$

The time constants and gain in equation (A.2) can be determined by measuring the response of the injector system to a step input. The step response of the system is the inverse Laplace transform of

$$\frac{1}{s} H_p(s) = \frac{K(\tau_3 s + 1)}{s(\tau_1 s + 1)(\tau_2 s + 1)} \tag{A.3}$$

which is

$$u(t) = K\left(1 + \frac{\tau 3 - \tau 1}{\tau 1 - \tau 2} e^{-t/\tau 1} + \frac{\tau 3 - \tau 2}{\tau 2 - \tau 1} e^{-t/\tau 2}\right) \tag{A.4}$$

The time constants of the system were determined by fitting equation (A.4) to the square wave response of the system. A sample square wave input file is shown in Figure A.7 for the 50 slpm case. The response to this input as measured by the thermocouple on the wall near the injector exit is shown in Figure A.8. The only difference between the two curves in Figure A.8 is that one was taken during the first run of the day, when the injector started at room temperature, and the other was taken after the first run, when the injector was already cold. This demonstrates the nonlinear nature of the injection system. The response when the injector was warm was not used in fitting the linear model, since the tunnel was run most of the time with a pre-cooled injector.

The steady state offset between the input and output signals was unimportant in determining the values of K, τ_1, τ_2, and τ_3, so the temperature changes from each

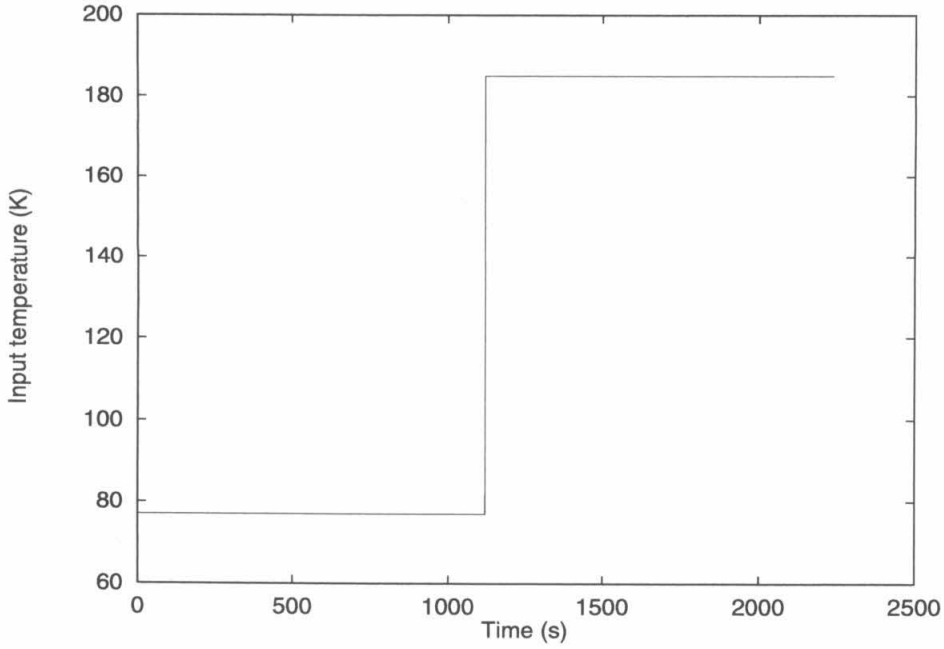

Figure A.7 Temperature commands input to injector

step were referenced from zero. Figure A.9 shows one section of the response curve from the second run along with a fit to the data. The constants derived from both 77K to 185K response curves were averaged to get the numbers used in the final 50 slpm model. A similar technique was used to obtain the model parameters for the 92.7 slpm flowrate.

The closed loop transfer function of the system in Figure A.6 is described by (for set point changes - see pages 231-233 of [24])

$$\frac{T_p(s)}{T_s(s)} = \frac{H_c(s)H_p(s)}{1 + H_c(s)H_p(s)} \tag{A.5}$$

Letting $\frac{T_p(s)}{T_s(s)} = \frac{1}{(\tau_c s+1)}$ so that the closed loop transfer function has a first-order response with a specified time constant, τ_c, results in

$$\frac{1}{(\tau_c s + 1)} = \frac{H_c(s)H_p(s)}{1 + H_c(s)H_p(s)} \tag{A.6}$$

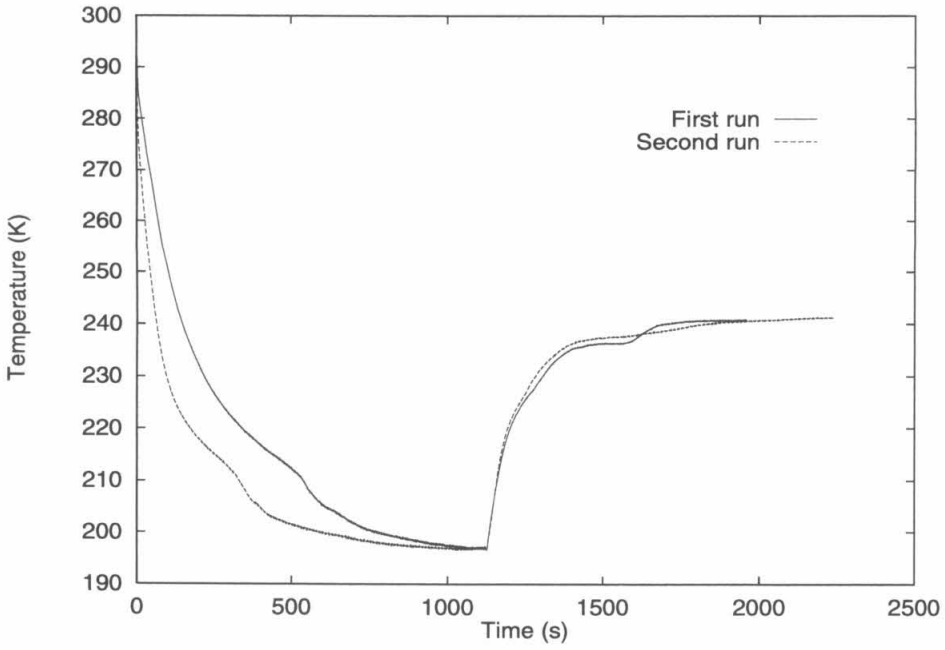

Figure A.8 Wall temperature near injector exit

Solving (A.6) for $H_c(s)$ and substituting for $H_p(s)$ results in the desired transfer function of the control system:

$$H_c(s) = \frac{(\tau_1 s + 1)(\tau_2 s + 1)}{K\tau_c s(\tau_3 s + 1)} \tag{A.7}$$

Substituting $\frac{P(s)}{E(s)}$ for $H_c(s)$ and rearranging the terms in (A.7) results in

$$\frac{P(s)}{E(s)} = \frac{(\tau_1 + \tau_2) + 1/s + \tau_1\tau_2 s}{K\tau_c(\tau_3 s + 1)} \tag{A.8}$$

which can be simplified using the new terms

$$K_c = \frac{\tau_1 + \tau_2}{K\tau_c} \qquad \tau_I = \tau_1 + \tau_2 \qquad \tau_D = \frac{\tau_1\tau_2}{\tau_1 + \tau_2} \tag{A.9}$$

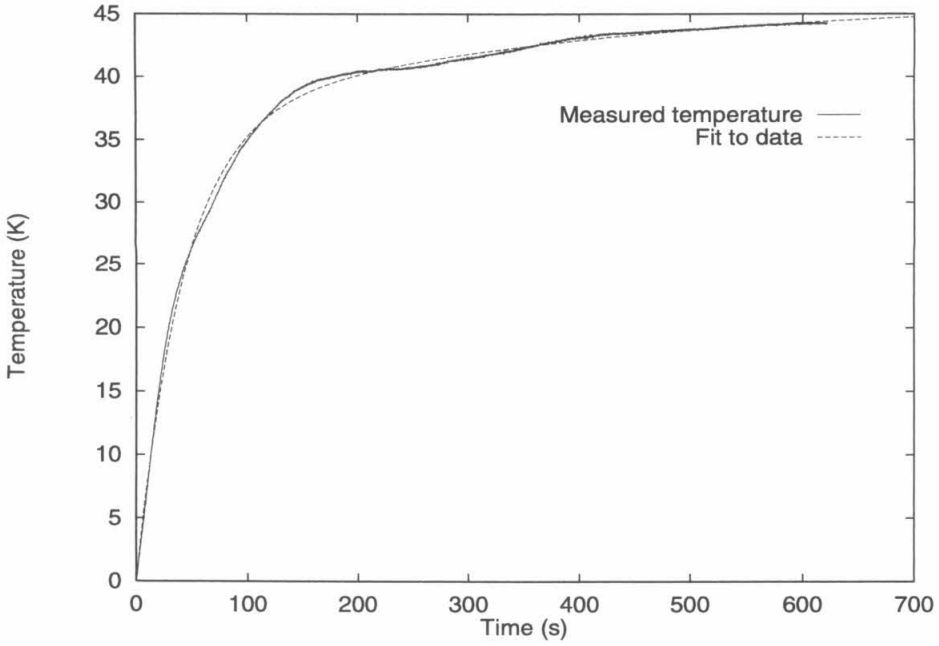

Figure A.9 Wall temperature response of injector to jump in input temperature from 77K to 185K

This results in

$$[\tau_3 s + 1]P(s) = K_c \left[1 + \frac{1}{\tau_I s} + \tau_D s\right] E(s) \tag{A.10}$$

which would be a standard PID controller if the term $[\tau_3 s + 1]$ was dropped. Equation (A.10) can be transformed to a discrete difference equation in the time domain:

$$\frac{\tau_3}{\Delta t}[p_n - p_{n-1}] + p_n = \overline{p} + K_c \left[e_n + \frac{\Delta t}{\tau_I} \sum_{k=1}^{n} e_k + \frac{\tau_D}{\Delta t}(e_n - e_{n-1})\right] \tag{A.11}$$

Substituting $(n-1)$ for n in (A.11), subtracting from (A.11), and solving for p_n

gives

$$p_n = \left[\frac{1}{\frac{\tau_3}{\Delta t}+1}\right]\left\{\left(1+\frac{2\tau_3}{\Delta t}\right)p_{n-1} - \frac{\tau_3}{\Delta t}p_{n-2} + K_c\left[(e_n - e_{n-1}) + \frac{\Delta t}{\tau_I}e_n + \frac{\tau_D}{\Delta t}(e_n - 2e_{n-1} + e_{n-2})\right]\right\} \quad \text{(A.12)}$$

This is the equation used by the "C"-language control program listed in A.3.

A sample of the closed loop response of the system is shown in Figure A.10. The

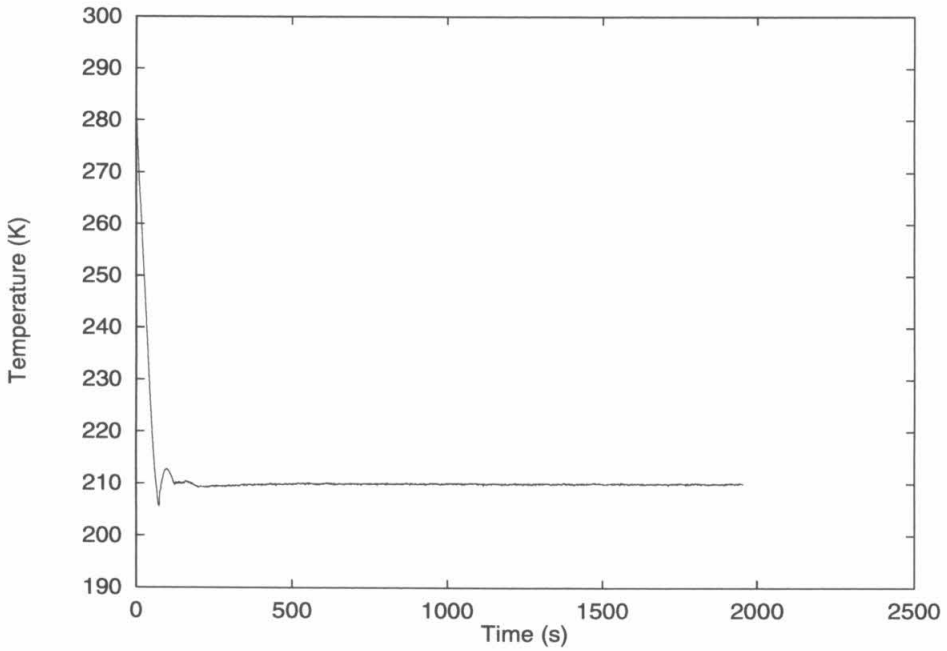

Figure A.10 Wall temperature of injector near the exit during a typical run at 50 slpm helium mass flowrate

mass flowrate was set at 50.0 slpm ($u_{He}/u_{air} = 1.25$ case), and the set temperature was 210 K. Data collection for this run began at the 450 second mark. After this point the maximum temperature recorded was 210.19 K, and the minimum temperature recorded was 209.7 K. Control of the injector temperature was typically within ± 0.3 K of the set point. The response for the 92.7 slpm mass flowrate cases was as good or better due to the shorter response time of the higher flowrate system.

A.3 Control Program Listing

```
/*
*  Program to control two mass flow controllers in a gas blending system
*  to get a desired output temperature.  A modified pid control algorithm
*  is used.  This program uses a temperature control variable - the desired
*  output temperature is known, and the input temperature to the injector
*  is controlled - mass flow rates are determined by knowing the output
*  temperatures of the two mass flow controllers.  Superior to the method
*  used in control.c - avoid it.
*/

/*
   Modified on 10-25-95 to limit the control temperature to the limits
   of the hardware.  This will prevent overshoots and shoot allow
   the control system to recover from large changes quickly.
   The variable involved is Tn.
*/


#include <stdio.h>
#include <\das20\include\daq.h>

/*
*   Declare variables of global scope - see program description for
*   definition of these variables.
*/

double Ms,Mt,Mc,Mcp,Mh,Mhp,en,en1,en2,Ts,Tp,Tn,Tmax,Tmin,xn,
       Mc_last=0.0,Mh_last=0.0,pn,pn1,pn2,Kc,taud,taui;
int mode,data[10],error=0,count=0,startup=1;
FILE *output;
/* Variables to be read in from config file */
double MAXMC, MAXMH, K, tau1, tau2, tau3, tauc, dt, alpha, THOT,
       TCOLD, MC_CHANGE, MH_CHANGE, MC_CORRECTION, MH_CORRECTION,
       MCOVER, MHOVER;


void data_in();
void init();
double black_box();
void mdot_output();
int display();
double Terror();

int main(int argc, char **argv) {
  int not_done,number,i;
  FILE *config_data;
  double Tqueue[10], mc_change, mh_change;

  if (argc!=2) {
```

```
    puts("Usage: pid <config file>");
    exit(1);
  }
  if ((config_data = fopen(argv[1],"r")) == NULL) {
    printf("Error opening config file %s.\n",argv[1]);
    exit(1);
  }
  fscanf(config_data,"%*s %lf", &MAXMC);
  fscanf(config_data,"%*s %lf", &MAXMH);
  fscanf(config_data,"%*s %lf", &K);
  fscanf(config_data,"%*s %lf", &tau1);
  fscanf(config_data,"%*s %lf", &tau2);
  fscanf(config_data,"%*s %lf", &tau3);
  fscanf(config_data,"%*s %lf", &tauc);
  fscanf(config_data,"%*s %lf", &dt);
  fscanf(config_data,"%*s %lf", &alpha);
  fscanf(config_data,"%*s %lf", &THOT);
  fscanf(config_data,"%*s %lf", &TCOLD);
  fscanf(config_data,"%*s %lf", &MC_CHANGE);
  fscanf(config_data,"%*s %lf", &MH_CHANGE);
  fscanf(config_data,"%*s %lf", &MC_CORRECTION);
  fscanf(config_data,"%*s %lf", &MH_CORRECTION);
  fscanf(config_data,"%*s %lf", &MCOVER);
  fscanf(config_data,"%*s %lf", &MHOVER);

  output = fopen("temp.dat","wt");

  pn=pn1=pn2=298.15;
  Tn=298.15;
  Kc=(tau1+tau2)/(K*tauc);
  taui=tau1+tau2;
  taud=tau1*tau2/(tau1+tau2);

/* Initialize the DAS20 */
  mode = 0;
  data[0] = ADDRESS;  /* DAS20 I/O Port */
  data[1] = INTRPT;   /* DAS20 Int */
  data[2] = DMA;      /* DAS20 DMA */
  if ((error = DAS20(mode,data)) != 0) {
    printf("\r\n Errror in initializing DAS20.  Error code: %d\r\n",error);
    exit(1);
  }
  data_in();
  init();
  not_done=1;
  while(not_done) {
    if (startup) {
      if ((Tp-Ts)<0.0) {
        Mt=Mt-0.5;
if (Mt<=Ms){ Mt=Ms; startup=0; }
        Tmax = (Mt>MAXMH*MHOVER) ?
```

```
                (THOT*MAXMH*MHOVER+TCOLD*(Mt-MAXMH*MHOVER))/Mt : THOT;
        Tmin = (Mt>MAXMC*MCOVER) ?
                (TCOLD*MAXMC*MCOVER+THOT*(Mt-MAXMC*MCOVER))/Mt : TCOLD;
      }
    }
    Tn=black_box();
    mdot_output();
    if ((not_done=display())==2) init();
  }
  mode=7;
  data[0]=0;
  data[1]=0;
  if ((error = DAS20(mode,data)) != 0) {
    clrscr();
    printf("\r\n Error in shutting down cold controller.  Error code: %d",
      error);
    exit(1);
  }
  mode=7;
  data[0]=1;
  data[1]=0;
  if ((error = DAS20(mode,data)) != 0) {
    clrscr();
    printf("\r\n Error in shutting down hot controller.  Error code: %d",
      error);
    exit(1);
  }
}

void data_in() {
  clrscr();
  gotoxy(4,2);
  printf("Enter the mass flowrate set point (in slpm): ");
  scanf("%lf",&Ms);
  printf("\nEnter the initialization mass flowrate (in slpm): ");
  scanf("%lf",&Mt);
  printf("\r\n\r\n   Enter the desired injector wall temperature: ");
  scanf("%lf",&Ts);
  Tmax = (Mt>MAXMH*MHOVER) ? (THOT*MAXMH*MHOVER+TCOLD*(Mt-MAXMH*MHOVER))/Mt
     : THOT;
  Tmin = (Mt>MAXMC*MCOVER) ? (TCOLD*MAXMC*MCOVER+THOT*(Mt-MAXMC*MCOVER))/Mt
     : TCOLD;
  pn=pn1=pn2=298.15;
  clrscr();
}

void init() {

  clrscr();
  gotoxy(4,2);
  puts("Current error:          K          Previous error:          K");
```

```
  gotoxy(4,4);
  puts("Temp setting:           K          Injector temp:            K");
  gotoxy(4,6);
  puts("Mt setting:             slm        e(n-2):                   K");
  gotoxy(4,8);
  puts("Mc setting:             slm        "
       "Mc Process:               slm");
  gotoxy(4,10);
  puts("Mh setting:             slm        "
       "Mh Process:               slm");
  gotoxy(4,12);
  puts("Count:                             Tn (T into inj):          K");
  gotoxy(4,20);
  puts("Enter:");
  puts("   q to quit, m to change Mt, or t to change Ts");
}

double black_box() {
/*************************************************************************
*   Handle all of the control math stuff
*************************************************************************/
  en2=en1;en1=en;
  pn2=pn1;pn1=pn;
  en = Terror();
/*  en = alpha*xn + (1-alpha)*en1; */
  pn=((1+2*tau3/dt)*pn1-tau3*pn2/dt+Kc*((en-en1)+dt*en/taui+
     taud*(en-2*en1+en2)/dt))/(tau3/dt+1);
  if (pn>Tmax) {pn=pn1=pn2=Tmax; en=en1=en2=0;}
  if (pn<Tmin) {pn=pn1=pn2=Tmin; en=en1=en2=0;}
  Tn = pn;
  return(Tn);
}

void mdot_output() {
/*************************************************************************
*   Send Mc and Mh to the analog outputs as appropriate.  Read in channel 0
*   first for the 5 volt reference.  Channel 0 uses 0-10V (gain code 0).
*   A delay (intentional 'sluggishness') is incorporated - the command to
*   the mass flow controllers will not change by more than 1% of the
*   full scale flow per time interval.
*************************************************************************/
/*************************************************************************
*   D/A channel 0 is cold, channel 1 is hot
*************************************************************************/

  int i,outc,outh;
  long int SAMPLES=50,outdata=0;
  double Mc_corrected,Mh_corrected,loadc,loadh,reference,Tnext,delta;

  mode=3;
  for (i=0; i < SAMPLES; i++) {
```

```
    data[0]=0;
    data[1]=0;
    if ((error = DAS20(mode,data)) != 0) {
      clrscr();
      printf("\r\n Error in reference voltage.  Error code: %d\r\n",
error);
      exit(1);
     }
     outdata += data[0];
  }
  reference = (double)outdata/SAMPLES;
  Tnext=Tn;
  if (Tnext>Tmax) Tnext=Tmax;
  if (Tnext<Tmin) Tnext=Tmin;
  Mc=(Tnext-THOT)*Mt/(TCOLD-THOT);
  Mh=(Tnext-TCOLD)*Mt/(THOT-TCOLD);

/*
  Correct Mc for leaky mass flow controller: subtract MC_CORRECTION from
  Mc, but be sure that Mc >= 0.0.  Also correct Mh in the same way.
*/
  Mc_corrected = Mc + MC_CORRECTION;
  if (Mc_corrected < 0.0) Mc_corrected = 0.0;
  if (Mc_corrected > MAXMC*MCOVER) Mc_corrected = MAXMC*MCOVER;
  Mh_corrected = Mh + MH_CORRECTION;
  if (Mh_corrected < 0.0) Mh_corrected = 0.0;
  if (Mh_corrected > MAXMH*MHOVER) Mh_corrected = MAXMH*MHOVER;
  delta=(Mc_corrected-Mc_last)/MAXMC;
  if (delta>MC_CHANGE) Mc_corrected=Mc_last+MC_CHANGE*MAXMC;
  if (delta<-MC_CHANGE) Mc_corrected=Mc_last-MC_CHANGE*MAXMC;
  delta=(Mh_corrected-Mh_last)/MAXMH;
  if (delta>MH_CHANGE) Mh_corrected=Mh_last+MH_CHANGE*MAXMH;
  if (delta<-MH_CHANGE) Mh_corrected=Mh_last-MH_CHANGE*MAXMH;
  loadc=Mc_corrected/MAXMC;
  loadh=Mh_corrected/MAXMH;
  outc=loadc*reference+0.5000001;
  outh=loadh*reference+0.5000001;
  Mc_last=Mc_corrected;
  Mh_last=Mh_corrected;
  gotoxy(2,23);
  printf("Mc_last: %lf   Mh_last: %lf ",Mc_last,Mh_last);
/*************************************************************************
First the mass flow controller for the cold He. (channel 0).
*************************************************************************/
  mode=7;
  data[0]=0;
  data[1]=outc;
  if ((error = DAS20(mode,data)) != 0) {
    clrscr();
    printf("\r\n Error controlling Mc.  Error code: %d\r\n",error);
    exit(1);
```

```
  }
/*************************************************************************
Second, the mass flow controller for the hot He. (channel 1).
*************************************************************************/
  mode=7;
  data[0]=1;
  data[1]=outh;
  if ((error = DAS20(mode,data)) != 0) {
    clrscr();
    printf("\r\n Error controlling Mh.  Error code: %d\r\n",error);
  }
}

int display() {
  int i,keypress=0;
  long int SAMPLES=50,outdata=0;
  double reference;

/*************************************************************************
First, get reference voltage.
*************************************************************************/
  mode=3;
  for (i=0; i < SAMPLES; i++) {
    data[0]=0;
    data[1]=0;
    if ((error = DAS20(mode,data)) != 0) {
      clrscr();
      printf("\r\n Error in reference voltage.  Error code: %d\r\n",
error);
      exit(1);
     }
     outdata += data[0];
  }
  reference = (double)outdata/SAMPLES;

/*************************************************************************
Second, get the measured Mc. (channel 2).
*************************************************************************/
  outdata=0;
  mode=3;
  for (i=0;i<SAMPLES;i++) {
    data[0]=0;
    data[1]=2;
    if ((error = DAS20(mode,data)) != 0) {
      clrscr();
      printf("\r\n Error in Mcp reading.  Error code: %d\r\n",error);
      exit(1);
    }
    outdata += data[0];
  }
  Mcp=(((double)outdata/SAMPLES)/reference)*MAXMC;
```

```
/*************************************************************************
Third, get the measured Mh.  (channel 3).
*************************************************************************/
  outdata=0;
  mode=3;
  for (i=0;i<SAMPLES;i++) {
    data[0]=0;
    data[1]=3;
    if ((error = DAS20(mode,data)) != 0) {
      clrscr();
      printf("\r\n Error in Mch reading.  Error code: %d\r\n",error);
      exit(1);
    }
    outdata += data[0];
  }
  Mhp=(((double)outdata/SAMPLES)/reference)*MAXMH;

/*************************************************************************
Now print out the info.
*************************************************************************/

  gotoxy(23,2);
  printf("%7.3lf",en);
  gotoxy(61,2);
  printf("%7.3lf",en1);
  gotoxy(23,4);
  printf("%5.1lf",Ts);
  gotoxy(61,4);
  printf("%5.1lf",Tp);
  gotoxy(23,6);
  printf("%6.2lf",Mt);
  gotoxy(56,6);
  printf("%7.3lf",en2);
  gotoxy(23,8);
  printf("%6.2lf",Mc_last);
  gotoxy(61,8);
  printf("%6.2lf",Mcp);
  gotoxy(23,10);
  printf("%6.2lf",Mh_last);
  gotoxy(61,10);
  printf("%6.2lf",Mhp);
  gotoxy(23,12);
  printf("%5d", ++count);
  gotoxy(61,12);
  printf("%6.2lf",Tn);
  fprintf(output,"%5d  %6.2lf  %6.2lf  %6.2lf  %6.3lf  %6.3lf  %6.3lf"
          "  %6.2lf\n", count,Tp,Mcp,Mhp,pn,pn1,pn2,Tn);
  gotoxy(4,20);
  puts("Enter:");
  puts("   q to quit, m to change Mt, or t to change Ts");
  keypress = NULL;
```

```
  if (kbhit()) keypress = getch();
  if (keypress == 'q' || keypress == 'Q') return(0);
  if (keypress == 'm' || keypress == 'M') {
    gotoxy(4,20);
    clreol();
    gotoxy(4,21);
    clreol();
    printf("Enter the new mass flowrate: ");
    scanf("%lf",&Mt);
    Tmax = (Mt>MAXMH*MHOVER) ?
           (THOT*MAXMH*MHOVER+TCOLD*(Mt-MAXMH*MHOVER))/Mt : THOT;
    Tmin = (Mt>MAXMC*MCOVER) ?
           (TCOLD*MAXMC*MCOVER+THOT*(Mt-MAXMC*MCOVER))/Mt : TCOLD;
    return(2);
  }
  if (keypress == 't' || keypress == 'T') {
    gotoxy(4,20);
    clreol();
    gotoxy(4,21);
    clreol();
    printf("Enter the new Ts: ");
    scanf("%lf",&Ts);
    return(2);
  }
  return (1);
}



double Terror() {
/* Get xn=Ts-Tp, which means getting Tp.  Using type T thermocouples in
   the injector tip, so typet is called.
*/
  int i;
  long int SAMPLES=500,outdata=0;
  double avrdata,millivolts;

/* Using channel 1 to get temp data.  Gain 3 is used (range +/-5 V).
*/
   mode=3;
   for (i=0; i < SAMPLES; i++) {
     data[0]=3;
     data[1]=1;
     if ((error = DAS20(mode,data)) != 0) {
       clrscr();
       printf("\r\n Error in temperature collection.  Error code: %d\r\n",
 error);
       exit(1);
     }
     outdata += data[0];
   }
```

```
    avrdata = (double)outdata/SAMPLES;
    millivolts = avrdata * SCALE;
    Tp = typet(millivolts);
    return (Ts-Tp);
}
```

Appendix B

Data Reduction of the Planar Rayleigh Scattered Images

A total of 40 different sets of Rayleigh scattered pictures were taken during this study. Most of them contained 30 data frames and several additional alignment and background frames. With over 1200 pictures to look at it became advantageous to automate the process of data reduction as much as possible. This Appendix describes some of the theoretical considerations involved in analysis of the scattered light images, discusses ice crystal size measurements, and gives, using one specific frame as an example, a step-by-step description of how the data from the Rayleigh scattered measurements was reduced.

B.1 Theoretical Calculation of Scattering Intensity

The scattering intensity depends on the scatterer size, wavelength and polarization of light being scattered, and other variables. Eckbreth [7] derived a formula for the number of photons per pixel collected by an imaging array

$$NPP = \frac{E_p N}{h\nu} \sigma_m \epsilon' \frac{\pi s}{4\eta^2} \frac{M}{(M+1)^2} \frac{1}{f} \tag{B.1}$$

The nomenclature for this formula is listed in Table B.1. All of the parameters on the right-hand side of (B.1) are known constants or determined by the experimental setup except for N and σ_m. The number density depends on the total amount of

NPP	:	number of photons per pixel
E_p	:	energy in the light pulse
N	:	number density of scatterers
h	:	Planck's constant
ν	:	frequency of incident beam
σ_m	:	differential (angular) scattering cross section
ϵ'	:	collection efficiency
s	:	side length of (square) detector array
η^2	:	number of detectors in array
M	:	magnification
f	:	f-number of collection optics

Table B.1 Nomenclature used in Equation (B.1)

material and the radii of the particles, and the cross section of the scatterers depends on their radii and material composition (in this case ice).

Previous studies have measured ice crystal sizes on the order of 100 Å [27] [25]. This is small compared with the 480 nm wavelength of the laser light, so the scattering of the laser light off of the ice crystals was in the Rayleigh regime ([28], page 75). The angular scattering cross section for unpolarized light in this case is given by ([19], page 194):

$$\sigma_m(\theta) = \frac{8\pi^4 r^6}{\lambda^4} \left(\frac{n^2 - 1}{n^2 + 2} \right)^2 (1 + \cos^2 \theta) \tag{B.2}$$

Here r is the size of the scattering particle, θ is the angle between the direction of the incident light and the observation direction, λ is the wavelength of the light, and n is the index of refraction of the scattering particle. The term $(1+\cos^2\theta)$ reflects the assumption of unpolarized light. For light polarized perpendicular to the plane of scattering the $\cos^2\theta$ term drops and only the 1 remains. For light polarized parallel to the plane of scattering the opposite is true; the 1 drops and the $\cos^2\theta$ remains.

The prism tuner in the dye laser used in these experiments polarized the light produced by the laser, and a half-wave plate was used to make the polarization vector of the main component of the laser light perpendicular to the plane of scattering.

The high gain of the dye laser (the front reflector of the lasing cavity was only 60% reflective) meant that the polarization of the beam would not be complete, and it was expected that the scattering cross section would have some small dependence on θ due to this.

B.2 Ice Crystal Size

The use of equations (B.1) and (B.2) along with measurements of the energy output by the dye laser and the amount of humidity in the lab air made it possible to get estimates for an average size of the ice crystals in the test section. The number density and average radius of the ice crystals were constrained by the fact that the total number density of water molecules in the air was fixed. After substituting (B.2) into (B.1), there were two equations, (B.1) and the volume to number density relation

$$N\left(\rho_{ice}\frac{4}{3}\pi r^3\right) = \rho_{H_2O/air} \tag{B.3}$$

with two unknowns, N and r. The term $\rho_{H_2O/air}$ refers to the density of water in the air mixture (kg of water per cubic meter of air). The term ρ_{ice} refers to the density of ice (approximately 1000 kg/m^3).

A vertical slice one pixel wide from a ccd picture is shown in Figure B.1. The data from the ccd camera is expressed adu's, or analog-to-digital units, for each pixel. For all of the experiments in this study the gain of the camera was set so that there were 50 electrons per adu. With a net collection efficiency of 0.25 (including interstitial spacing between the active elements) the number of photons per adu was 200. The region of zero intensity shown in rows 0 through 15 of Figure B.1 is an artifact of the data reduction process (see Section B.3). The laser beam approximately begins at row 35 and ends at row 535. The intensity falls off to approximately 15 adu's outside of the beam. The 15 adu background is due to diffuse scattering off of the various parts of the wind tunnel.

After subtracting the background the average intensity in the beam of Figure B.1

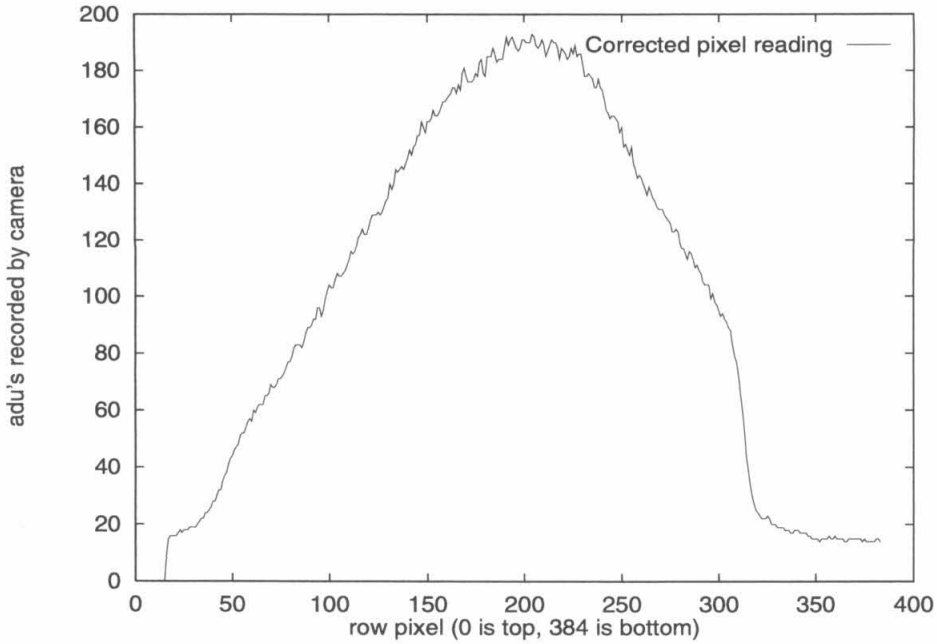

Figure B.1 Intensity profile of laser sheet for the $u_{He}/u_{air} = 1.7$, no ramp case at $x/d = 83.6$

is 106.43 adu's per pixel. That equates to 5321.4 electrons per pixel on average in the beam. The NPP term in equation (B.1) can be described as the number of electrons per pixel (or the number of *detected* photons per pixel), since the term ϵ' accounts for the collection efficiency of the array. Hence, for this example, $NPP = 5321.4$.

Since the energy output of the laser was measured before every run of the tunnel it is possible to get an estimate of the energy of the pulse. The energy per pulse varied randomly by as much as 15% from shot to shot, and the laser dye steadily lost efficiency as it aged. In spite of these errors, the resulting measurements of average radii are relatively accurate due to the weak dependence of the radius on the the energy of the pulse. For the case shown in Figure B.1 the estimated energy of the laser pulse is 2.8 J.

Substituting the wavelength of the light ($\lambda = 480\,\text{nm}$) and the index of refraction

of ice ($n = 1.33$) into equation B.2 results in

$$\sigma_m = 6.1099 \times 10^{26} r^6 \mathrm{m}^{-4} \tag{B.4}$$

All calculations are done in SI units, so the m^{-4} term is present so that σ_m comes out in m^2 when r is in meters. Substituting (B.4) into (B.1) along with values of the other variables appropriate to the experimental set up gives

$$5321\,\text{photons/pixel} = \frac{(2.8\,\mathrm{J})N}{4.138 \times 10^{-19}\,\mathrm{J/photon}} \left(6.11 \times 10^{26} \frac{r^6}{\mathrm{m}^4}\right) (0.25) \frac{\pi(1.082 \times 10^{-2}\,\mathrm{m})}{4(576 \times 384\,\text{pixels})} \frac{0.3}{(1.3)^2} \frac{1}{64} \tag{B.5}$$

Canceling units and rearranging results in

$$N r^6 = 4.831 \times 10^{-32}\,\mathrm{m}^3 \tag{B.6}$$

Finally, substituting the measured atmospheric water content for that run into (B.3) and solving for N results in

$$N = 3.664 \times 10^{-7} r^{-3} \tag{B.7}$$

Combining equations (B.6) and (B.7) to eliminate N and solving for r gives an ice crystal averages radius estimate of 5.1×10^{-9} m, or 51 Å for this case, which was in excellent agreement with the results of Thoman [27] and Stein [25]. Substituting r back in gives a number density of 2.8×10^{18} scattering clusters per cubic meter.

Similar calculations further upstream (8.2 diameters downstream of the injector exit) give an ice crystal diameter of 70 Å. This is consistent with the expected agglomeration of the crystals as they move downstream.

The scattering cross section of nitrogen is $9.0 \times 10^{-32}\,\mathrm{m}^2$ for a wavelength of 480 nm [7]. Assuming pure nitrogen in the test section with a number density of $3 \times 10^{24}\,\mathrm{m}^{-3}$, the number of photons per pixel contributed by Rayleigh scattering off of molecules of air in the test section was estimated to be 49. This is slightly less

than 1% of the signal received, indicating that scattering off of nitrogen (and hence helium, since its cross section is much smaller than that of nitrogen) was negligible.

B.3 Detailed Description of Data Reduction Process

Once an image was transferred from the Photometrics ccd camera to the computer it was corrected for nonuniformity of the laser light sheet and the variation in scattering efficiency across the test section due to the change in scattering angle. This was accomplished through a series of steps. This section will show the steps that were taken in reducing the images from a specific data set. All of the images were reduced in a similar fashion, so the one set shown here is representative of all of them.

The set of images chosen for this example was taken with $u_{He}/u_{air} = 1.32$ using the 7° ramp at a station 49.2 diameters downstream from the injector exit. The average laser pulse energy recorded before the run was 2.51 J, and the humidity level as measured by the psychrometer was 0.010 $\mathrm{kg}_{H_2O}/\mathrm{kg}_{air}$. A picture of a grid of known size was taken before each run. In addition, reference images of the laser firing without the tunnel running were taken before and after the run. It was hoped that Rayleigh scattering off of the room density air in the test section could be used to normalize the energy distribution across the beam; it would then have been possible to use the reference images to correct for scattering of the beam off of the wind tunnel windows. The Rayleigh signal from the scattering off of the air was of insufficient strength to perform the normalization, so the reference pictures were not used. Finally, dark images were taken before and after the run to get a measure of the dark noise of the ccd camera (about 50 adu's).

The 12 bit resolution of the ccd camera was greater than that of most display devices, so it was also necessary to reduce the data to an 8 bit scale for presentation. The ccd camera sent the image data to the computer encoded in a column-oriented format using 16 bit integers. The standard format for images is row-oriented, so all of the ccd images were converted to a row-oriented format for viewing.

The very first step taken in the image data reduction was to correct the images

for the off-axis viewing angle. A picture of a standard grid was taken before each run. Figure B.2 shows the grid picture taken before the run used in this example.

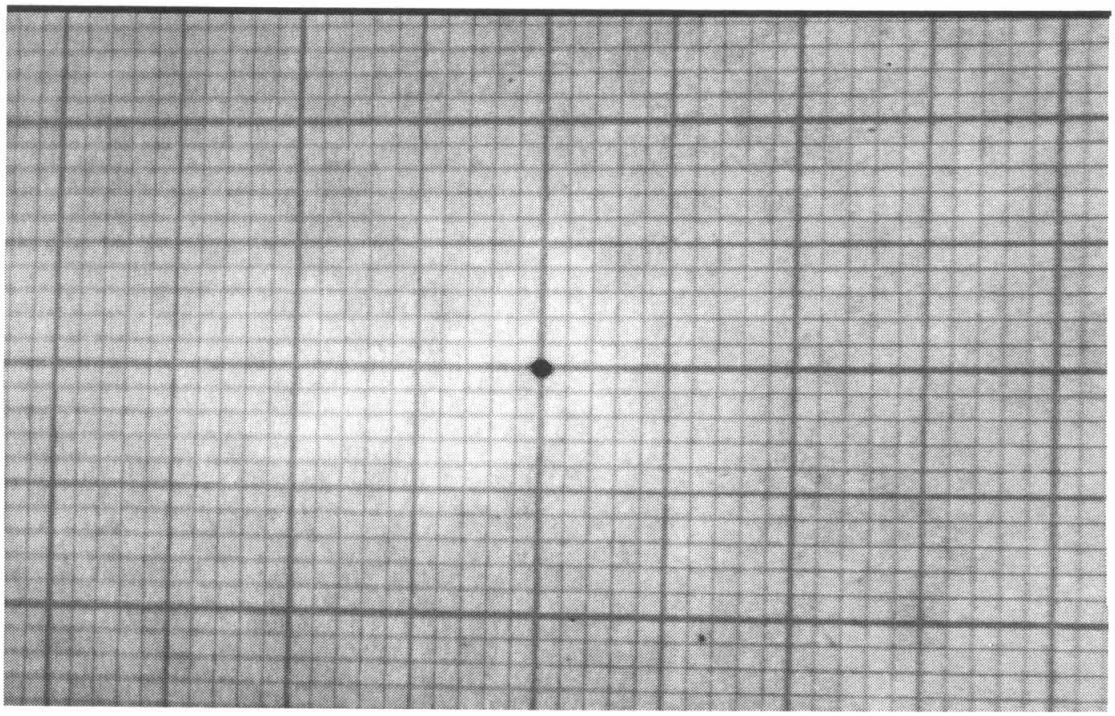

Figure B.2 Grid image for $u_{He}/u_{air} = 1.32$, 7°, $x/d = 49.2$ case

The fine grid lines were spaced 1 mm apart, and the origin used for calculating pixel units was located at the upper left-hand corner of the image. Pixel positions were numbered starting at (0,0). Grid coordinates were based upon the dark circle at the center of the grid being (0,0). The coordinates of four points were used as a basis for correcting the entire image. The same four points were used for every data set. In grid coordinates they were: (-16,11), (16,11), (16,-11), and (-16,-11). For this particular grid the corresponding pixel coordinates were: (79.0,51.0), (495.25,46.0), (490.75,349.0), and (72.25,342.0). The fractional pixel coordinates were caused by estimating the position of the center of the grid line, which was not often aligned with the pixels.

Once the pixel coordinates of the reference grid points were known it was possible to use a linear transformation to correct the entire image. The PV-WAVE Advantage^{TM} data analysis and graphing program contains an implementation of the linear correction algorithm that was used on the images. Assuming that the off axis view of the ccd camera caused a linear warping of the grid, the equations relating the distorted pixel coordinates to the undistorted pixel coordinates are [29]

$$u_i = c_0 + c_1 y_i + c_2 x_i + c_3 y_i x_i \,, \quad i = 0, 1, 2, 3 \tag{B.8}$$

$$v_i = d_0 + d_1 y_i + d_2 x_i + d_3 y_i x_i \,, \quad i = 0, 1, 2, 3 \tag{B.9}$$

In this nomenclature the uncorrected pixel coordinates are denoted by the vectors $\underline{u}$ and $\underline{v}$. The corrected pixel coordinates are denoted with the vectors $\underline{x}$ and $\underline{y}$.

Once the numbers for the reference pixels were obtained from the grid image, it was necessary to determine what the pixel coordinates of the corrected grid should be. This was done by averaging the uncorrected coordinates to get a center point and then expanding or contracting the image about that center point to give the desired magnification. The expansion or contraction needed to achieve the desired magnification was rarely over 10%. The desired final size of the box formed by the four reference points was 416 by 286 pixels, which meant that all images were scaled so that there were 13 pixels per mm in the object field ($416/32 = 286/22 = 13$). The pixel coordinates from the original grid image of Figure B.2 show a width of 416.25 pixels on the top and 418.5 pixels on the bottom. They also show a height of 291 pixels on the left and 303 pixels on the right, giving a maximum scaling of 5.9% for this data set.

Once the $\underline{u}$, $\underline{v}$, $\underline{x}$, and $\underline{y}$ vectors were chosen, the system of equations in (B.8) and (B.9) could be solved for $\underline{c}$ and $\underline{d}$. The pictures were then all processed through an image warping procedure in PV-WAVE. The warping procedure went through the final image one pixel at a time substituting the $\underline{x}$ and $\underline{y}$ values for each pixel into equations (B.8) and (B.9); this gave the corresponding pixel coordinate in the original distorted image. A bilinear interpolation was then used to determine the

pixel value to use in the corrected image.

Figure B.3 is the corrected version of Figure B.2. The black region at the top of

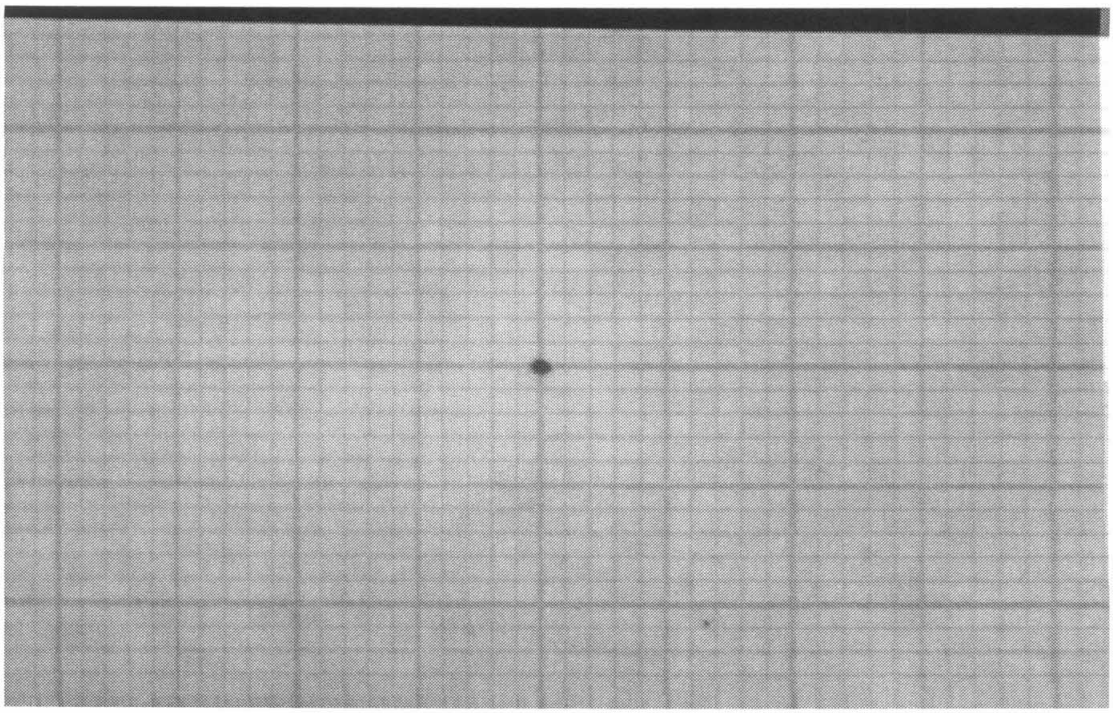

Figure B.3 Corrected grid image for $u_{He}/u_{air} = 1.32$, 7°, $x/d = 49.2$ case

the image and the bright region on the right are the result of the warping process. They represent pixels which mapped to a region outside of the original grid image, and are spurious.

Figure B.4 shows an original uncorrected image from the data set. The image was changed from column-oriented to row-oriented, had the dark image subtracted from it, and the 12 bit depth of the ccd data was scaled to 8 bits for printing. This data image and all others from this data set were warped to correct for the off axis view and then combined into an average picture shown in Figure B.5. The brighter vertical bands toward the right of both images are caused by reflection off of both surfaces of the tunnel test section window that the ccd camera was looking through.

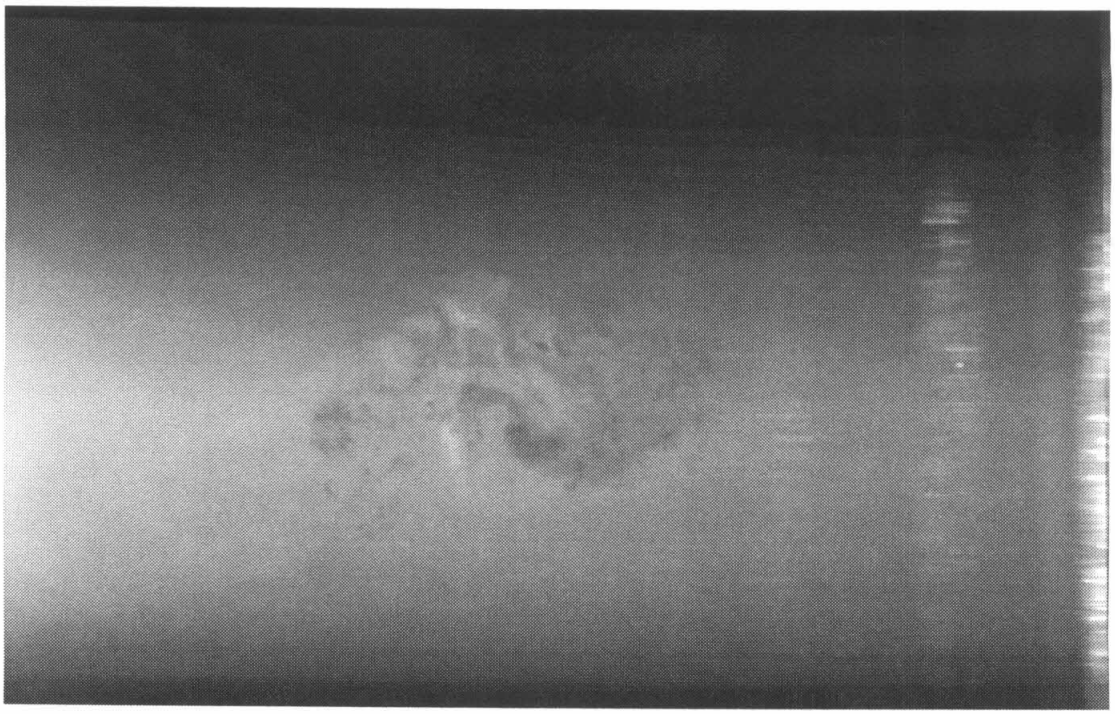

Figure B.4 First image from $u_{He}/u_{air} = 1.32$, 7°, $x/d = 49.2$ case

Every effort was made to keep this window as clean as possible, but some reflections were unavoidable. The tunnel windows gradually built up what appeared to be an oily residue on their surfaces as the tunnel ran. This was in spite of the 0.2 μm air filter upstream of the tunnel inlet.

After an average image was produced a window was chosen. The window enclosed the region of interest, and the method of data reduction required that the edges of the window all lie inside the laser beam. The white box in Figure B.5 shows the box chosen in this case.

After each individual picture was corrected for the dark noise, changed to row-oriented, and warped to correct for the off axis viewing angle it was cropped using the chosen window. Due to the large variation in laser intensity across the beam it was necessary to normalize across the image to get a uniform background field.

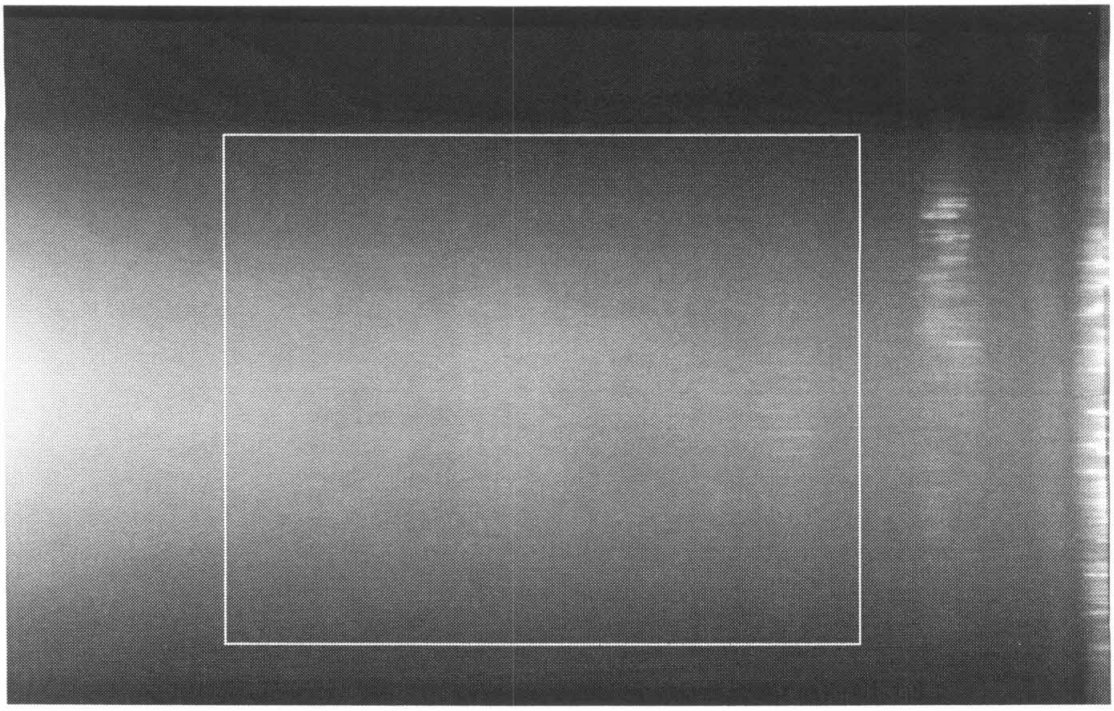

Figure B.5 Distortion corrected average of all frames from $u_{He}/u_{air} = 1.32$, 7°, $x/d = 49.2$ case

Variation of the scattering intensity across the width of the tunnel was also large enough that a normalization process was needed. Figure B.6 shows the left and right edges of the cropped image from the first frame of the example data set. Figure B.7 shows the top and bottom edges from the same cropped frame. These show the variability of the distribution of energy across the laser pulse from shot to shot. The top and bottom rows of the cropped average frame were at approximately the same intensity, but the top and bottom rows of the first frame clearly show more energy toward the bottom of the beam. The greater intensity on the left of the window was caused by the increase in the scattering cross section for the portion of the laser light polarized parallel to the viewing plane.

In addition to the horizontal variation in intensity due to the change in scattering cross section there was also the effect of diffuse scattering off of the windows and

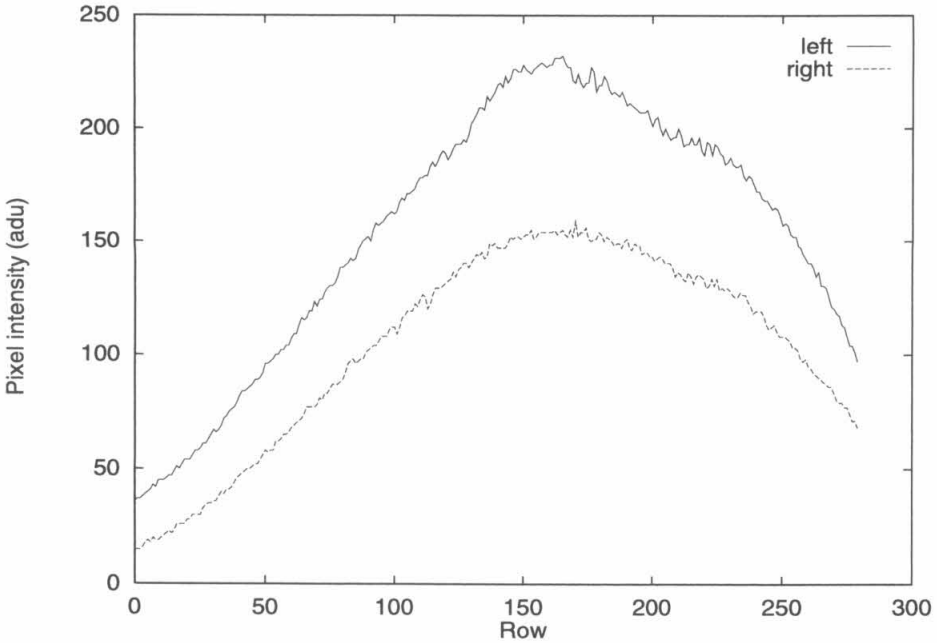

Figure B.6 Left and right columns from first image of $u_{He}/u_{air} = 1.32$, 7°, $x/d = 49.2$ case

various parts of the tunnel test section. Luckily, this seemed to vary little with the distribution of intensity across the laser sheet. Thus, it was possible to average several reference frames and subtract the result from the cropped images. The accuracy of this was limited by the 10-15% variation in the laser energy output, but since the diffuse scattering was a small portion of the total light received by the ccd camera this method was considered adequate.

The four edges of each cropped image were then used to construct a background field by interpolation from edge to edge. This field represented the image which would have been collected had there been no jet. This field was then divided into a field with a uniform intensity of 224 adu's to form a correction field. When the correction field was multiplied pixel by pixel with the original image the result was an image with a uniform background intensity. The intensity plot of the bottom row in Figure B.7 shows a slight bump near the 300^{th} column. This was likely due

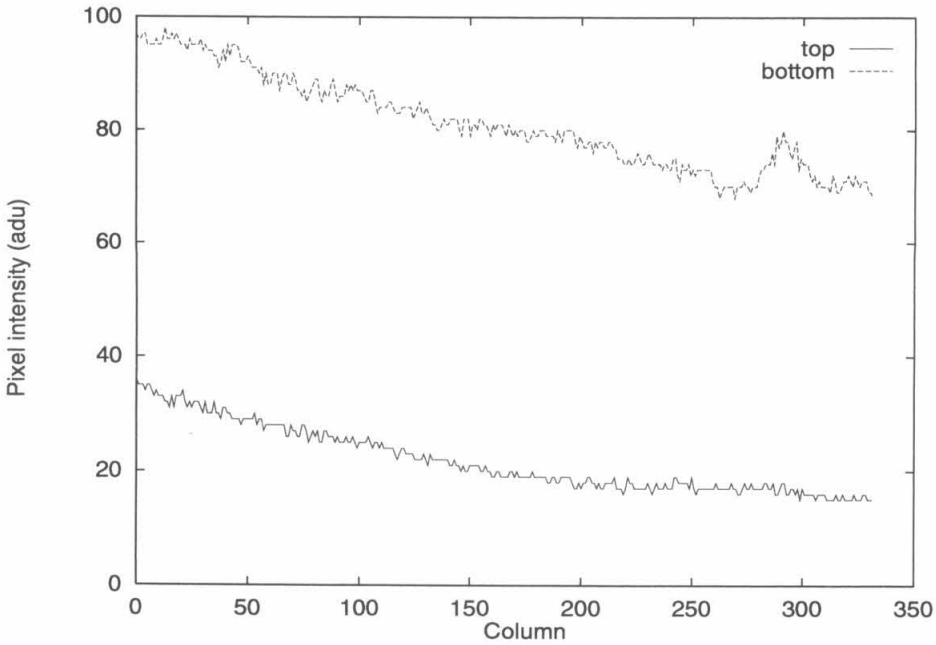

Figure B.7 Top and bottom rows from first image of $u_{He}/u_{air} = 1.32$, 7°, $x/d = 49.2$ case

to some bit of dust present in the flow at that point. Bumps like this were deleted from the edge curves and the missing points replaced by an interpolation based on the remaining points.

Appendix C

Pressure and Temperature Measurements of the Jet

The time averaged values of the position, total area, and shape of the jet were determined from the pressure and temperature data taken at various downstream stations in the tunnel. The pressure and temperature data consisted of measurements made along vertical lines. Rotation of the probe along the axis of the traverse allowed for off axis measurements. Constraints on the amount of tunnel time available, along with a diminishing of the incremental information gained as the number of traverses increased, constrained the number of traverses per streamwise probing location. This led to a higher concentration of data points along the vertical direction of the jet cross section and a lower concentration in the horizontal direction.

The cross sectional views of the jet were made by first non-dimensionalizing the positional information in each data file (there was one data file per traverse). A computer program written by the author then read in each data file, along with information on how it was taken (*e.g.*, the angle of the probe off of the tunnel centerline), and output a file containing the probe data and the y and z coordinates for each reading. Another program then read this file and performed a linear interpolation between each data point along each traverse. The points between each traverse were then interpolated. Thus, the denser vertical traverses were interpolated first, and the sparser spaces in between them interpolated last. The resolution for the final result was chosen to be 0.01 exit diameters per pixel. This was chosen primarily

for the convenience of scaling, as it is ten times more dense than the data points on the vertical traverse.

Once these data files had been obtained, area measurements of the jet were easily obtained by counting the number of pixels whose value was under the threshold chosen. The 80% contours were normally used as the basis for defining the edge of the jet in these experiments, as they consistently described closed, regularly shaped regions. The jet area measurement for a specific data type (*e.g.*, pressure) was made by counting the number of pixels whose value was less than or equal to 80% of the maximum pixel value in the entire image.

The radius of gyration was calculated for each cross section to give additional information on the shape and growth of the jet. Unlike the area calculation described above, the radius of gyration depends on the distribution of fluid within the jet. The first step in calculating the radius of gyration was to calculate the center of mass of the jet, since all radius of gyration calculations here are about the center of mass of the jet. The center of mass was calculated by finding the total mass of the jet, M, and its moments about the axes of interest, M_y and M_z.

$$M = \iint_A \rho(y,z)\, dA \tag{C.1}$$

$$M_y = \iint_A z\rho(y,z)\, dA \tag{C.2}$$

$$M_z = \iint_A y\rho(y,z)\, dA \tag{C.3}$$

The center of mass coordinates could then be found

$$\overline{y} = \frac{M_z}{M} \qquad \overline{z} = \frac{M_y}{M} \tag{C.4}$$

The term $\rho(y,z)$ in these equations refers to the local density of the field being integrated over (*e.g.*, the pixel values when an area integral is converted into a summation over a region of an image). Once the center of mass was found the second

moments, M_{yy} and M_{zz}, and the radius of gyration, r, could then be calculated.

$$M_{yy} = \iint_A (z - \overline{z})^2 \rho(y, z)\, dA \tag{C.5}$$

$$M_{zz} = \iint_A (y - \overline{y})^2 \rho(y, z)\, dA \tag{C.6}$$

$$r = \sqrt{\frac{M_{yy} + M_{zz}}{M}} \tag{C.7}$$

Appendix D

Thermocouple Time Response

If radiative terms are negligible, the temperature relationship between a thermocouple and the surrounding fluid is given by the first-order differential equation [21]

$$T_{gas} = \left(1 + \tau \frac{d}{dt}\right) T_{junction} \tag{D.1}$$

This implies that a square wave pulse in the gas temperature will result in an exponential response by the thermocouple. The time constant, τ, is defined by

$$\tau = \frac{\rho c d}{4h} \tag{D.2}$$

where ρ is the wire's density, c_p is its specific heat, d is its diameter, and h is the appropriate convective heat transfer coefficient.

The Nusselt number, Nu, is related to the heat transfer coefficient and the thermal conductivity of the gas by [17]

$$Nu = \frac{hd}{k} \tag{D.3}$$

Using appropriate physical constants for the thermocouple wire (from Caldwell [4]) and Nusselt number estimates from Laufer and McClellan [17] an estimate for the time constant of the thermocouple's response in air was found to be 17 ms.

The time constant was also measured using an electronic circuit similar to that used by Kendrick [15] which put a square wave voltage on the junction. The circuit

included diodes which isolated the junction so that its response could be measured after the falling edge of the square wave. The data from these measurements was fit to an exponential, and the time constants for the air freestream and helium jet (at the injector exit for the $u_{He}/u_{air} = 1.7$ case) were found to be 22.5 ms and 17.5 ms, respectively.

Conduction along the thermocouple wire can be important if the ratio of thermocouple length to cold length is less than 10 [21]. The cold length is defined as $\sqrt{\alpha\tau}$, where α is the thermal diffusivity of the wire material. The results of these time constant measurements suggested a cold length of 0.34 mm, and the wire length was approximately 6 mm. This indicated that conduction to the probe supports should have been negligible. The study of conduction along the thermocouple wire discussed in Section 3.2 was undertaken because the desired resolution of the temperature measurements was less than the length of the thermocouple wire.

Appendix E

Additional Rayleigh Scattered Images

This appendix contains a collection of images which provide a sample of the different jet cross sections seen at the various test conditions.

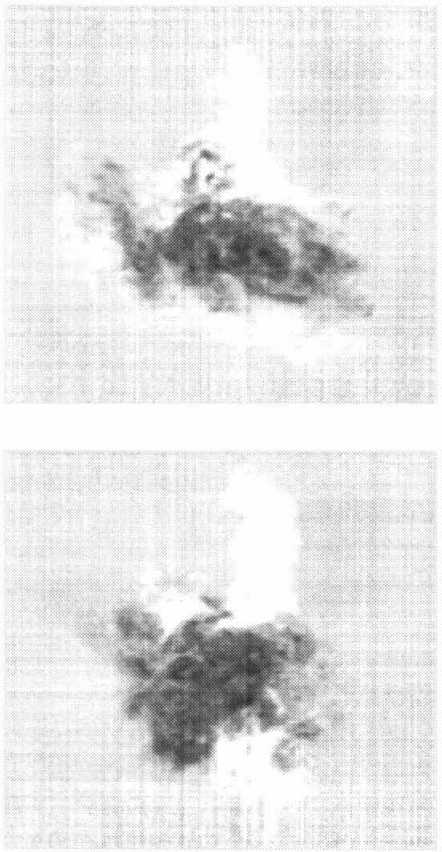

Figure E.1 Two Rayleigh scattered images for the $u_{He}/u_{air} = 1.7$, no ramp case at x/d=16.4.

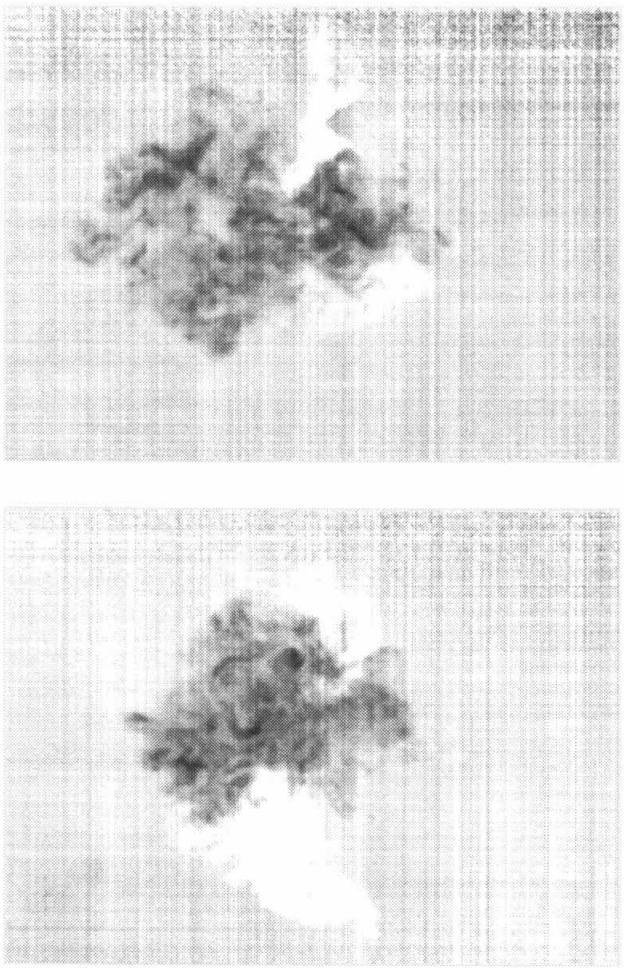

Figure E.2 Two Rayleigh scattered images for the $u_{He}/u_{air} = 1.7$, no ramp case at x/d=32.8.

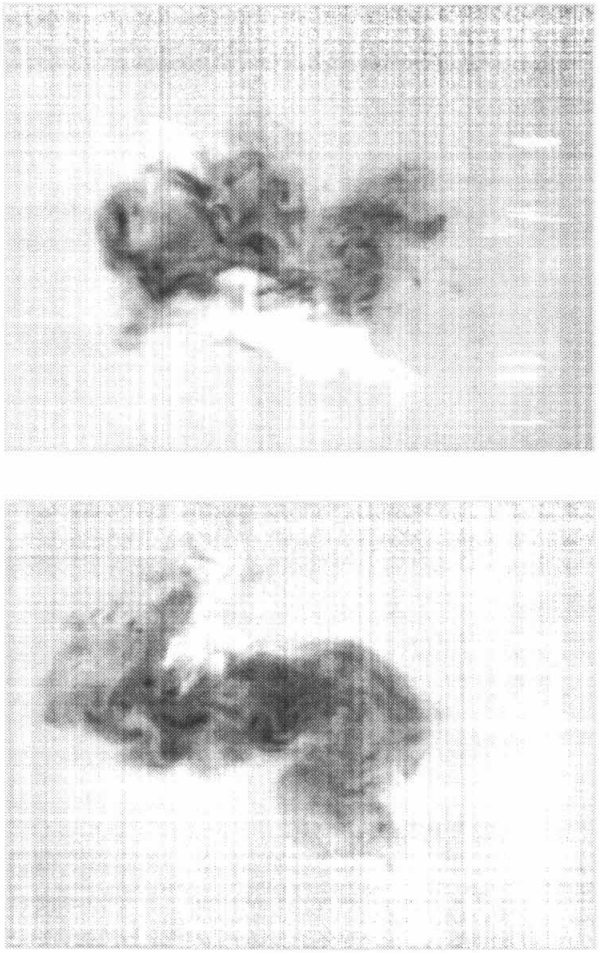

Figure E.3 Two Rayleigh scattered images for the $u_{He}/u_{air} = 1.7$, no ramp case at x/d=49.2.

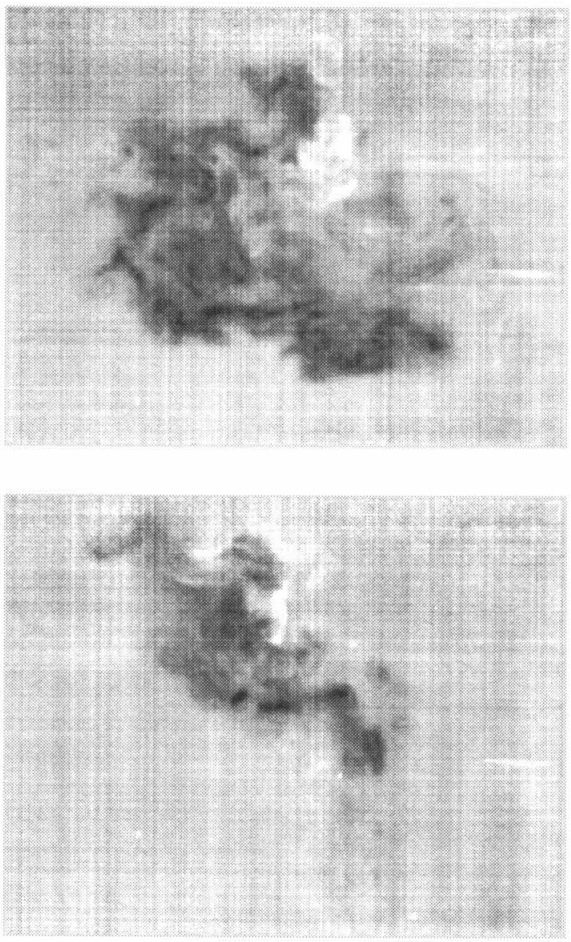

Figure E.4 Two Rayleigh scattered images for the $u_{He}/u_{air} = 1.7$, no ramp case at x/d=66.4.

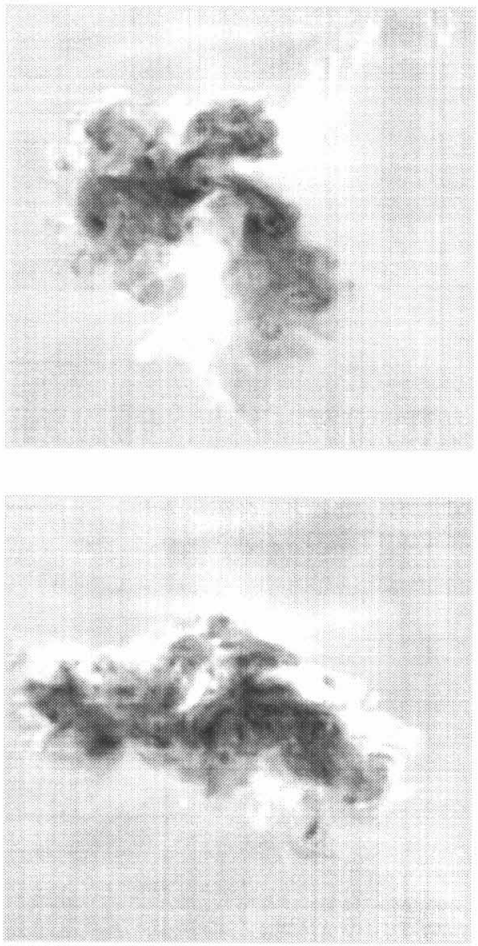

Figure E.5 Two Rayleigh scattered images for the $u_{He}/u_{air} = 1.7$, 4.5° ramp case at x/d=32.8.

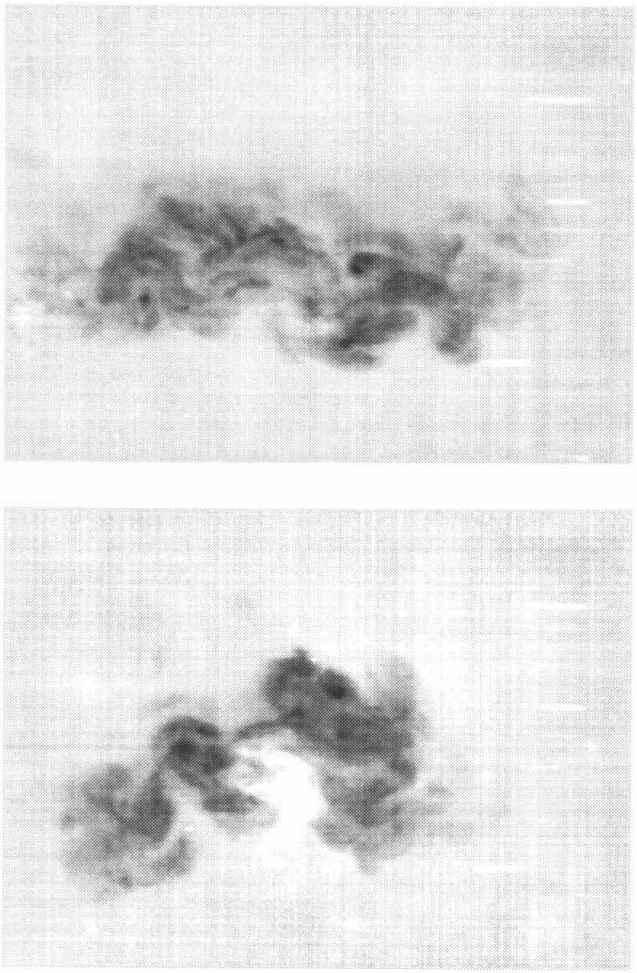

Figure E.6 Two Rayleigh scattered images for the $u_{He}/u_{air} = 1.7$, 4.5° ramp case at x/d=49.2.

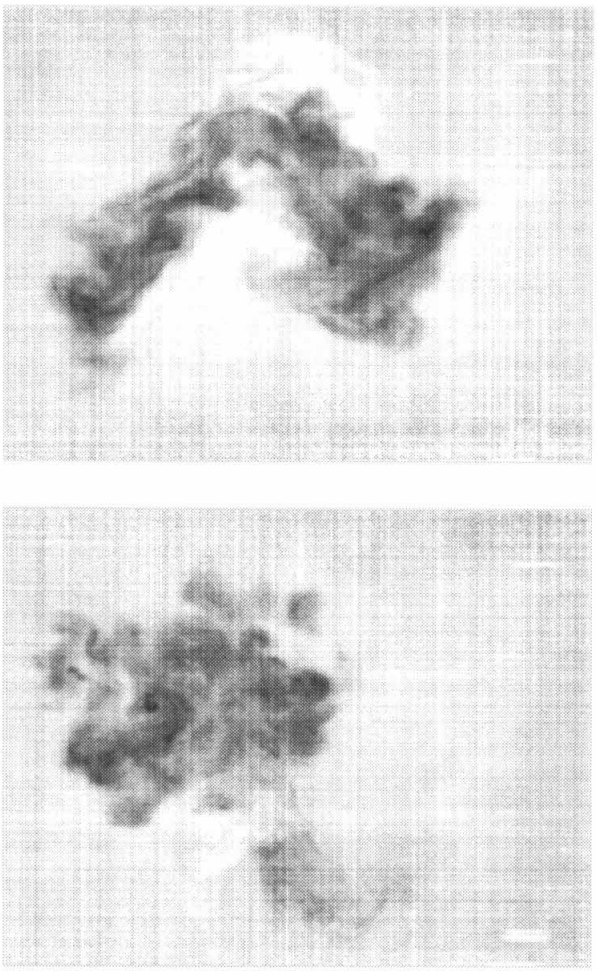

Figure E.7 Two Rayleigh scattered images for the $u_{He}/u_{air} = 1.7$, 4.5° ramp case at x/d=66.4.

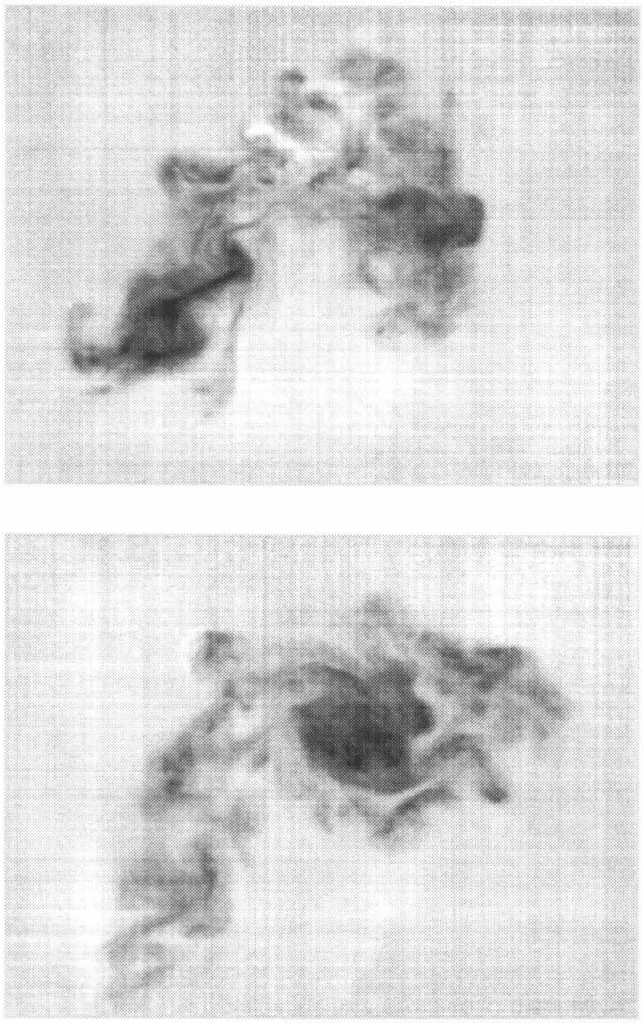

Figure E.8 Two Rayleigh scattered images for the $u_{He}/u_{air} = 1.7$, 4.5° ramp case at x/d=83.6.

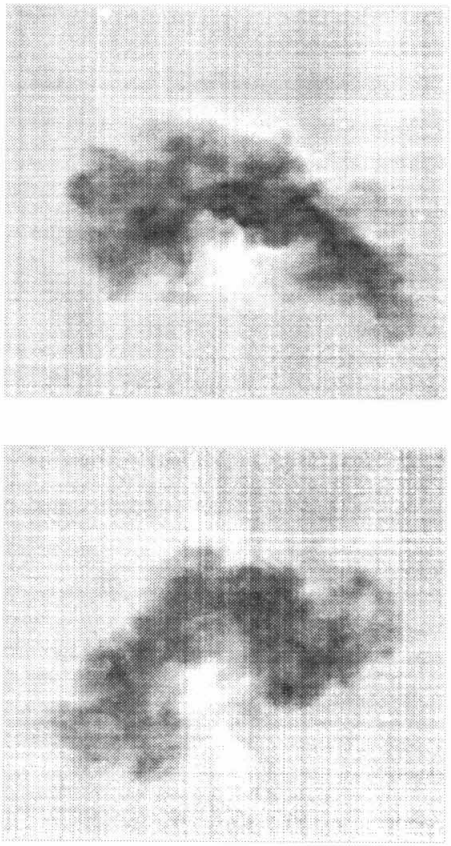

Figure E.9 Two Rayleigh scattered images for the $u_{He}/u_{air} = 1.7$, 7.0° ramp case at x/d=32.8.

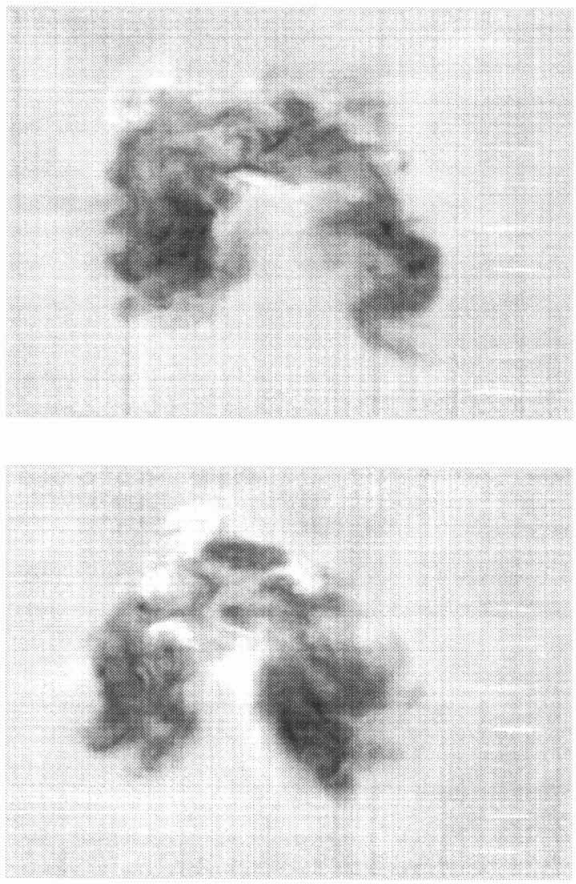

Figure E.10 Two Rayleigh scattered images for the $u_{He}/u_{air} = 1.7$, 7.0° ramp case at x/d=49.2.

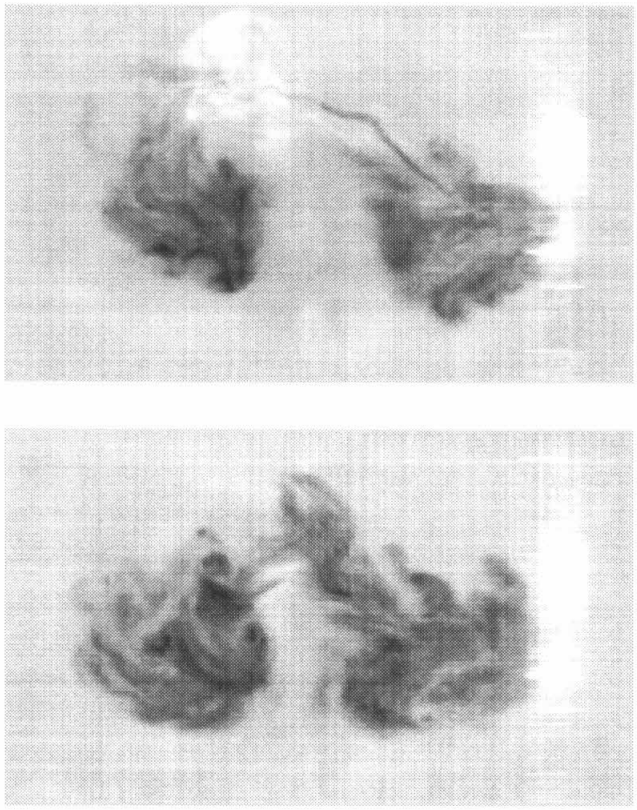

Figure E.11 Two Rayleigh scattered images for the $u_{He}/u_{air} = 1.7$, 7.0° ramp case at x/d=66.4.

Bibliography

[1] H. Wilhelm Behrens. Total temperature thermocouple probe based on recovery temperature of circular cylinder. *International Journal of Heat and Mass Transfer*, 14:1621–1630, 1971.

[2] Martin Brouillette. *On the Interaction of Shock Waves with Contact Surfaces Between Gases of Different Densities.* Ph.D. thesis, California Institute of Technology, 1989.

[3] John M. Budzinski. *Planar Rayleigh Scattering Measurements of Shock Enhanced Mixing.* Ph.D. thesis, California Institute of Technology, 1992.

[4] F. R. Caldwell. *Thermocouple Materials.* U.S. Government Printing Office, 1962. Monograph 40.

[5] Donald E. Coles. Private communication, 1992.

[6] J. Philip Drummond. Mixing enhancement of reacting parallel fuel jets in a supersonic combustor. In *AIAA/SAE/ASME/ASEE 27th Joint Propulsion Conference*, number 91–1914, Washington, D.C., 1991. American Institute of Aeronautics and Astronautics.

[7] Alan C. Eckbreth. *Laser Diagnostics for Combustion Temperature and Species*, volume 7 of *Energy and Engineering Science Series.* Abacus Press, Cambridge, Mass., 1988.

[8] Jean-Francois Luc Haas. *Interaction of Weak Shock Waves and Discrete Gas Inhomogeneities.* Ph.D. thesis, California Institute of Technology, 1984.

[9] Jean-Francois Luc Haas and Bradford Sturtevant. Interaction of weak shock waves with cylindrical and spherical gas inhomogeneities. *Journal of Fluid Mechanics*, 181:41–76, Aug 1987.

[10] Jeff Hecht. *The Laser Guidebook.* McGraw-Hill Book Company, New York, 1986.

[11] William H. Heiser and David T. Pratt. *Hypersonic Airbreathing Propulsion.* American Institute of Aeronautics and Astronautics, Inc., Washington, D.C., 1994.

[12] F. J. Higuera and A. Li nán. Choking conditions for nonuniform viscous flows. *Physics of Fluids A*, 5(3):768–770, Mar 1993.

[13] Jeffry W. Jacobs. Shock-induced mixing of a light-gas cylinder. *Journal of Fluid Mechanics*, 234:629–649, Jan 1992.

[14] Khalid A. Juhany. *Supersonic Film Cooling Including the Effect of Shock Wave Interaction.* Ph.D. thesis, California Institute of Technology, 1994.

[15] Donald William Kendrick. *An Experimental and Numerical Investigation into Reacting Vortex Structures Associated with Unstable Combustion.* Ph.D. thesis, California Institute of Technology, 1995.

[16] Toshi Kubota. Private communication, 1996.

[17] John Laufer and Robert McClellan. Measurements of heat transfer from fine wires in supersonic flows. *Journal of Fluid Mechanics*, 1(3):276–289, 1956.

[18] Frank E. Marble, Gavin J. Hendricks, and Edward E. Zukoski. Progress toward shock enhancement of supersonic combustion processes. In *AIAA/SAE/ASME/ASEE 23rd Joint Propulsion Conference*, number 87–1880, Washington, D.C., 1987. American Institute of Aeronautics and Astronautics.

[19] Earl J. McCartney. *Optics of the Atmosphere: Scattering by Molecules and Particles.* Wiley Series in Pure and Applied Optics. John Wiley & Sons, New York, 1976.

[20] A. Melling. Seeding gas flows for laser anemometry. In *Advanced Engineering for Aero Engine Components*, number CP–399, pages 8.1–8.11. AGARD, 1986. Presented at the Propulsion and Energetics Panel 67^{th} Symposium.

[21] P. C. Miles and F. C. Gouldin. Determination of the time constant of fine-wire thermocouples for compensated temperature measurements in premixed turbulent flames. *Combustion Science and Technology*, 89:181–199, 1993.

[22] J. M. Picone and J. P. Boris. Vorticity generation by shock propagation through bubbles in a gas. *Journal of Fluid Mechanics*, 189:23–51, Apr 1988.

[23] George Rudinger and Lowell M. Somers. Behavior of small regions of different gases carried in accelerated gas flows. *Journal of Fluid Mechanics*, 7:161–176, Feb 1960.

[24] Dale E. Seborg, Thomas F. Edgar, and Duncan A Mellichamp. *Process Dynamics and Control.* John Wiley & Sons, New York, 1989.

[25] Gilbert D. Stein. Angular and wavelength dependence of the light scattered from a cloud of particles formed by homogeneous nucleation. *The Journal of Chemical Physics*, 51(3):938–942, Aug 1969.

[26] H. Guyford Stever. Condensation phenomena in high speed flows. In H. W. Emmons, editor, *Fundamentals of Gas Dynamics*, volume 3 of *High Speed Aerodynamics and Jet Propulsion.* Princeton University Press, 1958.

[27] H. Thoman. Size of ice crystals formed during rapid expansion of humid air. *The Physics of Fluids*, 9(5):896–902, May 1966.

[28] H. C. van de Hulst. *Light Scattering by Small Particles.* Dover Publications, Inc., New York, 1981.

[29] Visual Numerics. *PV-WAVE Advantage^{TM} PV-WAVE Command Language^{TM} User's Guide.* Version 4.2.

[30] Ian A. Waitz. *An Investigation of Contoured Wall Injectors for Hypervelocity Mixing Augmentation.* Ph.D. thesis, California Institute of Technology, 1991.

[31] Ian A. Waitz, Frank E. Marble, and Edward E. Zukoski. Investigation of a contoured wall injector for hypervelocity mixing augmentation. *AIAA Journal*, 31(6):1014–1021, Jun 1993.

[32] Joseph Yang. *An Analytical and Computational Investigation of Shock-Vortical Flows with Applications to Supersonic Combustion.* Ph.D. thesis, California Institute of Technology, 1991.

[33] Joseph Yang, Toshi Kubota, and Edqard E. Zukoski. Applications of shock-induced mixing to supersonic combustion. *AIAA Journal*, 31(5):854–862, May 1993.

[34] Joseph Yang, Toshi Kubota, and Edward E. Zukoski. A model for characterization of a vortex pair formed by shock passage over a light-gas inhomogeneity. *Journal of Fluid Mechanics*, 258:217–244, Jan 1994.